Magmatic evolution of the Campi Flegrei and Procida volcanic fields, Italy, based on interpretation of data from well-constrained melt inclusions

Rosario Esposito[a,*], Kimberly Badescu[a], Matthew Steele-MacInnis[b], Claudia Cannatelli[c], Benedetto De Vivo[d,e], Annamaria Lima[f], Robert J. Bodnar[g], Craig E. Manning[a]

[a] Department of Earth, Planetary and Space Science, UCLA, Los Angeles, CA 90095-1567, USA
[b] Department of Earth and Atmospheric Sciences, University of Alberta, Edmonton, Alberta T6G 2E3, Canada
[c] Department of Geology and Andean Geothermal Center of Excellence (CEGA), Universidad de Chile, Santiago, Chile
[d] Pegaso University, Piazza Trieste e Trento 48, Napoli, Italy
[e] Benecon Scarl, Via S. Maria di Costantinopoli 104, Napoli, Italy
[f] Dipartimento di Scienze della Terra, delle Risorse e dell'Ambiente, Università di Napoli Federico II, Via Cintia snc, 80126 Napoli, Italy
[g] Fluids Research Laboratory, Department of Geosciences, Virginia Tech, Blacksburg, VA 24061, USA

ABSTRACT

One of the main goals of studying melt inclusions (MI) is to constrain the pre-eruptive physical and chemical processes that have occurred in a magma reservoir at the micro-scale. Recently, several studies that focused on magmatic differentiation of volcanic systems produced detailed interpretations based on data from MI trapped at different times and locations in the plumbing system. Ideally, MI data should be collected and tested following the melt inclusion assemblage (MIA) protocol that consists of studying and analyzing groups of MI that were trapped at the same time, and, thus, at the same chemical and physical conditions. However, the rarity of MIA in juvenile volcanic phenocrysts precludes this methodology in many cases, leading to uncertainty concerning the validity of the MI as recorders of pre-eruptive conditions.

In this study, we focused on MI from the Campi Flegrei (CF) and the Island of Procida (IP) volcanic systems in southern Italy, including data from this study and data from the literature. The database included MI hosted in sanidine, clinopyroxene, plagioclase, biotite and olivine, and, thus, represents melts trapped at various stages in the overall differentiation process. We developed a protocol to select the most reliable MI from a dataset associated with a single magmatic system. As a first step we compare MI data with bulk rock data for the same magmatic system. This comparison reveals that most MI show major element compositions that fall within or close to the range for bulk rocks – these MI are considered to be "normal". Some MI show anomalous compositions and are not representative of the melt in equilibrium with the phenocryst host and were excluded from the data set. In the second step we selected only bubble-free MI from the previously identified "normal" MI to interpret the volatile evolution. In the third step we compare compositions of the "normal" bubble-free MI to compositions predicted by rhyolite-MELTS simulations, assuming a variety of initial conditions.

Comparison of data obtained from basaltic-trachybasaltic MI with rhyolite-MELTS predictions indicates that one group of MI records the geochemical evolution of a volatile-saturated magma differentiating by polybaric fractional crystallization from ≥ 200 MPa (≥ 7.5 km) to 30 MPa (~1 km). Another group of MI records recharge of the magma chamber by a primitive basaltic magma that mixes with the preexisting primitive trachybasaltic magma before eruption. Extensive isobaric crystallization of the trachybasaltic magmas at ~7.5 km beneath CF may have generated trachytic-phonolitic magmas, such as those associated with the Neapolitan Yellow Tuff (NYT) that is characterized by a relatively high H_2O content. These volatile-saturated trachytic-phonolitic magmas likely trigger high-magnitude eruptions during their ascent to the surface.

1. Introduction

Campi Flegrei (CF) and the Island of Procida (IP) are well known recently active volcanic complexes in the Campanian Plain of southern Italy that represent a volcanic hazard owing to their proximity to Naples and the towns surrounding Pozzuoli Bay (~1.5 million
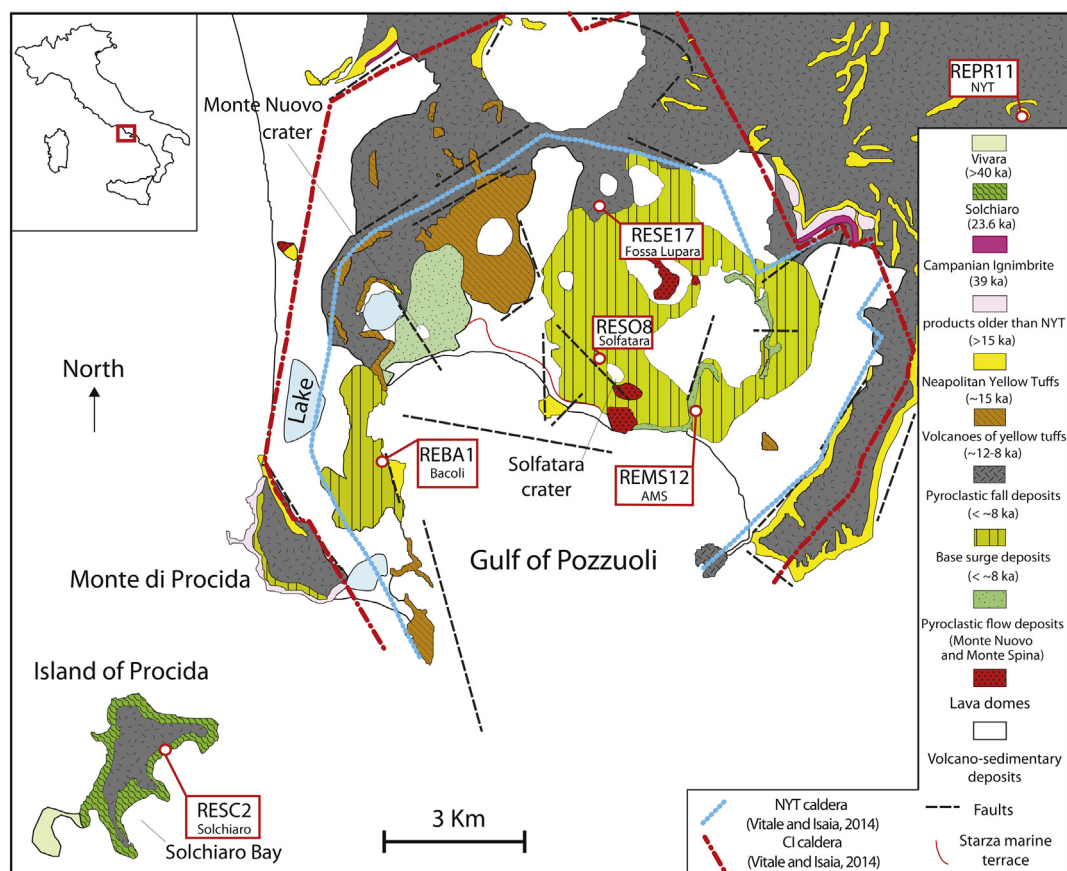
Fig. 1. Simplified geological map of Campi Flegrei and Procida, modified after Di Vito et al. (1985) by Scandone (1997). Locations of the caldera rims are based on Vitale and Isaia (2014), though we attribute the source of the CI to outside CF (De Vivo et al., 2001; Rolandi et al., 2003; De Natale et al., 2016). White circles with red outlines are locations of samples analyzed in this study (sample names indicated). NYT = Neapolitan Yellow Tuff; AMS = Agnano-Monte Spina; CI = Campanian Ignimbrite. (For interpretation of the references to colour in this figure legend, the reader is referred to the web version of this article.)

inhabitants). The area has been the site of volcanic activity for > 60 ka (De Vivo et al., 2010; Orsi et al., 1999; Pappalardo et al., 1999). The most catastrophic eruption at CF is the Campanian Ignimbrite (e.g., Orsi et al., 1996), generating 300 km^3 dense rock equivalent [DRE; (Fedele et al., 2007)], the source of which remains under debate (De Vivo et al., 2010; De Vivo et al., 2001; Rolandi et al., 2003). The later eruption of the Neapolitan Yellow Tuff (NYT) was extremely explosive and generated 40 km^3 DRE of eruptive products (Orsi et al., 1992; Wohletz et al., 1995). The most recent eruption occurred in 1538 and formed the Monte Nuovo cinder cone volcano (Fig. 1).

The CF area has in recent decades attracted the interest of geoscientists owing to activity that consists of episodic slow ground uplift, followed by more rapid deflation (bradyseism). In recent years, the ground in the central part of the CF has been inflating, highlighting the critical need for understanding whether this activity is a precursor of an imminent eruption (e.g., Chiodini et al., 2015). Ground deformation and seismicity at CF are also associated with intense fumarolic and hydrothermal activity, concentrated mostly in the crater of Solfatara at Pozzuoli (Fig. 1). The relatively slow ground uplift may or may not represent a precursor of a volcanic eruption, depending on the cause of the inflation (Bodnar et al., 2007; Lima et al., 2009; Moretti et al., 2017). Though various models have been proposed to explain bradyseism at CF, it is now becoming clear that magmatic fluids released from deep and/or shallow magmas play an important role in ground movement, and the occurrence of ground movement does not require that a new batch of magma is intruding below CF (e.g., Lima et al., 2009; Lima et al., 2017).

The composition of exsolved magmatic fluids injected into the overlying hydrothermal system is controlled by the chemical evolution

of volatiles during magma evolution (crystallization, mixing, and crustal assimilation). The compositions of MI hosted in olivine from CF and IP suggest that trachybasaltic parental magmas are the source of activity in both areas (Cannatelli et al., 2007; Mangiacapra et al., 2008; Mormone et al., 2011; Esposito et al., 2011). However, the isotopic compositions of mafic bulk rocks suggest that the two areas experienced different magma evolution histories (e.g., Cannatelli, 2012; D'Antonio et al., 2007; Peccerillo, 2017 and references therein). While major and trace element trends in both localities are dominantly controlled by fractional crystallization, the variability of some elements such as potassium, the isotopic signature of the bulk rocks, and the composition and zoning of juvenile mineral phases combined suggest that other open-system magmatic processes also contributed to observed geochemical trends. The geochemical variability, evolution, and the importance of open-system processes associated with the generation and the differentiation of these magmas continue to be debated (Peccerillo, 2017 and references therein).

The pre-eruptive volatile contents of magmas associated with CF and IP have been studied by many workers by analyzing the glass of melt inclusions (MI) (Arienzo et al., 2016; Arienzo et al., 2010; Cannatelli et al., 2007; Cecchetti et al., 2001; Cecchetti et al., 2003; Cipriani et al., 2008; Esposito et al., 2011; Fourmentraux et al., 2012; Mangiacapra et al., 2008; Mormone et al., 2011; Roach, 2005; Stock et al., 2016). MI provide information that is not easily obtained by studying bulk rocks or active fumaroles. MI often preserve pre-eruptive volatile contents because host phenocrysts act as an insulating capsule and MI are not affected by degassing of the surrounding magma that likely occurs during ascent and crystallization (Metrich and Wallace, 2008). However, interpretation of volatile data from MI, and thus the

modeling of magma dynamics, is based on the assumption that MI record the composition of the melt from which the host minerals formed. However, MI may not preserve the original melt composition if (1) the composition of the glass phase does not represent the composition of the melt that was originally trapped owing to a variety of processes [e.g., post entrapment crystallization, diffusion of elements, formation of a vapor bubble, decrepitation (Cannatelli et al., 2016 and references therein)], (2) if boundary layer processes during trapping modified the composition of the melt adjacent to the growing crystal, such that the trapped melt does not represent the bulk (far-field) melt (e.g., Baker, 2008), or (3) the melt that was trapped was generated as a result of disequilibrium processes (e.g., Danyushevsky et al., 2004). It is important to note that while concentrations and ratios of elements that are compatible in the host will be modified by post entrapment crystallization (PEC), PEC does not affect ratios of incompatible elements in the melt (now glass) (Danyushevsky et al., 2002a; Lima et al., 2003).

The most rigorous and dependable approach to confirm that the composition of a MI is representative of the melt from which the host crystal grew is to study groups of MI that were trapped at the same time, defined as a "melt inclusion assemblages" (MIA; Bodnar and Student, 2006). All MI within an MIA would have been trapped at the same temperature and pressure, and all would have trapped a melt of the same composition. As such all of the MI within the MIA should show consistent phase behavior and chemistry (Bodnar and Student, 2006). While studying MIAs can provide unarguable evidence that the MI have trapped and preserved the original melt from which the host crystal was growing, melt inclusion assemblages are uncommon in most samples, and workers have rarely reported melt inclusion assemblages in studies of MI from CF and IP owing to their scarcity (Esposito et al., 2014). Also, the few MIA identified by Esposito et al. (2014) are comprised of small MI (< 20 μm), and therefore challenging or impossible to analyze by secondary ion mass spectrometry (SIMS) and/or Fourier-transform infrared (FTIR) spectroscopy.

As an alternative to the MIA approach to test that compositions of MI represent the original melt that was present when the phenocryst was growing, the composition of MI may be compared to the bulk rock compositions of samples from the same magmatic system (Danyushevsky et al., 2000). This comparison can help identify MI compositions that are anomalous relative to general geochemical trends defined by bulk rocks. While both the MIA approach and comparison of MI compositions with bulk rock compositions can be applied to determine if the volatile contents of MI represent the volatile content of the original, pre-eruptive melt, we note that most previous studies of MI from CF and IP have not reported or discussed methods to test whether the major elements and volatile contents of MI record the original, unmodified composition. Here, we use the term "representativeness" to identify a MI that traps and preserves a sample of the melt that was in equilibrium with the host phenocryst at the time of trapping. In other words, MI represent a "snapshot" of the liquid (melt) composition during magmatic differentiation, representing melt that was in equilibrium with crystals ± vapor. One of the main factors that limits our ability to determine whether volatile contents of MI from CF and IP reported in the literature represent the original volatile content of the trapped melt is that contributions of the vapor bubble in the MI to the total volatile content of the MI are not discussed or considered, even though vapor bubbles are reported in the descriptions of MI petrography. Recent studies confirm that analyzing only the glass phase of a bubble-bearing MI and ignoring the CO_2 content of the bubble significantly underestimates the total CO_2 (and other volatile) content of the trapped melt (e.g., Aster et al., 2016; Esposito et al., 2016; Moore et al., 2015). Because most of the CO_2 is contained in the vapor bubble of a bubble-bearing MI, a more realistic and accurate estimate of the CO_2 content of the trapped melt is obtained if only the bubble, rather than only the glass, is analyzed. Concentrations of other volatiles, including H_2O and S, will similarly be underestimated if the volatile content of the bubbles is not considered (Esposito et al., 2016).

Given these concerns, it is appropriate to re-evaluate MI data from CF and IP because published reports often do not specify whether or not the MI that were studied contain vapor bubbles. In addition, MI compositions are often not compared with bulk rock compositions and geochemical trends are often not described. Moreover, if MI compositions do not follow the main bulk rock trends, the significance of these anomalous MI compositions is not considered. It is important to note that all, or most, of the MI in the studies we cited (and in one case, conducted) may be representative of the bulk melt during differentiation, but the representativeness has not been rigorously evaluated. Thus, it remains unclear whether the variations in volatile contents observed in MI represent variations in the composition of melts in equilibrium with the growing crystal at the time of trapping, or instead are due to modifications after trapping.

In this study, we review published data for MI from the CF and IP volcanic areas (Arienzo et al., 2016; Arienzo et al., 2010; Cannatelli et al., 2007; Cecchetti et al., 2003; Cipriani et al., 2008; Esposito et al., 2011; Fourmentraux et al., 2012; Mangiacapra et al., 2008; Mormone et al., 2011; Roach, 2005; Stock et al., 2016), and we present new geochemical data obtained from MI from the CF and IP volcanic fields. The new data are from representative samples from the Neapolitan Yellow Tuff (NYT), Solchiaro, Bacoli, Agnano-Monte Spina (AMS), Solfatara, and Fossa Lupara eruptions. These new data supplement the database of MI compositions from the literature. We selected MI from the NYT, Bacoli, and Fossa Lupara eruptions because, to our knowledge, MI from these eruptions have not yet been studied. Moreover, the selected samples represent a significant range in time (~23.6 ka to 3.7 ka) and space within the CF and IP (Fig. 1). By conducting new analyses within a rigorous analytical protocol, our goal was to develop a better understanding of the reliability of MI as recorders of the pre-eruptive magma history at CF and IP. We compared compositions of MI from this study with those of bulk rocks and MI from the literature to better understand the correlation between MI and bulk rock compositions (Appendix Table A). The compiled literature data, combined with our new data, allow examination of possible correlations between the major element and volatile contents of MI and the compositions of host phenocrysts (mainly olivine, clinopyroxene, and sanidine). In addition, we compared compositions of experimentally reheated MI with data from naturally quenched MI. The selected MI data for CF and IP and mineral data were also compared with differentiation trends and mineral compositions predicted using rhyolite-MELTS simulations to better understand if crystallization occurred under volatile-saturated conditions (Ghiorso and Gualda, 2015). Finally, we describe in detail a protocol to test the representativeness of MI in the absence of melt inclusion assemblages. We demonstrate that re-evaluating MI data following the method employed here reduces uncertainty and instills confidence that the MI compositions are representative of the original pre-eruptive melt.

2. Geology and geochronology of Campi Flegrei and Procida Island

Campi Flegrei (CF) and Procida Island (IP) are part of the Phlegrean Volcanic District (PVD; Orsi et al., 1996). The PVD, along with the Somma-Vesuvius volcanic district, is part of the Campanian Comagmatic Province, which in turn is part of the circum-Tyrrhenian magmatic event that began in the Plio-Quaternary (Peccerillo, 1999 and references therein). Campanian magmatism is associated with NW-SE and NE-SW trending normal faults that reflect the extensional/transtensional tectonic regime of the Campanian margin (Milia, 2010 and references therein). The magmas generated in the CF and IP share a common origin dating back at least 40 ka (De Astis et al., 2004). The oldest volcanic products in the entire Campanian Plain do not outcrop but, rather, were collected from drill cores and give ages of 2.0 ± 0.4 Ma (Barbieri et al., 1979), ~1 Ma (Ippolito et al., 1975) and ~0.4 Ma (Brocchini et al., 2001).

2.1. Campi Flegrei

The Campi Flegrei (CF) volcanic field is located NW of Naples and is characterized by the presence of several volcanic cones, rings, and caldera structure(s). The volcanic framework at CF is interpreted by some researchers as representing a nested and resurgent caldera that is partially submerged under the Bay of Pozzuoli (Orsi et al., 1995; Orsi et al., 1992; Orsi et al., 1996; Perrotta et al., 2006) (Fig. 1). In this model, the outer caldera rim was formed during eruption of the Campanian Ignimbrite (CI), the largest eruption in the entire Campanian Plain, that occurred at ~39 ka (De Vivo et al., 2001; Rolandi et al., 2003), and the inner caldera was formed later by the Neapolitan Yellow Tuff (NYT) eruption at ~15 ka (Deino et al., 2004). While most workers agree that a caldera at CF was formed during the NYT eruption, both the existence of an outer caldera formed by the CI and the source of the CI are subjects to debate (Scandone et al., 2006). Rosi and Sbrana (1987), Orsi et al. (1996), and Piochi et al. (2013) suggest that the CI was erupted from a vent located in the center of the CF. In contrast, Scandone et al. (1991) suggest that the CI originated from the Acerra depression northeast of Naples. Another interpretation is that the CI was produced as the result of multiple fissure eruptions that occurred along faults associated with the local extensional tectonic regime (De Vivo et al., 2010; De Vivo et al., 2001; Rolandi et al., 2003). As summarized by De Vivo et al. (2010), these eruptions fed by regional faults range in age from > 300 ka to 39 ka. Recent findings based on a new borehole at CF support this latter hypothesis that the CI originated through fissure vents from outside of the CF (De Natale et al., 2016). In particular, these researchers reported that the volume of the NYT is 2.5 larger than that of the CI, and that the volume of the CI deposits contrasts with the hypothesis that the CI formed a caldera structure larger than that associated with the NYT. In addition, we note that there is some debate concerning the location of both the CI and the NYT caldera rims (e.g., Orsi et al., 1996; Perrotta et al., 2006; Rosi and Sbrana, 1987; Vitale and Isaia, 2014). Regardless of the origin of the CI, we do not include data from MI from CI in this assessment because (1) no basaltic or trachybasaltic MI are reported from this eruption (Marianelli et al., 2006; Signorelli et al., 1999; Webster et al., 2003) (2) it is generally not possible to determine from the published studies which MI are bubble-bearing and which are not, and (3) the origin of the CI and its possible genetic relationship to CF and IP are still under debate for the reasons mentioned above.

The oldest outcropping volcanic products in the CF volcanic field, dated at 58 ± 3 ka, are found only in escarpments in the northern part of CF (Pappalardo et al., 1999). Activity occurring in the interval between these oldest recognized eruptions and the eruption of the CI (~39 ka; De Vivo et al., 2001; Rolandi et al., 2003) is referred to as pre-CI activity. Pre-CI activity includes the Punta di Marmolite and Cuma lava domes (Gillot et al., 1982), two of the few lava domes at CF. Other mostly alkali-trachytic explosive eruptions have been recognized during the pre-CI activity (Pappalardo et al., 1999). A lithic breccia associated with an ignimbrite deposit and dated at ~39 ka (De Vivo et al., 2001; Rolandi et al., 2003) formed after this period of relatively minor volcanic activity. This lithic breccia, known as the Breccia Museo-Piperno formation, outcrops at many localities around the CF and some authors suggest that it represents the proximal phase of the CI (Orsi et al., 1996; Pappalardo et al., 1999; Perrotta et al., 2006). Various estimates of the volume of material erupted during the CI range from 80 km^3 (Thunell et al., 1979), to 150 km^3 (Civetta et al., 1997), to 200 km^3 (Rolandi et al., 2003), to 300 km^3 (Fedele et al., 2007) DRE. The estimated volume is related to the ignimbrite dated at ~39 ka by De Vivo et al. (2001).

Following the CI eruption, volcanic activity is characterized by several eruptions referred to as "tufi biancastri" (whitish tuffs) that occur mainly in eastern CF (Di Girolamo et al., 1984). These eruptions span a period from < 39 ka to 15 ka, at which time the NYT erupted. The age of the NYT is controversial because two different analytical methods give significantly different ages. The NYT has been dated at 12 ka using the ^{14}C method (Alessio et al., 1971) and at ~15 ka using the ^{39}Ar/^{40}Ar method (Deino et al., 2004). As mentioned above, the NYT is interpreted to be the eruption that formed the CF caldera, and the NYT deposits cover an area of 1000 km^2 and consist of 40 km^3 DRE (Orsi et al., 1992; Wohletz et al., 1995). Volcanic activity at CF that occurred after the NYT eruption is referred to as "recent activity" by Di Girolamo et al. (1984). Di Vito et al. (1999) grouped post-NYT activity into three epochs of volcanic activity: epoch I between ~15 and 10.6 ka; epoch II between ~9.6 and 9.1 ka; and epoch III between ~5.5 and 3.5 ka, based on a recalculated age reported by Smith et al. (2011). Di Vito et al. (1999) recognized 64 volcanic units that were deposited after the eruption of the NYT. The common characteristic of this recent activity is that eruptions were mostly explosive, generated from monogenetic centers, and produced a small amount of material compared to the NYT eruption. The eruptions of the first two epochs are located mainly near the periphery of CF, while more recent eruptions occurred mostly in the interior of CF. Recently, Lirer et al. (2011) recognized a new volcanic unit that they named Torretta. ^{14}C dating of samples from the Torretta unit revealed an age of 2.8 ka (Lirer et al., 2011). The Monte Nuovo eruption in 1538 CE represents the only historical eruption at CF, and a historical chronicle describes in detail the week-long eruption that formed a scoria cone (Da Toledo and Giacomo, 1539).

2.2. Procida

The Island of Procida (IP) represents the products of volcanic activity from five monogenetic volcanoes: Vivara, Terra Murata, Pozzo Vecchio, Fiumicello, and Solchiaro (De Astis et al., 2004; Di Girolamo et al., 1984; Di Girolamo and Stanzione, 1973; Pescatore and Rolandi, 1981; Rosi et al., 1988a; Rosi et al., 1988b). These volcanoes are aligned along a NE-SW trending volcanic belt that extends from the Island of Ischia southwest of IP to Monte di Procida to the northeast (Fig. 1). The importance of the NE-SW transverse faults that are associated with the Appennine (NW-SE) normal fault in the formation of the Procida Island volcanoes is noted in several studies (Acocella et al., 1999; De Astis et al., 2004; Orsi et al., 1996). The IP volcanism has likely been active over the last 80 ka, but no historical volcanic activity has been recorded (De Astis et al., 2004 and references therein). Volcanic deposits resulting from the activity of the five volcanoes are interlayered with deposits from higher magnitude eruptions sourced from Ischia Island and CF. The most recent eruptive materials on Procida are associated with the Solchiaro eruption. Paleosols at the base of the Solchiaro deposits have been dated at 17.3 ka and 19.6 ka, respectively by Lirer et al. (1991) and by Alessio et al. (1989). All of the paleosol ages were based on radiocarbon (^{14}C) measurements. Also, Alessio et al. (1989) reported an age of 14.3 ka for a paleosol above the Solchiaro deposits. This suggests that the last volcanic activity at Procida occurred between 19.6 ka and 14.3 ka. More recently, Morabito et al. (2014) recalibrated the 19.6 ka age reported by Alessio et al. (1989) to obtain an age of 23.624 ± 0.33 cal ka BP, moving the age of the Solchiaro eruption to an earlier time.

2.3. Genesis and differentiation of magma at Campi Flegrei and Procida Island

The CF and IP magmatism is part of the Quaternary magmatism that is characterized by high K$_2$O contents in relatively primitive melts (Peccerillo, 2017). The trend is defined by the potassic series starting from least evolved trachybasalts, continuing through shoshinites and latites, and ending with trachytes and phonolites (Suppl. Fig. 1a). There is no correlation between the age and compositional evolution of rocks erupted in the Phlegrean area. The more primitive magmas of the last 23.6 ka erupted along regional normal faults oriented NE-SW, along the NYT caldera border and continuing through Procida and Ischia Islands

(Acocella and Funiciello, 1999; De Astis et al., 2004; Orsi et al., 1996). The volume of trachyte is much larger than the combined volumes of trachybasalt, shoshonite and latite. In particular, the intermediate composition rocks represent the smallest volume of erupted products.

Bulk rock major element compositions show trends mostly consistent with simple fractional crystallization (D'Antonio, 2011 and references therein), in which olivine is the predominant mineral phase in the least evolved members. Clinopyroxene is present throughout the entire differentiation trend and predominates in the intermediate members, and sanidine is more abundant in the more evolved stages. Plagioclase also crystallized along the trend, with accessory phases chromite, Ti-magnetite, apatite and biotite observed. Melluso et al. (2012) calculated that ~90% of fractional crystallization (alkali-feldspar, plagioclase, clinopyroxene and olivine in order of abundance) is required to generate the trachyte-phonolites from the latitic bulk composition of CF. However, simple fractional crystallization models cannot explain either the variability of K for the least evolved rocks, nor the K-enrichment of some of the more evolved rocks. Other elements (e.g., Cl, Sb) show similar anomalous variability and enrichment (Villemant, 1988). The combination of isotopic and trace element data suggests that a mechanism of percolation of fluids from the wall rock into the magma reservoir caused selective enrichment of K–Sb–Cl during fractional crystallization (Civetta et al., 1991; Villemant, 1988).

In several studies, the large variation of CO_2 and H_2O concentrations of MI at CF and IP is interpreted as the combination of continued degassing of volatile-saturated magmas during ascent and multiple CO_2 fluxing events (Arienzo et al., 2016; Arienzo et al., 2010; Mangiacapra et al., 2008; Mormone et al., 2011). In addition, Moretti et al. (2013) studied major elements and volatiles in trachybasaltic and shoshonitic MI from Ischia Island (West/South-West from CF and IP) and discussed the importance of CO_2 fluxing for the geochemical evolution of magmas associated with Neapolitan volcanism. It is important to note that studies advocating the importance of CO_2 fluxing corroborate the hypothesis of selective enrichment of K, Sb, and Cl by percolation of fluids through magmas at CF (Civetta et al., 1991; Villemant, 1988). However, D'Antonio and Di Girolamo (1994) noted that the selective enrichment of K–Sb–Cl in mafic rocks from IP is accompanied by the enrichment of other trace elements that are not compatible with fluids (e.g., Nb). In addition, "shrinkage" bubbles in MI are reported in the MI from studies advocating CO_2 fluxing, raising concerns about the reliability of the volatile data recorded by MI (i.e., did the MI trap some CO_2 along with melt?). Alternatively, D'Antonio and Di Girolamo (1994) invoked mixing between magma batches showing different degrees of evolution (e.g., trachybasalt and latite) and having different Sr-isotopic signatures to explain the observed trends.

There is a general agreement regarding the depth at which extensive crystallization and possible CO_2 fluxing occurred (and is occurring) beneath the CF and IP volcanic fields. Seismic reflection data suggest a partial melting zone ~1 km thick at 7.5 km beneath CF. In agreement with geophysical data, data from MI suggest that extensive crystallization and CO_2 fluxing occurred at ~200 MPa (Arienzo et al., 2010; Mangiacapra et al., 2008; Moretti et al., 2013).

Several hypotheses have been proposed for magma generation in the Phlegrean area. Many researchers argue that magmatism originated from an intraplate-type mantle source that was subsequently metasomatized by slab-derived fluids (Peccerillo, 2017 and references therein). Trace element data for CF and IP mafic magmas are enriched in LILE and LREE relative to MORB, and the trace element patterns are similar to those of intraplate basalts. In contrast, Ti, Y, and Yb are depleted relative to MORB and the HFSE show lower degrees of enrichment relative to LILE and LREE, characteristics of an arc-type signature (De Astis et al., 2004; Peccerillo, 1999 and references therein).

Volcanic rocks erupted from the CF volcanic field during the last 60 ka show highly variable isotopic compositions. In particular, the $^{87}Sr/^{86}Sr$ ratio varies from ~0.7065 to 0.7086, $^{143}Nd/^{144}Nd$ varies from ~0.5124 to 0.5128, $^{206}Pb/^{204}Pb$ from ~18.90 to 19.25, $^{207}Pb/^{204}Pb$

from ~15.65 to 15.77, and $^{208}Pb/^{204}Pb$ from ~38.95 to 39.38 (see Peccerillo 2017, Chapter 7 and references therein). The isotopic data document a general increase in $^{87}Sr/^{86}Sr$ and decrease in $^{143}Nd/^{144}Nd$ and $^{206}Pb/^{204}Pb$ from older to younger rocks. However, the same $^{87}Sr/^{86}Sr$ increase and $^{143}Nd/^{144}Nd$ and $^{206}Pb/^{204}Pb$ decrease is noted with increasing MgO content (Suppl. Fig. 1b). The isotopic variability indicates that simple fractional crystallization cannot be the only process responsible for the geochemical trends defined by rocks of the CF volcanic field. Pappalardo et al. (2002) interpret the correlation between $^{87}Sr/^{86}Sr$ and age to reflect crustal contamination. Thus, the younger erupted magmas would have resided in the crust for a longer time, underwent more extensive crustal contamination and, therefore, show higher $^{87}Sr/^{86}Sr$. However, it is important to note that the age - isotopic signature correlation is not observed if only the NYT and post-NYT bulk rock data are examined (Di Renzo et al., 2011). It is also worth noting that the NYT shows homogeneous Sr-isotope ratios, and based on this Gebauer et al. (2014) suggest minimal wall rock contamination for NYT magmas. In contrast with the interpretation of Pappalardo et al. (2002), Peccerillo (2017) argues that the correlation between isotopic composition and MgO may suggest that hotter and less viscous mafic magmas experience more contamination relative to more evolved, cooler and more viscous magmas, as has been invoked for Alicudi volcano in the Aeolian arc (Peccerillo 2017, and references therein). According to this latter interpretation, the isotopic variability is not necessarily controlled by residence time of magmas in the crust.

Although most of the major element trends at IP suggest simple fractional crystallization, variability of incompatible elements and variability of isotopic composition of bulk rocks suggest that open-system magmatic processes must have also been involved. The most mafic rocks in the Campanian Province are found in the IP, with few of the lithic lava clasts considered to be primitive (MgO up to ~11.5 wt% and Ni up to ~230 ppm; D'Antonio et al., 1999a). In addition, a juvenile sample from the Solchiaro I deposits at IP indicates that lower Sr-isotopic ratios in the CF and IP (~0.7052) are not restricted to lithic lava clasts (De Astis et al., 2004). The $^{87}Sr/^{86}Sr$ (0.7051 to 0.7065) of IP bulk rocks is lower than that of CF rocks, and vice versa for $^{143}Nd/^{144}Nd$. D'Antonio et al. (2007) recognize two trends based on ^{11}B and $^{206}Pb/^{204}Pb$ versus $^{87}Sr/^{86}Sr$ systematics of bulk rocks from CF, IP, and Ischia Island. They interpret one trend to represent contamination of the mantle source by slab-derived fluids or sediment-derived melts. In particular, the CF rocks are interpreted to have been generated by a transitional MORB-type asthenospheric mantle contaminated by sediment-derived melts, while the IP rocks were generated by the same mantle source contaminated by slab-derived fluid. The other trend records crustal contamination during crystallization of volcanic rocks younger than 39 ka. In addition, D'Antonio et al. (2007) suggest that some rocks younger than 39 ka were affected by mixing-mingling processes between chemically and isotopically distinct magmas, based on disequilibria among minerals and groundmass. Mazzeo et al. (2014) also studied lithic lava clasts from the Solchiaro deposits at IP and hypothesized that the mantle wedge from which primary magmas at IP were sourced was contaminated by 2–4% of slab-derived components represented by partial melts from shale and carbonates, and aqueous fluids from the slab. It is important to note that the mafic rocks from CF are not primitive. Consequently, Pappalardo et al. (2002) and Peccerillo (2017) emphasize that an interpretation whereby the difference in isotopic composition between CF and IP is related to different types of contamination of the source is speculative.

3. Sample description

Six new samples were collected to supplement existing data from the two volcanic areas. Five are from CF and one is from the IP. The CF samples are representative of five volcanic units erupted at different times in this volcanic field. The six eruptions sampled are, from oldest to youngest: Fossa Lupara (also named Senga in the literature),

Table 1
Sample details and petrographic description of MI from this study.

Sample	Eruption	Sample type	Host phase	Zonation	Size (μm)	Mi shape	Bubbles in MI	Heated/natural	T quench °C	Notes
Normal MI										
RE.PR11.A13.M1	NYT	Unconsolidated yellow tuff	cpx		60 × 30	Ovoid elongated	na	natural		
RE.PR11.D14.M1	NYT	Unconsolidated yellow tuff	cpx		50	Spherical	na	natural		
RE.PR11.D15.M1	NYT	Unconsolidated yellow tuff	cpx		90	Spherical	na	natural		
RE.PR11.D19.M1	NYT	Unconsolidated yellow tuff	cpx	xl zoned	50 × 30	Ovoid	no bubble	natural		
RE.PR11.D23.M1	NYT	Unconsolidated yellow tuff	cpx		110 × 40	Ovoid elongated	no bubble	natural		
RE.PR11.D23.M2	NYT	Unconsolidated yellow tuff	cpx		110 × 40	Ovoid elongated	no bubble	natural		
RE.PR11.D7.M1	NYT	Unconsolidated yellow tuff	cpx	xl zoned	50	spherical	no bubble	natural		
RE.PR11.F12.M1	NYT	Unconsolidated yellow tuff	san		70 × 100	ovoid	multiple	natural		
RE.PR11.F12.M2	NYT	Unconsolidated yellow tuff	san		70 × 100	ovoid	multiple	natural		
RE.PR11.F2.M1	NYT	Unconsolidated yellow tuff	san		50 × 30	ovoid	1 bubble	natural		
RE.PR11.F21.M1	NYT	Unconsolidated yellow tuff	san		80 × 100	ovoid	no bubble	natural		
RE.PR11.F21.M2	NYT	Unconsolidated yellow tuff	san		30 × 50	ovoid	no bubble	natural		
RE.PR11.F21.M3	NYT	Unconsolidated yellow tuff	san		30 × 60	ovoid	no bubble	natural		
RE.PR11.F22.M1	NYT	Unconsolidated yellow tuff	san		70 × 50	ovoid	no bubble	natural		
RE.PR11.F22.M2	NYT	Unconsolidated yellow tuff	san		50 × 40	ovoid	no bubble	natural		
RE.PR11.F4.M1	NYT	Unconsolidated yellow tuff	san	xl zoned	35	spherical	2 bubbles	natural		
RE.PR11.F5.M1	NYT	Unconsolidated yellow tuff	san		40	spherical	1 bubble	natural		
RE.S08.D11.M2	Solfatara	Grey tuff, base surge	cpx		50 × 25	irregular	multiple	natural		
RE.S08.D13.M1	Solfatara	Grey tuff, base surge	cpx	xl zoned	55 × 110	ovoid	na	natural		
RE.S08.D13.M4	Solfatara	Grey tuff, base surge	cpx	xl zoned	35 × 25	ovoid	na	natural		
RE.S08.D13.M5	Solfatara	Grey tuff, base surge	cpx	xl zoned	35	spherical	na	natural		
RE.S08.D2.M1	Solfatara	Grey tuff, base surge	cpx		45	spherical	na	natural		
RE.S08.D2.M2_av	Solfatara	Grey tuff, base surge	cpx		60 × 35	negative crystal shape	na	natural		
RE.S08.D2.M3	Solfatara	Grey tuff, base surge	cpx		50 × 30	irregular	na	natural		
RE.S08.D2.M4	Solfatara	Grey tuff, base surge	cpx		25	spherical	na	natural		
RE.S08.D4.M1	Solfatara	Grey tuff, base surge	cpx	xl zoned	180 × 50	irregular	multiple	natural		
RE.S08.D4.M2	Solfatara	Grey tuff, base surge	cpx	xl zoned	40 × 30	ovoid	1 bubble	natural		
RE.S08.D4.M3	Solfatara	Grey tuff, base surge	cpx	xl zoned	120 × 50	irregular	multiple	natural		
RE.S08.D4.M4	Solfatara	Grey tuff, base surge	cpx	xl zoned	120 × 100	irregular	multiple	natural		
RESO8.D7.M1	Solfatara	Grey tuff, base surge	cpx	xl zoned	53 × 39	ovoid	reported	natural		
RESO8.D7.M2	Solfatara	Grey tuff, base surge	cpx	xl zoned	26	spherical	reported	natural		
RESO8.D7.M3	Solfatara	Grey tuff, base surge	cpx	xl zoned	30 × 39	ovoid	reported	natural		
RE.S08·F1.M1	Solfatara	Grey tuff, base surge	san	xl zoned	200 × 120	irregular	multiple	natural		
RE.S08·F1.M2	Solfatara	Grey tuff, base surge	san	xl zoned	200 × 120	irregular	multiple	natural		
RE.S08·F1.M3	Solfatara	Grey tuff, base surge	san	xl zoned	30 × 40	ovoid	1 bubble	natural		
RE.S08·F1.M4	Solfatara	Grey tuff, base surge	san	xl zoned	20	spherical	no bubble	natural		
RE.S08·F1.M5	Solfatara	Grey tuff, base surge	san	xl zoned	150 × 70	irregular	multiple	natural		
RE.S08·F10.M1	Solfatara	Grey tuff, base surge	san	xl zoned	80	spherical	4 bubble	natural		oxide associated
RE.S08·F12.M1	Solfatara	Grey tuff, base surge	cpx		120 × 49	negative crystal shape	1 bubble	natural		oxide associated
RE.S08·F12.M2	Solfatara	Grey tuff, base surge	san		120 × 49	negative crystal shape	1bubble	natural		oxide associated
RE.S08·F16.M1	Solfatara	Grey tuff, base surge	san		140 × 100	ovoid	multiple	natural		
RE.S08·F6.M1	Solfatara	Grey tuff, base surge	san	xl zoned	54 × 39	ovoid	multiple	natural		
RE.S08·F6.M2	Solfatara	Grey tuff, base surge	san	xl zoned	84 × 42	irregular	1 bubble	natural		
RE.S08·F6.M3	Solfatara	Grey tuff, base surge	san	xl zoned	37	spherical	1 bubble	natural		
RE.S08·F8.M1	Solfatara	Grey tuff, base surge	san		40 × 20	ovid elongated	na	natural		
RE.SC2.A10.M1	Solchiaro	Grey tuff, base surge	cpx	xl zoned	35	spherical	1 bubble	natural		wrinkled interface
RE.SC2.A10.M2	Solchiaro	Grey tuff, base surge	cpx	xl zoned	35 × 70	ovoid	multiple	natural		wrinkled interface
RE.SC2.D11.M1	Solchiaro	Grey tuff, base surge	cpx	xl zoned	105 × 75	ovoid	1 bubble	natural		
RE.SC2.D11.M3	Solchiaro	Grey tuff, base surge	cpx	xl zoned	35 × 25	ovoid	1 bubble	natural		

Table 1 (continued)

Sample	Eruption	Sample type	Host phase	Zonation	Size (µm)	Mi shape	Bubbles in MI	Heated/ natural	T quench °C	Notes
RE.SC2-F2.M1av	Solchiaro	Grey tuff, base surge	san		100 × 70	irregular	na	natural		
RE.SC2-F2.M3	Solchiaro	Grey tuff, base surge	san		50 × 25	irregular	1 bubble	natural		
RE.SC2-F4.M1	Solchiaro	Grey tuff, base surge	san		100 × 120	negative crystal shape	no bubble	natural		apatite associated
RE.SC2-F4.M2	Solchiaro	Grey tuff, base surge	san		50 × 30	ovoid	no bubble	natural		
RE.SC2-F5.M1	Solchiaro	Grey tuff, base surge	san		50 × 40	irregular	multiple	natural		
RE.SC2-F5.M2	Solchiaro	Grey tuff, base surge	san		50 × 80	negative crystal shape	no bubble	natural		
RE.SC2-F7.M1	Solchiaro	Grey tuff, base surge	san	xl zoned	110 × 35	irregular	1 bubble	natural		
RE.SE17.AD9.m5	Fossa lupara	Scoriaceous lapilli	cpx		80 × 50	negative crystal shape	na	heated	1200	
RE.SE17.AD9.m6	Fossa lupara	Scoriaceous lapilli	cpx		75 × 50	negative crystal shape	na	heated	1200	
RE.SE17.AD9.m7	Fossa lupara	Scoriaceous lapilli	cpx		70 × 35	negative crystal shape	na	heated	1200	
RE.SE17.D13.M1	Fossa lupara	Scoriaceous lapilli	cpx	xl zoned	70 × 25	sub-ovoid	multiple	heated	1200	
RE.SE17.F4.M1	Fossa lupara	Scoriaceous lapilli	san		40 × 60	irregular	multiple	heated	1070	
RE.SE17.F4.M2	Fossa lupara	Scoriaceous lapilli	san		40 × 30	negative crystal shape	multiple	heated	1070	
RE.SE17.f6.m1	Fossa lupara	Scoriaceous lapilli	san		57 × 75	negative crystal shape	3 bubbles	heated	1070	
RE.SE17.f6.m2	Fossa lupara	Scoriaceous lapilli	san		57 × 75	negative crystal shape	3 bubbles	heated	1070	
REBA1.F2.M1	Bacoli	Yellow tuff	plg		na	na	na	natural		
REBA1.F3.M1	Bacoli	Yellow tuff	plg		na	na	na	natural		
REBA1.F34.M2	Bacoli	Yellow tuff	plg		na	na	na	natural		
REBA1.F7.M1	Bacoli	Yellow tuff	san		na	na	na	natural		
REMS12-C4.M1	AMS	Pumice	cpx		na	na	na	natural		
REMS12-C4.M2	AMS	Pumice	cpx		na	na	na	natural		
REMS12-C4.M3	AMS	Pumice	cpx		na	na	na	natural		
REMS12-C5.M1	AMS	Pumice	cpx		na	na	na	natural		
REMS12-C5.M2	AMS	Pumice	cpx		na	na	na	natural		
REMS12-C6.M1	AMS	Pumice	cpx		na	na	na	natural		
REMS12-C7.M1	AMS	Pumice	cpx		na	na	na	natural		
REMS12-C7.M2	AMS	Pumice	cpx		na	na	na	natural		
REMS12-C7.M3	AMS	Pumice	cpx		na	na	na	natural		
Anomalous MI										
RE.PR11.A13.M2	NYT	Unconsolidated yellow tuff	cpx	na	45	spherical	1	natural		
RE.SC2.D11.M2	Solchiaro	Grey tuff, base surge	cpx	xl zoned	na	na	na	natural		
RE.SC2.A10.M3	Solchiaro	Grey tuff, base surge	cpx	xl zoned	na	na	na	natural		
RE.SE17.F7.M2	Fossa lupara	Scoraiceous lapilli	san	xl zoned	305 × 70	ovoid	multiple	heated	1070	
RE.SE17.D13.M2	Fossa lupara	Scoriaceous lapilli	cpx	xl zoned	45 × 25	ovoid	no bubbles	heated	1200	
RE.SE17.AD9.m2	Fossa lupara	Scoriaceous lapilli	cpx		40	spherical	1 bubble	heated	1200	
RE.SE17.AD12.m2av	Fossa lupara	Scoriaceous lapilli	cpx	xl zoned	60 × 25	irregular	no bubbles	heated	1200	
RE.SE17.AD12.m1av	Fossa lupara	Scoriaceous lapilli	cpx	xl zoned	60 × 50	irregular	no bubbles	heated	1200	
REBA1.P6.M3	Bacoli	Yellow tuff	plg	na	na	na	na	natural		
REBA1.P6.M2	Bacoli	Yellow tuff	plg	na	na	na	na	natural		
REBA1.P6.M1	Bacoli	Yellow tuff	plg	na	na	na	na	natural		

Solfatara, Agnano-Monte Spina, Bacoli, and Neapolitan Yellow Tuff for CF, and Solchiaro from the IP (Table 1 and Appendix Table A).

The Fossa Lupara sample (RESE17: Fig. 1) consists of black, sharp-edged scoriae < 20 mm. The Fossa Lupara eruption has been dated at 3.82 ka by Di Vito et al. (1999), and Smith et al. (2011) recalculated the age to be 3.98–4.20 ka using a more recently developed and more precise method to interpret the isotopic data. The scoriae were selected from Fossa Lupara deposits ejected during the intermediate stages of the eruption (Lirer et al., 2011). The scoriae are porphyritic with abundant phenocrysts of clinopyroxene and subordinate sanidine and were sampled at the northeast sector of the crater associated with this eruption.

One sample representative of the upper deposits of the Solfatara eruption was collected close to the northwest crater rim of Solfatara (RESO8: Fig. 1), and consists of centimeter-scale fragments of rounded pumice contained in pyroclastic brownish ash layers. The pumices contain abundant sanidine and clinopyroxene. The age of the Solfatara eruption was recalculated from earlier data to be 4.15–4.35 ka by Smith et al. (2011) based on chronological data reported by Di Vito et al.

(1999) and by Isaia et al. (2009).

The Agnano-Monte Spina sample (REMS12: Fig. 1) was collected ~200 m southwest from the top of Monte Spina. The age of the AMS eruption was recalculated from earlier data to be 4.48-4.62 ka (Smith et al., 2011 and references therein). The sample consists of sharp-edged pinkish-grey pumices representing a 30-cm thick layer. The pumices are well sorted, characteristic of a fallout deposit. This layer of pumice also shows reverse grading suggesting that some changes occurred during the deposition such us (1) progressive increase in initial gas velocity, (2) change in vent morphology or, (3) increase in eruption column density (Self, 1976 and references therein). Abundant sanidine, clinopyroxene, rare biotite and olivine were observed.

The Bacoli sample (REBA1: Fig. 1) was collected close to the northern rim of the crater of the Bacoli volcanic formation in the western rim of CF caldera (12.8 ka, Di Renzo et al., 2011; 8.58 ka, Fedele et al., 2011; 11.51–14.15 ka, Smith et al., 2011). The sample consists of a yellow tuff containing abundant isolated euhedral sanidine and clinopyroxene phenocrysts.

The Neapolitan Yellow Tuff sample (14.9 ka; Deino et al., 2004) was

collected from the eastern caldera rim (northwestern part of Naples urban area, Ponti Rossi; REPR11: Fig. 1). The sample consists of ash fall deposits with abundant sanidine and clinopyroxene phenocrysts representing the unlithified facies of the NYT (this deposit is referred to as Pozzolana, the material used for concrete production in Roman times). We selected only single phenocrysts showing euhedral habit and rim glass to avoid including xenocrysts in our sample suite.

The Solchiaro sample (RESC2: Fig. 1) was collected on the northeastern coast of IP and represents the distal unlithified facies of the Solchiaro deposits. The sample consists of grey ash, brown lapilli, and isolated olivine, clinopyroxene, and sanidine crystals [sample RESC2 in Esposito et al. (2011)].

4. Analytical methods

The samples selected for this study were gently crushed and individual phenocrysts were hand-picked from the crushed material under a binocular microscope. Each phenocryst was mounted on a 2.5 mm-diameter glass rod (Esposito et al., 2014; Thomas and Bodnar, 2002) using Crystalbond™ cement. Phenocrysts were polished on the top and bottom surfaces and those crystals containing rounded to regular-shaped MI were selected for study. After we selected 20–30 crystals (depending on size), the phenocrysts were pressed into a one-inch diameter indium mount. Indium was used as the mounting medium to prevent H–C contamination during secondary ion mass spectrometric (SIMS) analysis, as occurs when epoxy mounts are used.

MI in the Fossa Lupara sample and one MI hosted in sanidine from the Agnano Monte Spina sample were partially to completely crystallized as found. We performed heating experiments on the crystallized MI using a Vernadsky heating stage (Sobolev et al., 1980). The heating stage was calibrated according to the 1-atm melting temperatures of silver (962 °C) and gold (1064 °C). During the heating experiment, a continuous flow of He into the furnace of the heating stage prevented (or minimized) Fe-oxide formation on the surface of Fe-rich phenocrysts. MI were heated until the T of homogenization (MI containing only silicate melt) was reached. Following homogenization, the sample was quenched rapidly to room temperature. The T uncertainty is $\sim \pm 5\,°C$ at 1064 °C. Heating rates were varied during the run, depending on phase behavior of the MI (Esposito et al., 2012).

The major element compositions of glasses and minerals were determined first using a JEOL JXA 8900 electron microprobe (EMP) at the USGS (Reston, VA, USA). The analyses were conducted using an accelerating voltage of 15 kV. The beam current was 10 nA and a defocused beam of 10 μm diameter was used. For oxide concentrations > 1 wt%, 1-sigma errors are < 2% relative, while for oxide concentrations < 1 wt%, 1 sigma errors are generally < 10% relative. Additional information relative to EMP standards used for the analyses are included in Appendix Table B.

Following EMP analyses, volatile elements (O, H, C, F, S, Cl) were measured by SIMS (Cameca IMS 1280) at the Woods Hole Oceanographic Institution (Woods Hole, MA, USA). We performed the analyses using $^{133}Cs^+$ as the ion source and the current varied between 1.0 and 1.6 nA. For each spot analyzed, the surface of the sample was pre-sputtered for 290 s to remove surface contamination. The size of the rastered area was 30 μm × 30 μm, and a 15 μm × 15 μm spot in the center of the rastered area was analyzed from 10 to 15 times in depth profile mode. We tuned the SIMS to count ions related to masses ^{16}O, ^{1}H, ^{12}C, ^{19}F, ^{32}S, ^{35}Cl, and ^{30}Si. Ratios between ion counts per unit time of each mass measured and ion counts per unit time of ^{30}Si were used to quantify the volatile contents. Six basaltic to basaltic-andesitic glass standards were used for calibration of the SIMS, and additional information on the glass standards is reported by Helo et al. (2011). For the SIMS measurements, using glass standards with silicate compositions that differ from MI compositions may introduce a matrix effect. However, Hauri et al. (2002) showed that SIMS calibration curves for H_2O, CO_2, F, S, and Cl obtained using rhyolitic, andesitic, and basaltic

glass standards do not show significant differences below certain absolute concentrations – specifically, for H_2O contents < 2 wt% and CO_2 contents < 1000 ppm. Most of the volatile concentrations of the MI reported in this study are below these upper limits. We used the calibration curves of Esposito et al. (2011) to calculate volatile concentrations in MI. To avoid contamination from the C-coating used for earlier EMP analysis, we adopted a specific protocol (see also discussion by Esposito et al. 2014) to remove the C coating. In particular, ~5 μm of sample was removed by polishing following EMP and before SIMS analysis, and the SIMS analytical area was pre-sputtered for 290 s before data collection started. We selected only flat depth profiles whereby the C counts did not vary significantly with depth, and we continuously monitored the ion-count response image to confirm a homogeneous carbon signal across the rastered area during analysis. Relative precision for CO_2, H_2O, F, Cl, and S by SIMS is < 10% relative, based on repeated analysis of glass standards (see Esposito et al., 2014; their Fig. 14).

5. Results

5.1. Petrography of melt inclusions

Many (but not all) of the phenocrysts examined contain MI and other mineral inclusions. Fluid inclusions are rare in the phenocrysts studied. Various types of MI, based on phases present at room temperature, were observed in all five samples as described below.

Sanidine, clinopyroxene, and plagioclase from Bacoli, Solfatara, Solchiaro, and NYT samples contain MI filled with mostly glass. Most of these naturally glassy MI contain one bubble in addition to the glass phase, and some contain glass plus bubble(s) plus an associated mineral (most commonly apatite). In a few cases, naturally glassy MI contain only glass (bubble-free MI). MI containing more than one bubble are found mostly in sanidine phenocrysts. This is thought to represent bubble formation in the MI after the melt has become sufficiently viscous to prevent the multiple bubbles from coalescing into a single bubble. Bubble-bearing MI (glass plus one bubble) show similar volume fractions of vapor (i.e., $volume_{bubble}/volume_{MI}$) in single phenocrysts selected for our study, and the proportion of vapor never exceeds 5 vol %, suggesting that the vapor bubble nucleated after trapping of a homogeneous silicate liquid (Moore et al., 2015), i.e., vapor bubbles were not trapped along with the melt. It is important to note that NYT MI show a larger proportion of bubble-free MI relative to MI from the other CF and IP eruptions studied.

The phenocrysts selected from Agnano-Monte Spina and Fossa Lupara samples contain partially to totally crystallized MI, in addition to naturally glassy MI as described above. In particular, MI in sanidine from Agnano-Monte Spina are sometimes found partially or totally crystallized, while partially crystallized MI are rarely found in clinopyroxene. Most of the Fossa Lupara phenocrysts contain partially to totally crystallized MI, but sometimes sanidine phenocrysts contain naturally glassy MI. Some sanidine phenocrysts in the Fossa Lupara sample show decrepitation halos, suggesting that the MI developed high fluid pressures after trapping and have lost some of their volatiles via fracturing of the surrounding host (Cannatelli et al., 2016).

In general, MI in all samples are ovoid or negative-crystal shape, but sometimes slightly to highly irregular shapes were observed (Table 1). For this study, we selected mostly regularly shaped MI because irregularly-shaped MI are more likely to have leaked or were in communication with the melt adjacent to the growing crystal for a prolonged period of time, (Humphreys et al., 2008a; Humphreys et al., 2008b; Welsch et al., 2013) or represent MI that have decrepitated (Maclennan, 2017). In addition, irregularly shaped MI hosted in plagioclase may be the result of dissolution reactions and record a chemical composition that is not representative of the melt in equilibrium with the host (Nakamura and Shimakita, 1998). Size ranges from a few microns to ~300 μm considering the longest dimension, and we selected only

MI > 20 μm to assure that analytical spots for EMP and SIMS would be contained entirely within the MI, thus avoiding contributions from the surrounding host. Most of the MI are isolated in the cores of phenocrysts without any geometrical correlation with their host (i.e., the MI are not obviously aligned along crystal growth surfaces). Some phenocrysts contain more than one MI. Consistent with the results of Esposito et al. (2014), MIA are rarely observed; where they are, individual MI are < 20 μm, a size that is smaller than the optimal instrumental conditions for analyzing volatiles.

5.2. Microthermometry

As mentioned above, most of the Fossa Lupara MI were crystallized as found. For this reason, we performed heating experiments using a Vernadsky heating stage to produce a homogenous glass before analysis. All MI-bearing clinopyroxenes from Fossa Lupara show a homogeneous silicate melt phase upon heating to ~1200 °C and all were quenched at this temperature. Most MI contain only glass after quenching from ~1200 °C, but some MI developed a vapor bubble during quenching. MI in sanidine phenocrysts from Fossa Lupara were quenched from ~1070 °C and most MI show only glass after quenching.

5.3. Major element compositions

Major element concentrations of MI are plotted on Harker diagrams versus SiO_2 (Fig. 2). The major element compositions of MI from this study (Table 2) overlap with published MI compositions (Arienzo et al., 2016; Arienzo et al., 2010; Cannatelli et al., 2007; Cecchetti et al.,

2003; Cipriani et al., 2008; Esposito et al., 2011; Fourmentraux et al., 2012; Mangiacapra et al., 2008; Mormone et al., 2011; Roach, 2005; Stock et al., 2016) and with bulk rock compositions from the literature (Albini et al., 1977; Beccaluva et al., 1991; Brocchini et al., 2001; Cannatelli et al., 2007; Capaldi et al., 1972; D'Antonio et al., 1999a; D'Antonio et al., 1999b; De Astis et al., 2004; de Vita et al., 1999; Di Girolamo et al., 1984; Di Vito et al., 2011; Ghiara et al., 1979; Mastrolorenzo and Pappalardo, 2006; Orsi et al., 1995; Orsi et al., 1992; Pappalardo et al., 2002; Piochi et al., 2005; Piochi et al., 2008; Scarpati et al., 1993; Tonarini et al., 2009; Tonarini et al., 2004; Turi et al., 1991; Villemant, 1988; Wohletz et al., 1995) (Fig. 2).

Compositions of MI studied here define differentiation trends with higher degrees of scatter relative to trends defined by bulk rock compositions – this is similar to trends defined by data for MI from the literature. In particular, at the same SiO_2 concentration, some major element concentrations (e.g., K_2O and Na_2O) span a wider range compared to that for the bulk rocks (Fig. 2). This behavior is commonly observed in MI studies (Kent, 2008, and references therein). In general, the major element concentrations of MI plotted as a function of SiO_2 show continuous differentiation trends (Fig. 2 a, b, d, and e). MI compositions from this study mostly agree with differentiation trends for bulk rocks, representing mainly fractional crystallization dominated by olivine plus clinopyroxene crystallization for less evolved magmas, clinopyroxene for intermediate magmas, and sanidine plus clinopyroxene crystallization for more evolved magmas.

Differentiation trends for TiO_2, FeO_{tot}, and P_2O_5 (Fig. 2), as well as for Al_2O_3, show poorer agreement compared to trends defined by bulk rock compositions from the literature. This behavior is consistent with
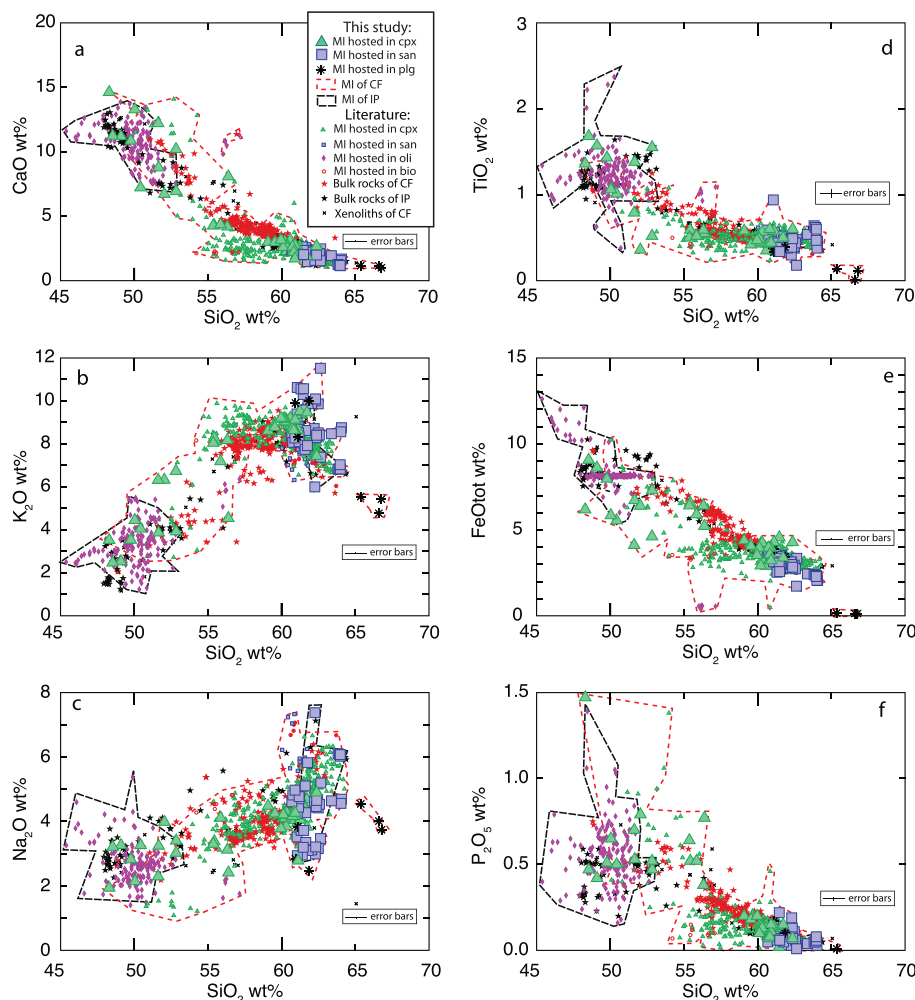

Fig. 2. Major element compositions of MI. The six panels represent plots of SiO_2 concentration versus (a) CaO, (b) K_2O, (c) Na_2O, (d) TiO_2, (e) FeO_{tot} and (f) P_2O_5. Large symbols represent MI analyzed in this study (triangles = MI hosted in clinopyroxene; squares = MI hosted in sanidine; asterisks = MI hosted in plagioclase). Small symbols represent data from the literature (triangles = MI hosted in clinopyroxene; squares = MI hosted in sanidine; diamonds = MI hosted in olivine; circles = MI hosted in biotite). Bulk rock data from the literature are shown as stars (red stars = CF; black stars = IP) and xenoliths of CF are shown as x's. The red-dashed line encircles the range in compositions of MI from CF, and the black-dashed line encircles the range in compositions of MI from IP. Estimated uncertainties for the data from the present study are shown as error bars in the lower-right of each panel. See text for sources for the bulk rock and MI data from the literature. (For interpretation of the references to colour in this figure legend, the reader is referred to the web version of this article.)

Table 2
Major element and volatile compositions of MI from this study.

Normal MI Sample	SiO₂ (wt%)	TiO₂	Al₂O₃	FeO_tot	MnO	MgO	CaO	Na₂O	K₂O	P₂O₅	Cl (ppm)	F	S	H₂O (wt%)	CO₂ (ppm)	total (wt%)	major elements only total	host phase	wo (mol%)	en	fs	An	Ab	Or
RE.PR11.A13.M1	52.49	0.51	18.61	4.86	0.13	1.77	7.52	2.24	4.23	0.71	5515	2063	2239	1.30		94.19	93.08	cpx	45.83	47.71	6.46			
RE.PR11.D14.M1	59.27	0.45	17.32	2.95	0.12	0.46	2.15	4.25	8.16	0.07	4970	1567	470	2.00		97.31	95.19	cpx	48.21	36.39	15.40			
RE.PR11.D15.M1	58.44	0.34	17.55	3.56	0.16	0.69	2.40	3.13	8.93	0.16	3290	2751	622	2.51	256	98.03	95.37	cpx	47.42	38.84	13.74			
RE.PR11.D19.M1	58.67	0.52	16.82	3.12	0.17	0.38	2.14	4.12	8.02	0.09	6671	2362	577	1.48	1046	97.75	94.04	cpx	47.95	33.60	18.45			
RE.PR11.D23.M1	60.45	0.41	17.71	3.02	0.17	0.39	2.30	4.34	8.26	0.03	5861	2382	575	1.50		99.51	97.07	cpx	48.10	35.32	16.58			
RE.PR11.D23.M2	60.44	0.45	17.39	3.16	0.18	0.33	2.14	4.47	8.18	0.03	5899		348			96.77	96.77	cpx	48.10	35.32	16.58			
RE.PR11.D7.M1	59.36	0.40	17.67	3.12	0.10	0.44	2.44	4.50	8.12	0.05	5653	1670	557	1.11		98.64	96.19	cpx	46.71	38.84	14.46			
RE.PR11.F12.M1	61.28	0.44	17.23	1.97	0.11	0.16	1.62	4.49	8.37	0.00	4421	2503	173	1.67		97.42	95.66	san				2.67	21.23	76.1
RE.PR11.F12.M2	61.45	0.36	17.71	1.99	0.17	0.17	1.51	4.38	8.22	0.03	5042		96			95.99	95.99	san				2.67	21.23	76.1
RE.PR11.F2.M1	60.95	0.52	17.46	2.35	0.13	0.24	1.88	4.46	8.15	0.04	5826		276			96.18	96.18	san				2.48	20.12	77.4
RE.PR11.F21.M1	60.56	0.37	17.74	2.73	0.12	0.51	2.22	3.06	9.56	0.06	2815		288			96.93	96.93	san				1.89	11.69	86.42
RE.PR11.F21.M2	59.48	0.37	17.89	3.59	0.11	0.76	2.60	3.43	9.15	0.08	3908		380			97.45	97.45	san				1.89	11.69	86.42
RE.PR11.F21.M3	58.13	0.36	17.22	3.06	0.10	0.71	2.43	3.16	9.05	0.11	3492		376			94.33	94.33	san				1.89	11.69	86.42
RE.PR11.F22.M1	59.93	0.43	17.85	2.71	0.17	0.41	1.94	4.44	8.39	0.06	5695	1367	587	1.41	68	98.97	96.33	san				2.48	20.51	77.01
RE.PR11.F22.M2	60.56	0.47	17.22	3.24	0.22	0.37	2.40	5.02	7.13	0.03	6609		316			96.66	96.66	san				2.48	20.51	77.01
RE.PR11.F4.M1	59.73	0.29	17.47	2.99	0.12	0.58	2.24	2.87	9.59	0.03	2748	1928	474	1.18		97.85	95.91	san				1.85	12.24	85.91
RE.PR11.F5.M1	59.71	0.43	17.54	2.79	0.14	0.40	2.04	4.48	8.03	0.08	4582	1711	455	0.92		97.58	95.63	san				2.52	20.18	77.3
RE.S08.D11.M2	58.46	0.46	18.33	3.50	0.15	0.39	2.12	4.39	8.54	0.14	3812	2836	196	1.65		98.01	96.49	cpx	47.29	38.53	14.18			
RE.S08.D13.M1	58.77	0.44	18.97	3.46	0.13	0.63	2.16	4.08	8.81	0.16	5714	2560	343	1.32	56	100.19	97.60	cpx	47.10	40.09	12.81			
RE.S08.D13.M4	57.89	0.40	18.08	3.04	0.10	0.58	2.02	3.83	8.44	0.13	6592		160			94.51	94.51	cpx	47.10	40.09	12.81			
RE.S08.D13.M5	58.49	0.50	18.81	3.21	0.08	0.66	2.22	4.15	8.67	0.13	5736		421			96.93	96.93	cpx	47.10	40.09	12.81			
RE.S08.D2.M1	58.19	0.46	16.81	4.32	0.20	0.49	2.20	4.31	7.59	0.09	7580		641			94.66	94.66	cpx	47.60	35.65	16.76			
RE.S08.D2.M2_av	59.27	0.50	17.76	3.65	0.16	0.47	2.34	4.34	7.92	0.02	6612	1735	318	1.83		98.75	96.43	cpx	47.60	35.65	16.76			
RE.S08.D2.M3	57.84	0.48	17.42	3.35	0.12	0.43	2.11	4.76	8.10	0.08	7931		324			94.68	94.68	cpx	47.60	35.65	16.76			
RE.S08.D2.M4	58.09	0.45	17.83	3.39	0.12	0.45	2.33	4.22	7.83	0.06	7710		72			94.78	94.78	cpx	47.60	35.65	16.76			
RE.S08.D4.M1	54.14	0.56	18.62	6.15	0.09	1.32	4.03	3.00	7.85	0.37	4716	2277	579	1.16	258	99.07	96.14	cpx	47.07	40.25	12.68			
RE.S08.D4.M2	52.33	0.56	18.02	6.20	0.15	1.60	4.05	3.19	7.82	0.49	5418		581			94.41	94.41	cpx	47.07	40.25	12.68			
RE.S08.D4.M3	53.09	0.48	18.81	6.15	0.13	1.65	4.09	3.16	7.71	0.62	5303		605			95.89	95.89	cpx	47.07	40.25	12.68			
RE.S08.D4.M4	54.07	0.50	19.33	5.70	0.09	1.46	4.22	3.98	6.95	0.51	4528		561			96.80	96.80	cpx	47.06	42.97	9.97			
RES08.D7.M1	58.92	0.58	18.54	3.46	0.07	0.58	2.15	4.15	8.36	0.08	5208	2051	458	1.50	104	98.92	96.88	cpx	47.77	37.60	14.63			
RES08.D7.M2	58.84	0.43	18.91	3.11	0.08	0.52	1.65	4.12	8.80	0.15	7025		637			96.61	96.61	cpx	47.77	37.60	14.63			
RESO8.D7.M3	57.78	0.47	17.32	3.16	0.12	0.41	1.78	3.59	8.85	0.14	5874		320			93.62	93.62	cpx	47.77	37.60	14.63			
RE.S08F1.M1	58.77	0.43	17.81	3.31	0.15	0.62	2.34	4.17	8.45	0.14	5883		252			96.12	96.12	san				3.99	19.05	76.96
RE.S08F1.M2	58.58	0.46	17.36	3.35	0.10	0.60	2.25	4.06	8.19	0.09	5866		429			95.05	95.05	san				3.99	19.05	76.96
RE.S08F1.M3	59.15	0.49	18.25	3.27	0.10	0.63	2.37	4.12	8.41	0.08	5031	2794	452	1.32		99.19	96.87	san				3.99	19.05	76.96
RE.S08F1.M4	59.31	0.54	18.08	3.30	0.12	0.60	2.37	4.31	8.27	0.11	5581		216			97.01	97.01	san				3.99	19.05	76.96
RE.S08F1.M5	58.82	0.38	17.31	2.78	0.11	0.51	1.96	4.16	8.01	0.10	4577		284			94.15	94.15	san				3.99	19.05	76.96
RE.S08F10.M1	58.89	0.50	17.87	3.37	0.15	0.54	2.31	4.52	8.02	0.09	6692	1400	454	1.35	180	98.67	96.26	san				3.03	20.77	76.20
RE.S08F12.M1	60.17	0.43	17.85	2.64	0.11	0.44	2.03	4.36	8.09	0.06	5707	2808	253	1.25		98.30	96.18	cpx				2.75	17.86	79.40
RE.S08F12.M2	60.18	0.47	17.93	2.81	0.09	0.45	2.16	4.31	8.00	0.13	6078		160			96.53	96.53	san				2.75	17.86	79.40
RE.S08F16.M1	58.88	0.58	18.31	3.58	0.12	0.62	2.30	4.47	8.12	0.05	6463	2353	468	1.19		99.31	97.02	san				2.92	20.70	76.37
RE.S08F6.M1	58.57	0.46	18.08	3.65	0.14	0.62	2.35	4.65	7.78	0.12	5638	2529	324	1.28		98.49	96.42	san				3.50	18.83	77.68
RE.S08F6.M2	58.61	0.44	18.01	3.45	0.09	0.56	2.23	4.57	7.76	0.09	7808		469			95.80	95.80	san				2.69	21.15	76.16
RE.S08F6.M3	58.34	0.41	17.85	3.41	0.14	0.62	2.27	4.76	7.92	0.09	7873		405			95.80	95.80	san				2.83	19.95	77.22
RE.S08F8.M1	59.15	0.50	17.95	3.32	0.11	0.51	2.08	4.90	7.43	0.07	5834	1821	347	1.95		98.25	96.03	san				2.38	20.48	77.14
RE.SC2.A10.M1	50.59	1.48	18.80	6.98	0.13	3.65	6.63	3.25	3.75	0.45						95.72	95.72	cpx	47.71	45.33	6.96			
RE.SC2.A10.M2	49.36	1.32	17.57	6.42	0.09	5.10	8.38	3.10	3.70	0.50	2520	933	1208	0.97	122	98.24	95.55	cpx	47.71	45.33	6.96			
RE.SC2.D11.M1	47.76	1.37	16.72	7.64	0.14	5.32	10.41	2.71	3.39	0.49						95.95	95.95	cpx	47.57	45.18	7.26			
RE.SC2.D11.M3	47.22	1.51	17.10	8.28	0.12	5.19	10.76	3.13	2.43	0.40						96.14	96.14	cpx	47.57	45.18	7.26			
RE.SC2F2.M1av	61.07	0.59	17.61	2.28	0.15	0.39	1.14	5.79	6.53	0.05	1188		239			95.56	95.56	san				4.12	41.80	54.08
RE.SC2F2.M3	61.57	0.45	17.65	2.20	0.16	0.39	1.14	5.84	6.77	0.08	2701		569			96.25	96.25	san				4.12	41.80	54.08
RE.SC2F4.M1	59.63	0.36	17.82	2.94	0.06	0.50	2.23	3.00	9.50	0.08	2085	904	299		84	97.48	96.12	san				2.14	11.75	86.11

Table 2 (*continued*)

Normal MI

Sample	SiO₂ (wt%)	TiO₂	Al₂O₃	FeO_tot	MnO	MgO	CaO	Na₂O	K₂O	P₂O₅	Cl (ppm)	F	S	H₂O (wt%)	CO₂ (ppm)	total (wt%)	major elements only total	host phase	wo (mol%)	en	fs	An	Ab	Or
RE.SC2.F4.M2	60.45	0.38	18.39	3.03	0.07	0.55	2.18	3.03	9.66	0.09						97.84	97.84	san				2.14	11.75	86.11
RE.SC2.F5.M1	57.62	0.44	17.41	3.09	0.22	0.26	1.39	5.43	7.39	0.05						93.31	93.31	san				4.70	36.21	59.09
RE.SC2.F5.M2	59.08	0.42	17.65	2.99	0.20	0.31	1.50	6.99	5.69	0.08	5466	3860	199	1.57		97.46	94.91	san				4.70	36.21	59.09
RE.SC2.F7.M1	57.06	0.41	17.34	3.11	0.09	0.70	2.44	2.75	8.89	0.13	3123	1547	605	2.54	120	96.10	92.93	san				3.07	11.40	85.53
RE.SE17.AD9.m5	58.89	0.34	18.18	2.82	0.05	0.86	3.06	3.93	8.94	0.13	2994		228			97.19	97.19	cpx	47.25	39.33	13.42			
RE.SE17.AD9.m6	59.03	0.33	18.41	2.47	0.10	0.60	2.56	3.62	9.17	0.13	2799		212			96.41	96.41	cpx	47.25	39.33	13.42			
RE.SE17.AD9.m7	58.16	0.42	18.58	2.82	0.11	0.59	2.95	3.95	8.87	0.14	4308		469			96.60	96.60	cpx	47.25	39.33	13.42			
RE.SE17.D13.M1	51.34	0.51	15.03	4.48	0.07	5.86	9.90	2.93	6.54	0.51	4218		1918			97.17	97.17	cpx	48.56	38.61	12.83			
RE.SE17.F4.M1	59.30	0.91	17.99	3.06	0.05	0.47	2.02	2.86	10.31	0.15	1705	81	38	0.02	19	97.17	97.12	san				4.13	17.57	78.29
RE.SE17.F4.M2	60.76	0.17	18.05	1.68	0.09	0.21	1.50	3.37	11.17	0.01	1934		64			97.01	97.01	san				4.13	17.57	78.29
RE.SE17.f6.m1	59.33	0.37	17.28	2.85	0.12	0.45	1.98	3.06	9.61	0.18	3623		176	0.05		95.23	95.23	san				3.09	17.41	79.50
RE.SE17.f6.m2	60.05	0.34	17.95	3.01	0.12	0.54	2.31	3.13	10.05	0.21	4161		196			97.78	97.71	san				3.09	17.41	79.50
REBA1.F2.M1	58.95	0.38	17.44	3.28	0.14	0.72	2.40	2.36	9.53	0.09	2472		336			95.29	95.29	plg				80.68	16.42	2.90
REBA1.F3.M1	57.75	0.31	17.57	3.66	0.07	0.79	2.72	3.63	7.87	0.16	3508		509			94.54	94.54	plg				81.08	15.90	3.02
REBA1.F34.M2	58.27	0.40	17.62	3.59	0.11	0.79	2.54	2.72	9.47	0.12	3394		569			95.62	95.62	plg				81.08	15.90	3.02
REBA1.F7.M1	59.57	0.47	17.83	2.70	0.12	0.39	1.91	4.44	8.02	0.07	6919		501			95.51	95.51	san				3.69	20.74	75.57
REMS12.C4.M1	57.73	0.43	17.69	3.89	0.14	0.74	2.53	4.02	8.65	0.12	6152		284			95.94	95.94	cpx	46.81	39.31	13.88			
REMS12.C4.M2	57.90	0.55	17.67	4.07	0.08	0.69	2.56	3.69	8.67	0.13	6495		681			96.01	96.01	cpx	45.66	40.47	13.88			
REMS12.C4.M3	58.28	0.55	18.08	4.09	0.15	0.73	2.45	2.65	8.25	0.13	6462		521			95.37	95.37	cpx	45.66	40.47	13.88			
REMS12.C5.M1	57.97	0.57	18.41	4.30	0.11	0.79	2.94	4.40	8.44	0.20	6013		429			98.13	98.13	cpx	47.22	38.93	13.85			
REMS12.C5.M2	57.15	0.40	18.06	3.90	0.16	0.79	2.86	4.07	8.42	0.17	5450		561			95.99	95.99	cpx	47.22	38.93	13.85			
REMS12.C6.M1	60.89	0.59	16.53	4.18	0.18	0.56	2.62	4.77	7.25	0.07	7800		124			97.63	97.63	cpx	46.19	37.64	16.18			
REMS12.C7.M1	58.79	0.44	17.47	3.80	0.14	0.75	2.66	4.03	8.34	0.11	5189		501			96.53	96.53	cpx						
REMS12.C7.M2	58.01	0.47	17.81	3.81	0.15	0.76	2.51	4.06	8.83	0.10	6323		505			96.51	96.51	cpx						
REMS12.C7.M3	59.03	0.42	17.83	3.85	0.15	0.75	2.56	4.04	8.49	0.07	6429		328			97.19	97.19	cpx						

Anomalous MI

Sample	SiO₂ (wt%)	TiO₂	Al₂O₃	FeO_tot	MnO	MgO	CaO	Na₂O	K₂O	P₂O₅	Cl (ppm)	F	S	H₂O (wt%)	CO₂ (ppm)	total (wt%)	major elements only total	host phase	wo (mol%)	en	fs	An	Ab	Or
RE.PR11.A13.M2	50.82	0.35	21.41	6.24	0.15	1.27	6.56	3.89	6.17	0.77	1984	958	1092	1.10		99.21	97.63	cpx	45.83	47.71	6.46			
RE.SC2.D11.M2	49.36	1.32	17.57	6.42	0.22	5.10	8.38	3.10	3.70	0.50				1.95		98.24	95.55	cpx	47.57	45.18	7.26			
RE.SC2.A10.M3	47.62	0.95	22.31	5.23	0.10	4.00	6.82	3.08	3.82	0.47						94.86	94.41	cpx	47.71	45.33	6.96			
RE.SE17.F7.M1av	58.76	0.37	18.16	2.43	0.10	0.36	1.93	3.57	10.11	0.05	4058	1494	252	0.12	4	96.53	95.84	san				2.44	16.84	80.72
RE.SE17.D13.M2	48.37	1.03	12.48	5.64	0.10	9.21	12.83	2.07	4.30	0.63	3908		2884			96.65	96.65	cpx	48.02	44.91	7.08			
RE.SE17.AD9.m2	58.23	0.46	18.31	3.43	0.13	0.68	3.07	3.67	8.93	0.20	5412	2427	860	0.42		98.53	97.11	cpx	46.62	43.07	10.31			
RE.SE17.AD12.m2av	47.30	1.33	12.50	6.06	0.11	9.54	14.30	1.90	3.45	1.44	913	1232	429	0.02	13	98.26	97.91	cpx	47.89	46.27	5.84			
RE.SE17.AD12.m1av	50.29	0.77	13.02	4.00	0.05	8.33	11.89	2.24	6.15	0.68	3582	3532	1699	0.20	64	98.73	97.40	cpx	47.89	46.27	5.84			
REBA1.P6.M3	63.03	0.11	20.20	0.13	0.01	1.30	0.96	3.53	5.13	0.00	220		140			94.40	94.40	plg				74.72	23.11	2.17
REBA1.P6.M2	58.62	0.13	19.48	0.16	0.00	1.19	1.05	4.07	4.98	0.01	171		bdl			89.69	89.69	plg				74.72	23.11	2.17
REBA1.P6.M1	59.57	0.47	17.83	2.70	0.12	0.39	1.91	4.44	8.02	0.07	473		bdl			95.51	95.51							
																Average	95.93							

Notes: MI showing only Cl and S as volatile concentrations were measured using EMP, all other MI were measured using SIMS; MI totals showed in green include H₂O contents.
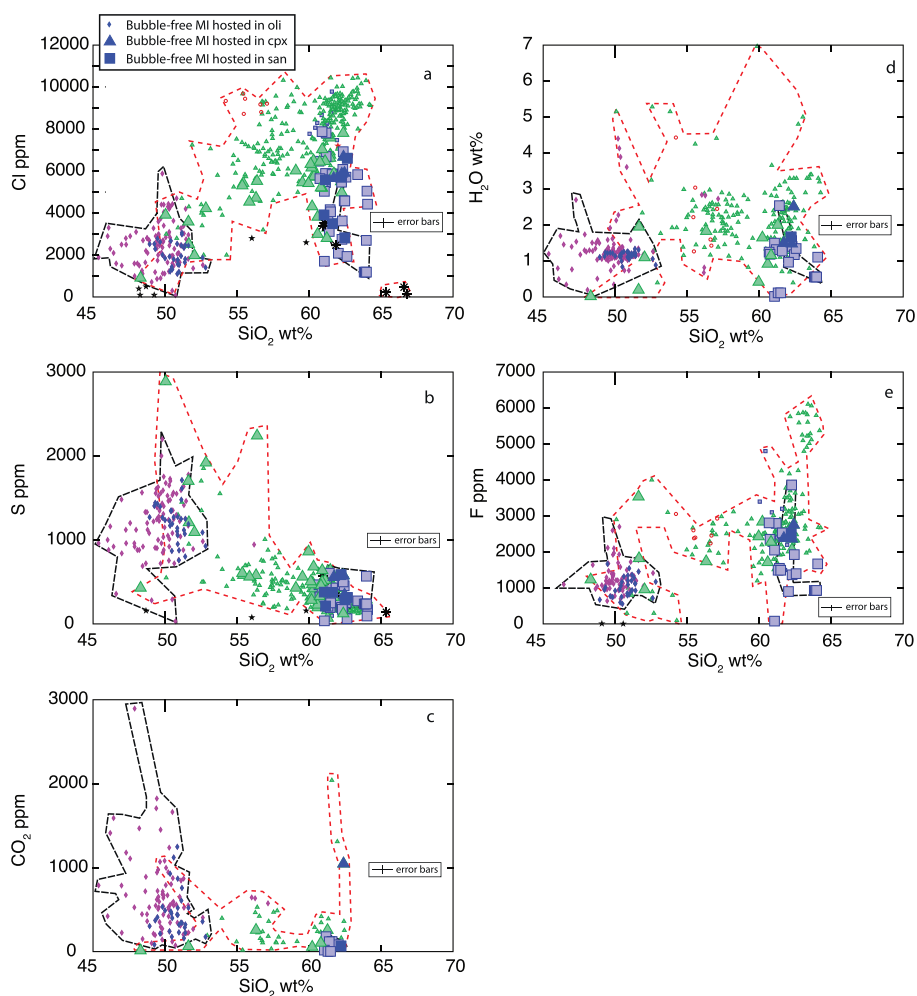
Fig. 3. Volatile concentrations of MI versus SiO_2 concentration for (a) Cl, (b) S, (c) CO_2, (d) H_2O and (e) F. Symbols and fields are the same as in Fig. 2, with the addition that *bubble-free MI* are differentiated using dark-blue symbols. Note that bulk rock data show only low contents of Cl, S and F, whereas bulk rock data for H_2O are absent. Estimated uncertainties for the data from the present study are shown as error bars in each panel. (For interpretation of the references to colour in this figure legend, the reader is referred to the web version of this article.)

MI data reported in the literature for other magmatic systems. For instance, TiO_2 contents of MI from this study show weak correlations with crystallization indicators relative to bulk rock data from the literature (Fig. 2d). For the least evolved MI compositions, TiO_2 concentrations span a wide range, while for more evolved compositions TiO_2 concentrations are more restricted.

For the MI studied here, FeO_{tot} behaves in a manner similar to TiO_2 (Fig. 2e). In particular, less evolved MI show more scatter relative to the more evolved MI. Some MI from the less evolved group (SiO_2 concentration ranging from ~47 to ~54 wt%) are FeO-depleted relative to the bulk rocks. The Fe-poor MI are all hosted in clinopyroxene from the Fossa Lupara sample. Some MI data from the literature for the Minopoli1 and Fondo Riccio eruptions (Cannatelli et al., 2007) and for the Solchiaro eruption (Mormone et al., 2011) show the same behavior, and most of the MI are hosted in clinopyroxene (three MI are hosted in olivine). In addition, a group of MI hosted in olivine and clinopyroxene from the Minopoli2 and Fondo Riccio eruptions (Mangiacapra et al., 2008) show extremely low FeO_{tot} contents at intermediate SiO_2 contents. Also, some MI hosted in clinopyroxene from the Astroni1 eruption (Stock et al., 2016) show a depletion in FeO_{tot} relative to the bulk rock trend. The depletion of FeO may reflect Fe loss from the MI to the Fe—Mg host via diffusion, as has been proposed and documented for other volcanic systems (Danyushevsky et al., 2000). It is important to note that most of the Fe-poor and less evolved MI from CF were heated

experimentally. Some of the Fe-poor MI also show slight depletion in Al_2O_3, slightly higher CaO contents, lower Na_2O contents, and slightly higher K_2O (Fig. 2).

Several evolved MI from this study show a slight depletion of Na_2O relative to the bulk rock geochemical trends, with the exception of MI from the Solfatara and Astroni samples. Some of the bulk rock compositions show the same Na-depletion, and several MI compositions reported in the literature show the same behavior. Na_2O-poor MI are not preferentially hosted in sanidine or clinopyroxene phenocrysts, and they include both heated and naturally quenched MI. Na_2O-poor MI can indicate that Na has been lost from the MI by diffusion, and to test this hypothesis we calculated totals considering both EMP and SIMS concentrations. Some of the Na-poor MI show ~100 wt% totals (Table 2), suggesting that Na loss is minimal. Also, there is no correlation between Na_2O and H_2O concentrations. In addition, the group of MI showing depletion of Na_2O shows a slight enrichment in K_2O. Potassium should not increase as a result of Na loss by diffusion (Morgan and London, 2005). It is also important to note that Na-loss should not be significant at the conditions used to analyze major element concentrations (Hayward, 2012). The least evolved MI from this study, as well as those from the literature, show a wide range of K_2O concentrations. For instance, for MI with SiO_2 of ~50 wt%, K_2O varies by a factor of 6 (from ~1 to ~6 wt%) (Fig. 2b).

Among major and minor elements, P_2O_5 shows the poorest

correlation with SiO_2 content. P_2O_5 concentrations of mafic and intermediate composition MI both from this study and from the literature show considerable scatter (from ~45 to ~57 wt% SiO_2, see Fig. 2 f), while evolved MI (from ~57 to ~66 wt% SiO_2) show good correlations between P_2O_5 contents and crystallization indicators.

A group of MI hosted in plagioclase from the Bacoli eruption does not overlap with the general trends defined by MI from the literature, or with bulk rock data for most of the major elements. The compositions of plagioclase-hosted MI are Qz normative, an observation that is rare for bulk rocks of CF and IP. These plagioclase-hosted MI show Na_2O and K_2O concentrations consistent with CF and IP bulk rock differentiation trends, while Al_2O_3 and SiO_2 concentrations are slightly higher than the bulk rock differentiation trends (Fig. 2). Concentrations of TiO_2, CaO, FeO, and P_2O_5 are lower than those shown by the bulk rock differentiation trends. The compositions of the MI hosted in plagioclase are not representative of CF and IP magmatism, suggesting that plagioclase selected for the study represent xenocrysts or that they formed under disequilibrium conditions.

Finally, we note that some of the individual bulk rock compositions project off the main bulk-rock trend (Fig. 2), and these tend to lie along mixing lines that point toward clinopyroxene or feldspar compositions. This suggests that some of the bulk rock compositions represent mixtures of melt plus entrained crystals. These "anomalous" bulk rock compositions represent a small fraction of the complete dataset.

5.4. Volatiles

Among all volatiles analyzed, Cl shows the best correlation with SiO_2 concentration, especially for less-evolved melts, while S shows a weak correlation, and H_2O, CO_2, and F show no correlation with SiO_2 (Fig. 3). Considering MI hosted in all phases, we observed two important features: (1) volatile concentrations of the MI studied here overlap with volatile concentrations of MI from CF and IP reported in the literature and (2) volatile concentrations of MI from this study are higher relative to CF and IP bulk rocks reported in the literature. This latter observation highlights the limitations of using bulk rocks to determine volatile compositions of magmas, because these samples have partially or totally degassed during ascent and eruption onto the surface. Conversely, MI are more likely to retain the original pre-eruptive volatile content during ascent and eruption.

Chlorine concentrations range from 913 to 7931 ppm. Chlorine behaves incompatibly through most of the magmatic differentiation showing a good correlation with $SiO_2 < 60$ wt% (0.85 r^2), but for $SiO_2 > 60$ wt% Cl shows a sub-vertical trend from 7710 to 1188 ppm (Fig. 3a). This vertical trend is observed for all MI hosted in sanidine.

Sulfur concentrations range from below detection limit (bdl) to 2884 ppm. Sulfur generally decreases from less evolved MI to more evolved MI. The S contents of MI are more scattered for less evolved MI, while S is more clustered for more evolved compositions (Fig. 3b).

Concentrations of H_2O in the MI studied here range from bdl to 2.54 wt%. In contrast to Cl and S, H_2O shows poor correlations with SiO_2, but for MI with > 60 wt% SiO_2 a sub-vertical distribution is observed (Fig. 3d). It is important to recognize that the H_2O-SiO_2 trend for MI with < 60 SiO_2 is defined by only five MI.

Fluorine concentrations range from 81 to 3860 ppm. Fluorine concentrations of MI show a behavior similar to Cl, but the correlation is weaker. For MI > 60 wt% SiO_2 the distribution is sub-vertical as observed for Cl and H_2O. Since there are only five MI showing $SiO_2 < 60$ wt%, the apparent vertical trend may reflect the small sample size (Fig. 3e).

Carbon dioxide concentrations range from below detection limit to 258 ppm with one MI from the NYT sample showing 1046 ppm (Fig. 3c). Carbon dioxide does not correlate with SiO_2 even when a single eruption is considered (Fig. 3c), and H_2O-CO_2 systematics do not define a trend (Fig. 4a). In contrast, MI from individual eruptions are considered, the NYT MI show a positive trend (Fig. 4b). The correlation
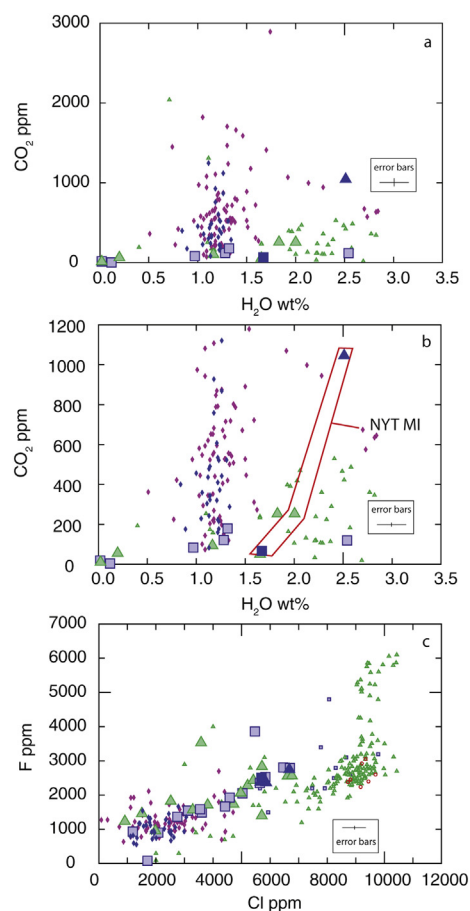
Fig. 4. Volatile concentrations of MI. a) H_2O versus CO_2 showing full range of reported CO_2 concentrations; b) H_2O versus CO_2 showing MI with up to 1200 ppm CO_2 (red field encircles MI from the Neapolitan Yellow Tuff); c) F versus Cl. Note the positive correlation suggesting that F and Cl have similar behavior during the differentiation of magmas associated with CF and IP. Symbols and fields are the same as in Figs. 2 and 3. Estimated uncertainties for the data from the present study are shown as error bars in each panel. (For interpretation of the references to colour in this figure legend, the reader is referred to the web version of this article.)

shown by NYT MI should be viewed with caution because only three analyses are available.

In general, volatile abundances of MI do not correlate with each other, with the exception of Cl vs F (Fig. 4c) which shows a strong positive correlation. This suggests that Cl and F are retained in the melt during the initial and intermediate stages of differentiation (trachybasalt-shoshonite-latite). During the last stages of crystallization, Cl likely partitions strongly into the fluid phase while F is retained in the melt.

5.5. Host mineral compositions

MI from this study are hosted in clinopyroxene (cpx), sanidine, and plagioclase. The ferrosilite component of cpx hosting MI ranges from 6 to 18 mol%, the wollastonite component from 46 to 49 mol%, and the enstatite component ranges from 34 to 48 mol% (Suppl. Fig. 2c). The MI compositions and host phase compositions are both consistent with trapping of a melt that was in equilibrium with cpx during crystallization. For example, the SiO_2 concentration of MI correlates with the ferrosilite component. Note that MI data show some significant scatter, and we will discuss the reasons for this in the discussion section. MI and clinopyroxene host compositions are consistent with data reported in the literature.

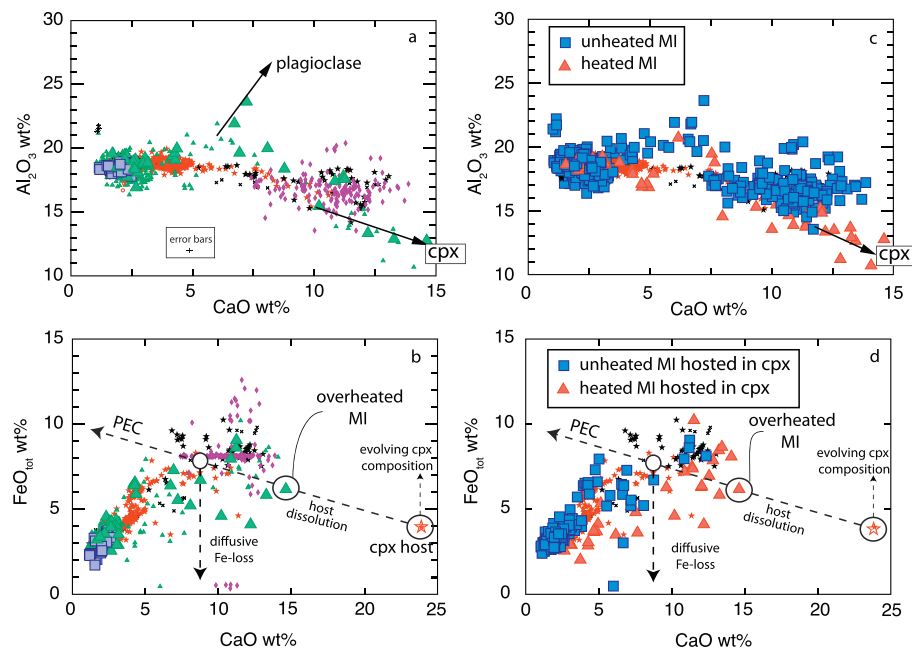The sanidines containing MI analyzed in this study possess 54 to

Fig. 5. Major element compositions of MI from this study and from the literature compared to bulk rock compositions. a) CaO vs. Al_2O_3 of MI discriminated by host phase (symbols the same as in Fig. 2); arrows point to plagioclase and clinopyroxene compositions of PVD. Note some less evolved MI showing high CaO and low Al_2O_3 contents. MI plotting off of the main bulk rock trend are hosted in clinopyroxene. b) CaO vs. FeO_{tot} of MI discriminated based on host phase (symbols same as in Fig. 2); note that several MI hosted in clinopyroxene and olivine plot outside the trend defined by the bulk rock data. The red star represents the composition of clinopyroxene host associated with the overheated MI (RESE17-AD12-M2, from this study). The white filled circle represents the hypothetical original trapped composition. Dashed lines represent trends associated with host dissolution, PEC, or Fe-loss by diffusion. c) CaO vs. Al_2O_3 of MI discriminated as either naturally glassy (unheated) MI or MI reheated in the lab. It is important to note that the Ca-rich and Al-poor inclusions were all reheated in the lab. d) CaO vs. FeO_{tot} of MI hosted in clinopyroxene, discriminated as either naturally glassy (unheated) MI or MI reheated in the lab. It is important to note that heated MI are generally distributed to the right (higher CaO) side of the bulk rock trend. (For interpretation of the references to colour in this figure legend, the reader is referred to the web version of this article.)

86 mol% orthoclase component, with most in the range 76–86 mol% (Suppl. Fig. 2a and b). The Or-poor sanidines are restricted to the Solchiaro sample and show up to 42 mol% albite component. No correlation is observed between host composition and SiO_2 concentration of MI (Suppl. Fig. 2a). One possible explanation is that sanidine began to crystallize over a restricted interval of SiO_2 concentrations (see discussion section for more details). However, a good correlation is observed if the orthoclase component of the host is plotted versus SiO_2/CaO ratio of the MI (Suppl. Fig. 2b). The SiO_2/CaO ratio is likely a better crystallization indicator at this differentiation stage, and, also, this ratio is not affected by PEC or host dissolution (see the discussion section for more details). The orthoclase component decreases and the albite component increases as crystallization progresses. This behavior was reported and documented by Melluso et al. (2012) who showed that the NaO content of the alkali feldspar increases in the more evolved bulk rocks.

Only six MI from this study and from the literature combined are hosted in plagioclase. The anorthite component ranges from 75 to 81 mol%, and the anorthite component of the host correlates with the SiO_2 concentration of the MI. This observation, based on only six MI, should be taken with caution.

5.6. Post entrapment crystallization or dissolution

In this study we did not attempt to correct for changes in MI composition associated with post entrapment crystallization (PEC) owing to the lack of a reliable model to implement the correction. We note that Kress and Ghiorso (2004) report that an algorithm incorporated into the MELTS platform could be used to estimate PEC based on the composition of the MI and the host for various phenocrysts, including pyroxene and feldspar. We attempted to apply this method to correct the MI of this study but the results indicated that ~90% PEC had to occur for many MI. This value is not realistic and is not supported by petrographic examination of the MI. As such, we consider bubble-free MI having compositions that overlap with bulk rock compositions to have experienced only minimal PEC, and have assumed that the compositions of the MI reasonably approximate the original melt composition.

6. Discussion

Our interpretation of geochemical trends in MI from CF and IP is based on new data from this study as well as published data for CF and IP. First, we focus on major element concentrations of MI that do not follow the general trends defined by bulk rock compositions. We test if the MI compositions are representative of the silicate melt in equilibrium with the host mineral, based on major element compositions. We discuss the significance of anomalous MI, and we exclude the non-representative anomalous MI from the interpretation of volatile evolution at CF and IP. Second, we focus on volatile and major element concentrations of normal MI that have trapped and preserved a representative sample of the melt at the time of trapping. We discuss the significance of volatile concentrations of all MI, and we select only the bubble-free MI to investigate crystallization trends using the rhyolite-MELTS code (Ghiorso and Gualda, 2015).

6.1. Significance of anomalous MI

Anomalous melt inclusions are those whose compositions cannot be reasonably inferred to represent compositions of melts along a fractionation trend. Below we discuss the anomalous MI that were identified and possible processes that may have produced the anomalous compositions.

6.1.1. Al_2O_3 and P_2O_5 anomalies of MI

Several processes can lead to anomalous Al_2O_3 and P_2O_5 concentrations in MI. These anomalous compositions can represent the trapping of a boundary layer associated with rapid crystal growth rates (e.g., Baker, 2008), or could represent trapping of melt produced as a result of dissolution-reaction-mixing (DRM) processes in the mush zone (Danyushevsky et al., 2004). Alternatively, these anomalies can be artifacts generated as a result of overheating during laboratory heating experiments. In this section, we discuss which processes are likely responsible for the anomalous MI observed at CF and IP.

As reported above, several MI are enriched in Al_2O_3 relative to bulk rocks in differentiation plots. Including MI from the literature, we observed that Al_2O_3 is one of the major components that shows large deviations from bulk rock geochemical trends. MI hosted in clinopyroxene show the largest variations for Al_2O_3 (Fig. 5a). At intermediate

CaO concentrations (between 5 and 8 wt%), some MI hosted in clinopyroxene show Al_2O_3 contents that are elevated relative to bulk rocks. At high CaO concentrations, other MI hosted in clinopyroxene shows anomalously low Al_2O_3 concentrations relative to the bulk rocks. It is worth noting that a few MI hosted in olivine show a slight enrichment in Al_2O_3 content. Experimental studies suggest that host-incompatible element concentrations of MI could be affected by boundary layer process. In particular, Faure and Schiano (2005) reported that MI trapped in fast growing olivine show a significant enrichment in Al concentration. However, boundary layer effects alone cannot explain the CaO vs. Al_2O_3 deviations of MI from the bulk rock trends. Interestingly, the Al_2O_3-poor MI were all reheated in the laboratory, while the most of the Al_2O_3-rich MI are naturally quenched (Fig. 5b). These Al_2O_3-rich MI show low TiO_2, FeO_{tot}, and MgO, and this observation is consistent with high degrees of PEC or with a plagioclase component added to the "normal" CF melt composition. However, it is important to note that most of the Al_2O_3-rich MI also show elevated P_2O_5 and some show high Cl concentrations, consistent either with trapping of apatite along with the melt or that some MI hosted in clinopyroxene trapped a boundary layer melt that was enriched in P (Baker, 2008).

For most of the Al-rich MI, the P_2O_5 enrichment cannot be attributed to PEC. If we consider the Al-rich MI showing the highest P_2O_5 concentration [1.38 wt%, "FRC2-P7-M1" from Cannatelli et al. (2007), see database Appendix Table D] and the BR showing the highest P_2O_5 concentration (0.6 wt%, "s 97110PNA-S"), ~57% PEC would be required to bring the MI composition into coincidence with the BR trend. With this amount of PEC other phases in addition to the host would also be crystallizing in the MI. Also, the Al-rich MI under consideration was reheated in the lab, and was quenched when the MI homogenized, indicating only minor PEC if the quenching occurred from a temperature that was lower than the trapping temperature. Also, at 57% PEC the Al_2O_3 concentration should have been ~11 wt%, a value that is much lower than the BR with similar extent of differentiation. To explain the P_2O_5 enrichment of FRC2-P7-M1 only requires ~2% apatite component, while the enrichment of Al_2O_3 would require a ~23% plagioclase component.

It is generally assumed that boundary layer processes would affect compositions of smaller inclusions to a greater extent compared to larger inclusions being trapped at the same crystal-melt interface. Esposito et al. (2011) found no correlation between the MI size and the P_2O_5 and K_2O concentration, suggesting that boundary layer processes alone cannot explain the Al_2O_3–P_2O_5 MI trends. Furthermore, an inverse correlation between the size of MI and the concentration of slow diffusing elements should be expected only if there is evidence that all the MI being considered trapped the same melt. In other words, we cannot compare data for a group of MI if there is no evidence that each MI was originally trapped from the same bulk melt. This fact underscores the importance of studying MIA (Bodnar and Student, 2006) to test for correlations (if any) between MI composition and size. With the assumption that all MI comprising the MIA trapped the same melt, the correlation between size and concentration of slow diffusing elements can be used to test whether boundary layer processes significantly affected the composition of those MI, and corrections to determine the original trapped melt composition can be proposed.

In this study, all MI hosted in sanidine show similar compositions and show no correlation between size of the MI and the K_2O concentration (Suppl. Fig. 4), suggesting that boundary layer processes did not affect the composition of sanidine-hosted MI. The selective enrichment of major and trace elements can be interpreted as the result of dissolution-reaction-mixing (DRM) in a mush zone at the interface between a magma body and wall rock (Danyushevsky et al., 2004; Esposito et al., 2011). Thus, the enrichment of Al_2O_3 can be explained by DRM between plagioclase and melts at various stages of evolution. Combined enrichment of Al_2O_3 and P_2O_5 can represent DRM between less evolved melt and mush zone material of more evolved magmas rich in plagioclase and apatite beneath CF and IP. The DRM interpretation

implies micro-scale heterogeneity that results when a less evolved melt ascends and interacts with a preexisting mush zone. In particular, the DRM interpretation corroborates the hypothesis that basaltic and trachybasaltic magmas interacted with a mush zone consisting of cogenetic evolved latitic and trachytic-phonolitic magmas at CF and IP, as reported in other studies (D'Antonio, 2011 and references therein).

As reported above, some of the heated and less evolved MI hosted in clinopyroxene show enrichment in CaO and MgO, and depletion in Al_2O_3, TiO_2, and Na_2O. These anomalies indicate that MI have likely been over-heated in the laboratory and the resulting composition of MI shows dilution of clinopyroxene-incompatible elements and enrichment in clinopyroxene-compatible elements (Fig. 5b). We attempted to correct compositions of reheated MI hosted in clinopyroxene by adjusting the CaO and Al_2O_3 to the regression line of the bulk rock data or to the bulk rock data "cloud" in the CaO vs. Al_2O_3 plot (Suppl. Fig. 3a). This correction suggests that 30 to 33% of host dissolution would have occurred during heating. However, after this correction, FeO, K_2O and P_2O_5 still show anomalous concentrations (Suppl. Fig. 3b, c, and d). In fact, a "correction" for 30–33% host dissolution tends to drive both K_2O and P_2O_5 toward more anomalous compositions. This suggests that a simple host dissolution correction cannot be used to restore the original MI composition.

Heated and more evolved MI hosted in sanidine show higher K_2O concentrations relative to unheated and more evolved MI (Suppl. Fig. 4), similar to MI hosted in cpx. MI showing anomalous compositions for some major elements may also show volatile concentrations that are not representative of the silicate melt that was in equilibrium with the host at the time of trapping. For instance, if the anomalous composition of a MI is the result of DRM, the MI volatile budget could be modified, and the concentrations of individual volatile components could be differentially affected. If the wallrocks involved are dominantly composed of anhydrous phases, concentrations of all volatiles would be lowered by simple dilution (Danyushevsky et al., 2004; Esposito et al., 2011). Alternatively, if the wallrocks contain carbonates, as has been inferred for Vesuvius (Gilg et al., 2001) and Merapi (Deegan et al., 2010), the concentration of CO_2 in the magma could be increased by DRM processes. The eruptive products at CF lack carbonate-bearing xenoliths or skarn materials (D'Antonio, 2011). This suggests that DRM at CF should lower the volatile contents of the melts, and this is consistent with observations by Esposito et al. (2011) who reported very low S, CO_2 and Cl concentrations of some anomalous MI and compositions plot toward the origin on S–CO_2–Cl vs Zr binary diagrams. The low concentration of volatiles is expected for overheated MI. Even though the lowering of the volatile concentration caused by dissolving excess host during the heating experiment is likely insignificant, two additional issues are associated with overheated MI. If MI are heated to a temperature above the "true" trapping temperature, the total amount of time that the MI would have been exposed to "high" temperatures will be longer, compared to heating to a lower temperature at the same rate. This, in turn, translates into a greater likelihood to lose H^+ by diffusion (Bucholz et al., 2013; Mironov and Portnyagin, 2011). Hydrogen can also be lost from the MI in nature (before eruption), leading to an increase in the homogenization temperature of the MI and requiring heating to higher temperatures to achieve homogenization during re-heating experiments in the lab.

6.1.2. Fe exchange

Numerous studies have documented Fe loss from MI based on the negative correlation between FeO_{tot} of the MI and the composition (Fo mol%) of the host, as well as the lower FeO_{tot} in the MI relative to bulk rocks and matrix glasses of the same magmatic system at comparable degrees of differentiation (Danyushevsky et al., 2000; Danyushevsky et al., 2002b; Esposito et al., 2011; Norman et al., 2002; Sobolev and Danyushevsky, 1994; Yaxley et al., 2004). Six MI from this study show anomalously low Fe concentrations relative to the main differentiation trend defined by bulk rocks (Fig. 2 e). Three MI are hosted in

plagioclase from the Bacoli eruption, and the other three MI are hosted in clinopyroxene from the Fossa Lupara eruption, and these were heated in the laboratory to obtain a homogeneous glass. The Fe-poor MI hosted in plagioclase from Bacoli are discussed in a later section because, in addition to anomalous FeO_{tot} concentrations, these MI show anomalous compositions for most of the other major elements. The lower FeO concentrations (from 4.1 to 6.2 wt%) of Fossa Lupara MI are consistent with overheating during experiments owing to the low FeO concentrations of clinopyroxenes hosting these MI (3.7 to 4.5 wt%). These MI show elevated concentrations of CaO and MgO and a general depletion of the other major elements (Fig. 5 c and d). The effect of overheating can be observed in most of the MI hosted in clinopyroxene from this study and in MI from the literature. In fact, most of the re-heated MI (red triangles in Fig. 5 d) that fall outside of the field defined by bulk rocks and can be distinguished from the unheated MI (blue triangles in Fig. 5 d) based on their generally lower FeO_{tot} concentrations and slightly elevated CaO contents.

Roedder (1979) reported that homogenization temperatures obtained from MI might be higher than the temperature of trapping owing mainly to three factors: (1) inadequate time for re-equilibration (heating rates during experiment are too fast), (2) loss of hydrogen or water from hydrous MI (which increases the liquidus temperature relative to more H_2O-rich compositions), and (3) thermal gradients in the stage. In addition to these factors, heating beyond the original trapping temperature would be required to homogenize the MI if it did not originally trap a single homogeneous silicate melt phase (Klébesz et al., 2015; Student and Bodnar, 2004). Anomalously high homogenization temperatures can also result if the MI original trapped a silicate melt plus a mineral inclusion (see Figs. 1-15 in Bodnar and Student, 2006). Small minerals trapped along with melt might be easily misidentified as daughter crystals, although this interpretation can be ruled out by comparing the final quenched glass compositions because MI containing trapped solid(s) will be enriched in components that are major constituents of the trapped mineral phase(s) (e.g., P_2O_5 enrichment if the co-trapped mineral inclusion is apatite). Finally, homogenization temperatures in excess of trapping temperatures will result during re-heating if an MI has been affected by leakage after trapping (see Figs. 1-3, D and E in Bodnar and Student, 2006). This last possibility can often be ruled out with careful petrographic analysis of the studied MI. Even though it is important to understand which factors could have affected the MI analyzed here to produce elevated homogenization temperatures, the overheating observation highlights the importance of performing heating runs through kinetic experiments if the correct (or approximate) temperature of trapping is required (Danyushevsky et al., 2002a). An additional consideration is that heating stage experiments are performed at atmospheric pressure. Because the phenocryst host precipitated at pressures higher than ambient (1 atm) pressure, the pressure in the MI at ambient laboratory pressure would necessarily be lower than that at trapping owing to the lower confining pressure, thus requiring heating to temperatures higher than the formation temperature to produce a single homogeneous melt phase.

In addition to overheating, post-entrapment loss of FeO from the MI could have contributed to the observed depletion in FeO_{tot}. In particular, a few MI, which were not heated in the laboratory, show low FeO_{tot} concentrations relative to the differentiation trend defined by bulk rocks, suggesting diffusive Fe loss. MI data from the literature also suggest that diffusive Fe loss has affected some MI from CF and IP. Esposito et al. (2011) studied samples representative of the Solchiaro eruption and reported a negative correlation between FeO_{tot} concentrations of MI and the Fo content of the olivine host. For this reason, Esposito et al. (2011) corrected MI compositions for diffusive Fe loss, and here we use the corrected compositions. Similarly, Mangiacapra et al. (2008) studied representative samples of Fondo Riccio and Minopoli2 eruptions and reported a group of MI showing $FeO_{tot} < 1$ wt%, which suggests some MI were affected by Fe loss. It is important to note that the Fe-poor MI reported by Mangiacapra et al. (2008) do not show

anomalous concentrations for the other major elements. In addition, MI data from the literature show a wide range of FeO_{tot} concentrations for $SiO_2 < 55$ wt%, and more evolved MI show FeO_{tot} concentrations that are consistent with the bulk rock FeO_{tot} versus SiO_2 trend, indicating that more evolved MI are less affected by Fe loss/gain. Because MI examined here show evidence that the original MI composition has been modified either by diffusive Fe loss or overheating, we question whether volatile contents obtained from the MI are representative of CF and IP pre-eruptive melts. The three overheated MI from the Fossa Lupara eruption studied here show the lowest volatile contents among all the MI considered (including the MI data from the literature), supporting the interpretation that Fe-poor MI and MI that were overheated in the laboratory should be avoided when studying volatile evolution in magmatic systems.

Considering data from this study and from the literature, not only do MI from CF and IP show evidence for Fe loss, but also some MI show evidence that the Fe concentration has increased. For instance, a group of MI hosted in olivine from the Solchiaro eruption (Mormone et al., 2011) shows higher FeO_{tot} concentrations relative to the trend defined by bulk rock compositions (Fig. 5 b). These MI were not reheated in the laboratory. It is important to note that the Fe-rich MI reported by Mormone et al. (2011) are also depleted in MgO. In particular, the MgO concentrations of the MI reported by Mormone et al. (2011) range from 4.2 to 6.5 wt%, with three MI showing MgO from 0.5 to 1.7 wt% (see Table 1 by Mormone et al., 2011), values that are much lower than the respective bulk rock compositions (8.58 wt%; sample Pro7/11 by De Astis et al., 2004). Mormone et al. (2011) interpreted the MI based on EMP data, arguing that the correction for PEC was not necessary. Moreover, Fe-rich and Mg-poor MI described by Mormone et al. (2011) are difficult to reconcile based on PEC because, when olivine crystallizes on the MI wall, both the MgO and the FeO_{tot} contents of an MI should decrease because the FeO content of the olivine host that crystallizes on the wall is generally higher than the FeO_{tot} content of the initially trapped melt.

Different processes can be proposed to explain the enrichment in FeO_{tot} of a MI. First, the Fe-rich MI can result from Fe diffusing into the MI from the olivine host during re-equilibration due to natural overheating and melting of some olivine from the MI wall. In fact, as more olivine component is added to the MI, the melt must decrease its Mg# to be in equilibrium with its host (Danyushevsky and Plechov, 2011 and references therein). For the same reason, Fe gain will be accompanied by Mg loss. Second, natural overheating can cause dissolution of a pre-existing Fe-oxide. In their study of re-homogenized MI hosted in olivine from scoria and basaltic lavas, Rowe et al. (2006) reported that several MI show higher FeO_{tot} contents relative to bulk rocks and suggested two explanations (1) dissolution of olivine host and (2) dissolution of co-trapped mineral inclusions such as chromite, sulfide, and magnetite. In the case of the Fe-rich MI from CF and IP, the Fe gain can be explained by natural overheating of MI originally containing co-trapped chromite. This natural overheating could be due to less evolved/hotter magma mixing with the olivine-bearing magma or to olivine sinking to hotter levels of the magma reservoir. These processes are consistent with reverse zoning of olivine as reported in several studies (e.g., D'Antonio and Di Girolamo, 1994) and the presence of chromite inclusions in olivine from Solchiaro (Esposito et al., 2011). The Fe-rich MI from CF and IP show significantly lower SiO_2 compared to other MI from these locations, and the SiO_2 vs Al_2O_3 trend points toward chromite composition, supporting an interpretation that melting of a co-trapped chromite is responsible for the elevated Fe contents. It is also important to note that some of the Fe-rich MI were defined by Mormone et al. (2011) as exhibiting "high" or "low" degrees of crystallization. An enrichment of FeO_{tot} can result from measuring a heterogeneous ("high" or "low" crystallized MI) material containing Fe-oxides.

6.1.3. TiO$_2$ variability of less evolved MI

In this study, MI show TiO_2 contents spanning a wide range,

particularly for less evolved MI that vary from ~0.5 to ~1.7 wt% TiO$_2$. This behavior is consistent with the wide range in TiO$_2$ concentrations of MI reported in other studies (Cannatelli et al., 2007; Esposito et al., 2011; Mormone et al., 2011). In particular, Esposito et al. (2011) reported TiO$_2$-rich MI containing up to ~2.4 wt% TiO$_2$ and TiO$_2$-poor MI with concentrations as low as 0.4 wt%, and interpreted these anomalies to be the result of diffusion-mixing reaction in the mush zone. In contrast to MI, TiO$_2$ concentrations of less evolved bulk rocks at CF show less variation for the same degree of differentiation (Fig. 2 d). It is worth noting that TiO$_2$ and SiO$_2$ show positive trends for less evolved IP bulk rocks, while the bulk rocks of CF show a quasi-horizontal TiO$_2$ vs. SiO$_2$ trend (see Fig. 2 d). One interpretation is that this difference indicates that crystallization of Ti-magnetite started earlier in the evolution of CF magmas compared to magmas associated with IP.

6.1.4. Anomalous plagioclase-hosted MI from the Bacoli eruption

As reported in the results section, three MI hosted in plagioclase from the Bacoli eruption do not adhere to most of the differentiation trends defined by bulk rock compositions (Fig. 2 a to e). The MI are Qz-normative, which is rare for melts of CF and IP. The origin of these MI may be interpreted in three ways: (1) the melt may have been locally affected by dissolution-reaction-mixing (DRM) (Danyushevsky et al., 2004 and references therein), (2) the plagioclase containing these MI may be xenocrystic and formed in a different (temporal and/or spatial) part of the overall magmatic system, and (3) the melt in plagioclase may be representative of the magma chamber/country rock interface. It is important to note that these three MI show lower major oxide totals relative to the other MI of this study (from 89.6 to 94.4 wt%). Unfortunately, we cannot assess the origin of these anomalous MI at this time.

6.1.5. Summary of the major element anomalies observed in MI data

In summary, the comparison between MI data and whole rock data indicates that some MI show anomalous compositions that do not follow the bulk rock trend, and these compositions cannot be explained by the main differentiation trend. The anomalous MI compositions cannot be corrected by simply adding aliquots of mineral host back into the melt (PEC correction) or by subtracting the host mineral composition from the melt composition (host dissolution correction). MI showing anomalous compositions either trapped a melt that was not in equilibrium with the host (DRM or boundary layer processes), or the composition was modified by processes other than simple PEC or host dissolution after trapping. For these reasons, we conclude that anomalous MI likely record volatile contents that are not representative of the melt that was in equilibrium with the growing phenocryst host. Moreover, most of the processes invoked to produce anomalous MI can also affect the volatile concentrations of melt (glass) owing to the dependence of volatile solubility on the major element composition of melts (Papale et al., 2006; Shishkina et al., 2010). In addition, trapping of apatite inclusions within the MI as a component of DRM can affect the Cl, F, and H$_2$O concentration of the melt. We recommend that MI showing anomalous major element concentrations should not be selected for volatile analysis because the volatile concentrations of these MI are likely not representative of the magmatic system. If the major element composition of the MI is not known, one cannot know that the MI composition is anomalous, and, thus whether the volatile content of that MI is representative. Therefore, it is fundamental that each MI is analyzed to determine major element composition before it is analyzed for volatiles. Even though this study is focused on CF and IP volcanic fields, anomalous MI are reported in many other volcanic systems (Danyushevsky et al., 2004 and references therein), and these same conclusions and recommendations apply to all such anomalous MI.

In the following sections, we interpret and discuss the volatile budgets of MI from this study and from the literature. We do not consider MI showing anomalous major element compositions in this assessment. Similarly, we exclude any MI from the literature for which

major element compositions are not reported. Additionally, MI hosted in plagioclase were not included because the three MI hosted in plagioclase that we analyzed all showed anomalous compositions relative to the bulk rocks. It is important of note that our data filtering does not eliminate MI affected by PEC but only MI that could not be corrected by simply adding or subtracting the mineral host to the anomalous MI. In the following discussion we use ratios of elements that are incompatible with the host because these ratios should not be affected by PEC (e.g., Lima et al., 2003). Also, as noted above, while it is possible to apply relatively robust PEC corrections for MI hosted in olivine (Danyushevsky and Plechov, 2011), reliable models are not available to correct for PEC for MI hosted in clinopyroxene and feldspar.

6.2. Evolution of volatile concentrations of MI

Several studies reported bubble-bearing MI in samples from CF and IP, but fewer studies have identified which MI (bubble-bearing or bubble-free) correspond to a specific volatile analysis. One exception is the work of Esposito et al. (2011), who identified each MI as either bubble-bearing or bubble-free before exposing the MI at the surface of the host for analysis. Based on recent studies (e.g., Aster et al., 2016; Moore et al., 2015), it is not possible to determine if the reported volatile content of an MI represents the actual volatile content of the trapped melt or represents only a portion of the total volatile budget in the original melt if the type of MI (bubble-bearing versus bubble-free) is not reported. Thus, the following discussion relies only on data from bubble-free MI that do not show anomalous major element compositions.

By including only bubble-free MI data in this interpretation, it is not necessary to account for any volatiles that might have been lost to the bubble after trapping of a single homogeneous silicate melt phase. Even though bubble-free MI may have been affected by H loss, we argue that extensive diffusive H loss would lead to the formation of a vapor bubble (Steele-MacInnis et al., 2017). Thus, the lack of a bubble supports the interpretation that H loss was not significant for the bubble-free MI considered here. Moreover, we do not observe any correlation between CO$_2$ and H$_2$O as would be expected if all MI started with the same volatile contents, and each MI experienced different degrees of H loss (Bucholz et al., 2013). Also, If diffusive H loss is only controlled by redox reactions of the MI-host system (Danyushevsky et al., 2002a), then it is unlikely that a significant amount of H$_2$O was lost from the MI because magnetite that would be produced by this process it is not observed in the studied MI.

Finally, it is important to note that filtering the MI data based on the presence or absence of a bubble may mask the complete variability represented by all the MI. In fact, it is more likely that a volatile-rich MI will form a bubble after trapping, compared to an MI that is relatively volatile-poor. Considering only bubble-free MI may unintentionally exclude some MI that trapped melts with higher volatile contents. We suggest that the best practice would be to analyze the volatile contents of the MI bubble and correct the original volatile content using methods described in the literature (e.g., Esposito et al., 2011; Mironov et al., 2015; Moore et al., 2015). In the next section, we interpret the H$_2$O-CO$_2$ data of MI from CF and IP volcanic fields considering only bubble-free MI.

6.2.1. H$_2$O and CO$_2$ degassing, crystallization and mixing of basaltic-trachybasaltic magmas

The volatile content of the glass phase in MI can be used as a geobarometer because CO$_2$ and H$_2$O solubilities in silicate melts are highly pressure dependent (Blundy and Cashman, 2008). A large range in CO$_2$ contents of MI, combined with a narrow range of H$_2$O concentrations, is often interpreted to reflect MI trapping along a degassing (ascent) path because CO$_2$ is lost from the melt early and before significant H$_2$O loss occurs. In this scenario, MI are trapped during crystallization of phenocrysts at different depths (pressures) as the magma ascends through

the crust. Alternatively, different phenocrysts might trap MI from essentially the same silicate melt at various depths within a stagnant plumbing system. Thus, H_2O–CO_2 systematics within a single eruptive event can support or dismiss the hypothesis that crystallization in the plumbing system occurred under volatile-saturated conditions, and if the crystallization occurs over a large or narrow range of pressure (depths.)

For CF and IP, MI data from individual eruptions are often interpreted to represent trapping during ascent as the magma degasses (Arienzo et al., 2016; Arienzo et al., 2010; Cecchetti et al., 2001; Cipriani et al., 2008; Esposito et al., 2011; Esposito et al., 2014; Mangiacapra et al., 2008; Moretti et al., 2013; Mormone et al., 2011) and that crystallization occurred under volatile-saturated conditions, and over a large range of pressures. As reported above, earlier studies interpreted the variability in H_2O vs. CO_2 systematics observed in MI as a combination of trapping at various depths along a degassing path, combined with episodic CO_2 fluxing events (Arienzo et al., 2016; Arienzo et al., 2010; Mangiacapra et al., 2008; Moretti et al., 2013; Mormone et al., 2011). However, we emphasize that "shrinkage" bubbles are often reported in MI from studies advocating for CO_2 fluxing, and most workers do not distinguish between bubble-free and bubble-bearing MI, nor do they account for volatiles contained in the bubble. Because these studies do not discuss these issues, their interpretations concerning degassing and CO_2 fluxing cannot be tested because the true, pre-eruptive volatile contents of the melt are unknown. In fact, Esposito et al. (2011), Hartley et al. (2014), Moore et al. (2015) and Esposito et al. (2016) all demonstrated that the bubble may contain as much as 99% of the originally trapped CO_2. For this reason, the discussion that follows is based on data from bubble-free MI only.

When we consider bubble-free MI of basaltic and trachybasaltic composition, the distribution of H_2O-CO_2 data shows less variability relative to data from all types of MI (bubble-free and bubble-bearing). The maximum CO_2 content of bubble-free MI (1248 ppm) is lower than that of bubble-bearing MI (1706 ppm). Also, the H_2O content of bubble-free MI shows less variability relative to the bubble-bearing group. Thus, the large variability in CO_2 contents combined with the narrow range of H_2O contents of bubble-free MI is more pronounced relative to bubble-bearing MI, suggesting that the magma was volatile-saturated and that olivine crystallized at various depths. For this discussion, we consider bubble-free MI as well as one bubble-bearing MI for which the original CO_2 content was corrected based on Raman analysis of the vapor bubble (MI RESC2-O26-MI3; Esposito et al., 2011).

In order to test the hypothesis that trapping of MI occurs during fractional crystallization under volatile-saturated conditions at various sub-volcanic depths, we computed fractional crystallization paths using the rhyolite-MELTS code (Ghiorso and Gualda, 2015). We considered MgO-rich bulk rocks from the IP and noted that the Al_2O_3/K_2O ratios of these rocks span a wide range (Figs. 6 and 7). We performed fractional crystallization calculations using rhyolite-MELTS to test if the general trend in Al_2O_3/K_2O vs. MgO systematics of bulk rocks is consistent with trends predicted during fractional crystallization. The first question we addressed was whether the previously reported MgO-rich bulk rock compositions can be assumed to represent liquid compositions. D'Antonio and Di Girolamo (1994) and D'Antonio et al. (1999a) noted that, for some of the bulk rocks, olivine phenocrysts may represent cumulus material and would thus be considered xenocrysts. In the studies by D'Antonio and Di Girolamo (1994) and D'Antonio et al. (1999a), the olivine showing the highest forsterite content was compared to the olivine composition predicted using various partition coefficients, KD_{Fe-Mg}, following the method of Rhodes (1981). These calculations indicated that olivine compositions in some of the bulk rocks were sometimes significantly different from the predicted olivine compositions, but the forsterite content of olivine never exceeded the calculated values (Table 3). Using the same bulk rock data from the literature, we compared the olivine composition calculated at the liquidus using rhyolite-MELTS with the observed data, as reported in

Table 3. We noted that the olivine compositions of the bulk rocks are comparable to the olivine composition predicted by rhyolite-MELTS, assuming 200 MPa, NNO, and H_2O–CO_2 saturation (see discussion below). In particular, bulk rock sample Apr22 shows Fo_{max} of 86.6. The rhyolite-MELTS predictions showed that a liquid composition equivalent to Apr22 is in equilibrium with $Fo_{87.3}$ at its liquidus (Table 3). D'Antonio and Di Girolamo (1994) reported that bulk rock Apr22 contains 11 vol% phenocrysts (olivine plus clinopyroxene). In other samples olivine ranges from 2.2 to 12.8 vol%, and clinopyroxene ranges from 2.5 to 7.6 vol%. We used the rhyolite-MELTS predictions as a starting composition to evaluate the consistency of predicted volume proportions of olivine and clinopyroxene and compared these values to values reported in the literature. According to these calculations, the magma should contain 12 vol% phenocrysts (olivine plus clinopyroxene) and 88 vol% liquid after ~115 °C cooling. At this stage, the magma contains ~4 vol% olivine and ~8 vol% clinopyroxene. The liquid would initially be in equilibrium with an Fo_{87} olivine and the final olivine to crystallize would be Fo_{84}. These results are consistent with the information reported in the literature and support the interpretation that trapping of MI occurs during fractional crystallization.

We selected five starting compositions for rhyolite-MELTS calculations: three bulk rock compositions, and two MI compositions that were corrected for PEC. Sample Apr18 (D'Antonio and Di Girolamo, 1994) was selected because this bulk rock composition shows both the highest MgO content and highest Al_2O_3/K_2O ratio. We also selected Apr22 (D'Antonio and Di Girolamo, 1994) because this rock showed the best match between the maximum forsterite content of olivine and the composition of olivine calculated to be in equilibrium with the rock composition on its liquidus (Table 3). In addition, we selected an initial composition that was based on the MI exhibiting the highest Al_2O_3/K_2O ratio [RESC5-O5-MA; Esposito et al. (2011)]. It is important to note that while bulk rock compositions can be affected by secondary processes (such as post depositional water-rock interactions) or entrainment of xenocrysts, the compositions of MI should not be affected by entrainment of xenocrysts into the surrounding liquid. As described by Fowler et al. (2007), we started with the uncorrected composition of MI RESC5-O5-MA (Esposito et al., 2011) and added aliquots of olivine host until the MI composition was in equilibrium with the host olivine measured adjacent to the MI. This allowed us to correct the MI composition for the effects of PEC. The fourth composition selected was bulk-rock sample Ps3 reported by Di Girolamo et al. (1984) because this composition shows relatively high MgO and relatively low Al_2O_3/K_2O. Finally, we selected the uncorrected composition of MI RESC3-O9-MA described by Esposito et al. (2011). This MI showed relatively low Al_2O_3/K_2O and the host olivine had a high forsterite content. We applied the same correction for PEC that was applied to MI RESC5-O5-MA.

Using these five initial compositions, we ran the models using specific starting conditions. For the bulk rocks (Apr18, Apr22 and Ps3), we calculated the liquid line of descent using rhyolite-MELTS, assuming H_2O (1.25 wt%) and CO_2 (1400 ppm) contents based on the H_2O–CO_2 systematics of bubble-free MI hosted in olivine. We assumed 200 MPa as the initial pressure, consistent with solubility experiments under volatile-saturated conditions for a trachybasaltic melt at the H_2O–CO_2 concentrations of our models (Fanara et al., 2015). As shown in Fig. 8, isobaric crystallization in the absence of volatile saturation produces trends that are inconsistent with the mafic MI data. Specifically, during crystallization at volatile-undersaturated conditions, both H_2O and CO_2 concentrations increase simultaneously. Conversely, the calculated trends based on bubble-free, basaltic-trachybasaltic MI data are consistent with polybaric crystallization under volatile-saturated conditions. For the model using the MI composition as the starting composition (PEC-corrected MIs RESC5-O5-MA and RESC3-O9-MA), we normalized the measured volatile contents to 100%, resulting in 1.21 wt% H_2O and 954 ppm CO_2 for RESC5-O5-MA, and 1.13 wt% H_2O and 479 ppm CO_2 for RESC3-O9-MA, respectively. The pressure at
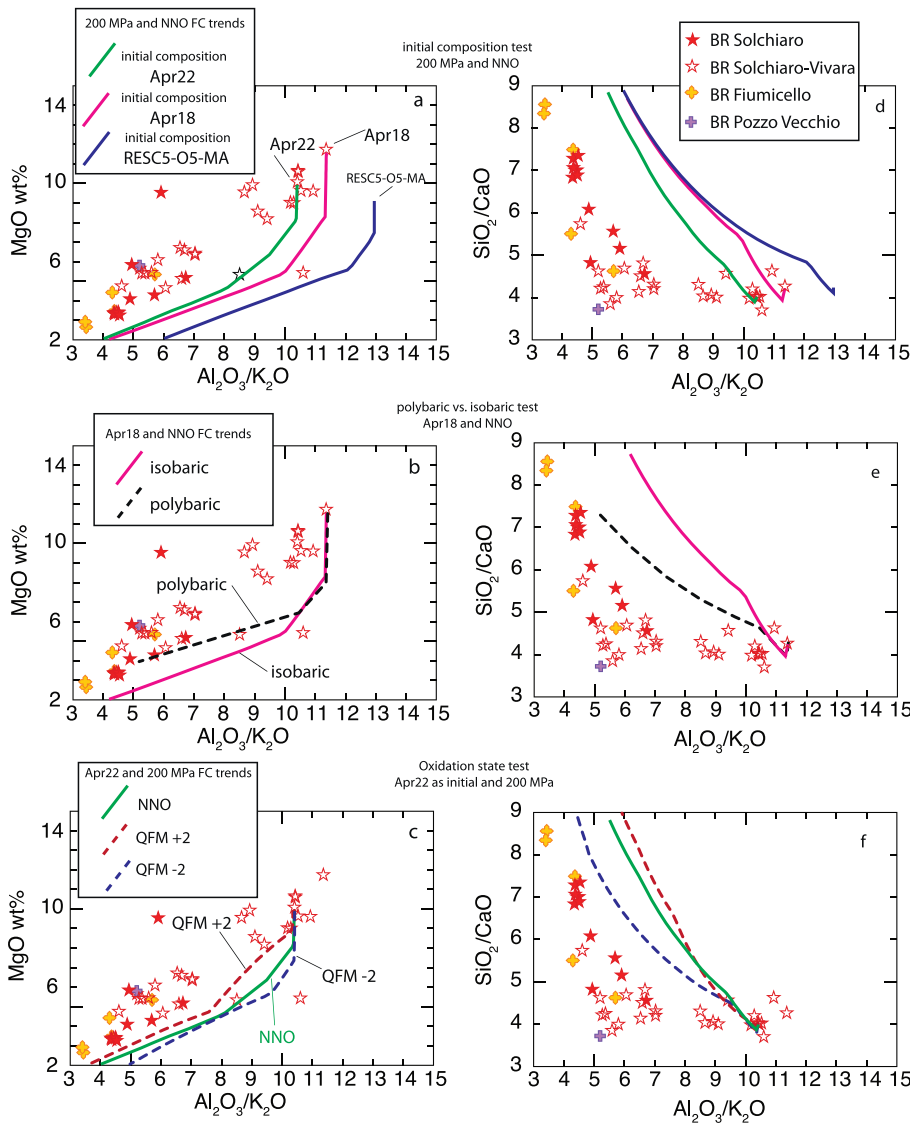
Fig. 6. Major element compositions of mafic bulk rocks from Procida and crystallization trends predicted by Rhyolite-MELTS using starting compositions based on bulk rocks or MI showing high Al_2O_3/K_2O. a), b) and c): MgO vs. Al_2O_3/K_2O; d), e) and f): SiO_2/CaO vs. Al_2O_3/K_2O. Symbols are for bulk rock compositions from Procida from the literature: red-filled stars = Solchiaro eruption (De Astis et al., 2004; Di Girolamo et al., 1984); red-open stars = Vivara or Solchiaro eruptions (D'Antonio et al., 1999a); yellow crosses = Fiumicello eruption; purple cross = Pozzo Vecchio eruption (Di Girolamo et al., 1984). Trends were calculated using rhyolite-MELTS (Gualda and Ghiorso, 2015) with three initial compositions: Apr22, Apr18 (bulk rocks; D'Antonio et al., 1999a), or RESC5-O5-MA (MI; Esposito et al., 2011). Panels a) and d) show results obtained using the three initial compositions at constant pressure of 200 MPa and at NNO oxidation state. Panels b) and e) show results obtained using Apr18 as the starting composition, the NNO redox buffer, and comparing isobaric versus polybaric crystallization paths (see text for details). Panels c) and f) show results obtained using Apr22 as the initial composition, constant pressure of 200 MPa, and assuming oxidation states of NNO, QFM + 2 and QFM-2. The trends were calculated assuming the melt is saturated with respect to H_2O-CO_2. The calculated trends show a poor fit to the bulk rock data, suggesting that initial melts equivalent to the high Al_2O_3/K_2O bulk rocks and MI cannot generate the observed geochemical trends by crystal fractionation alone. (For interpretation of the references to colour in this figure legend, the reader is referred to the web version of this article.)

volatile saturation (thus, the initial pressure in the models) was 160 MPa for RESC5-O5-MA and 90 MPa for RESC3-O9-MA.

6.2.1.1. Effect of starting composition. The first step was to test if the three high- Al_2O_3/K_2O starting compositions (Apr18, Apr22, and RESC5-O5-MA) could reproduce the geochemical trends defined by bulk rocks, the phases that crystallized, and the compositions of the phases. For this test, we assumed isobaric crystallization and a fixed oxidation state. The results are shown in Figs. 6, 9-11. The three starting compositions do not reproduce consistent geochemical trends for MgO and SiO_2/CaO vs. Al_2O_3/K_2O (Fig. 6a and d). The range of olivine compositions is consistent with the range from previous studies (Fig. 12). However, the calculated trend in Fo mol% vs. Al_2O_3/K_2O space does not agree with data from the bubble-free MI (Fig. 12). The clinopyroxene compositions predicted by rhyolite-MELTS show a good match with measured compositions (Fig. 9a), but the calculated feldspar compositions do not reproduce the observed alkali-feldspar composition (Fig. 10a). On the TAS diagram, only data from sample Apr22 produces a trend that is consistent with the "normal" MI compositions from the literature and from this study, but all three starting compositions reproduce the trachybasalt-shoshonite-latite-phonolite/trachyte bulk rock trend (Fig. 11a). It is important to note that the MI data plotted in the TAS diagram can be used to track the

stage in the differentiation sequence that the host phase for each MI crystallized, and we compared the relative timing of olivine, clinopyroxene and sanidine formation predicted by rhyolite-MELTS with results based on MI. For the Apr22 experiment, sanidine crystallization was predicted only during the last stages of crystallization, which does not match with compositions of MI hosted in sanidine. In addition, rhyolite-MELTS predicts that clinopyroxene crystallization ended earlier than sanidine crystallization, and that these two phases did not crystallize in equilibrium, in disagreement with petrographic analysis of more evolved rocks (e.g., Di Girolamo et al. 1984). Trends predicted by rhyolite-MELTS for MI and Apr18 starting compositions do not reproduce the observed crystallization trend of alkali-feldspar.

We also examined if the low-Al_2O_3/K_2O bulk rock composition and/or MI compositions would produce a better match between rhyolite-MELTS predictions and data from natural samples. For MgO and SiO_2/CaO vs. Al_2O_3/K_2O, the predicted fractional crystallization trends are consistent for the general bulk rock data for Al_2O_3/K_2O < 7 (Fig. 13). As shown in Figs. 7a and d and 13a, the match applies not only to bulk rock data, but also to MI data. What is even more striking is the match between rhyolite-MELTS predictions and "normal" MI in the TAS diagram. Experiments assuming Ps3 and RESC3-O9-MA as the starting composition better predicted the occurrence of sanidine crystallization,
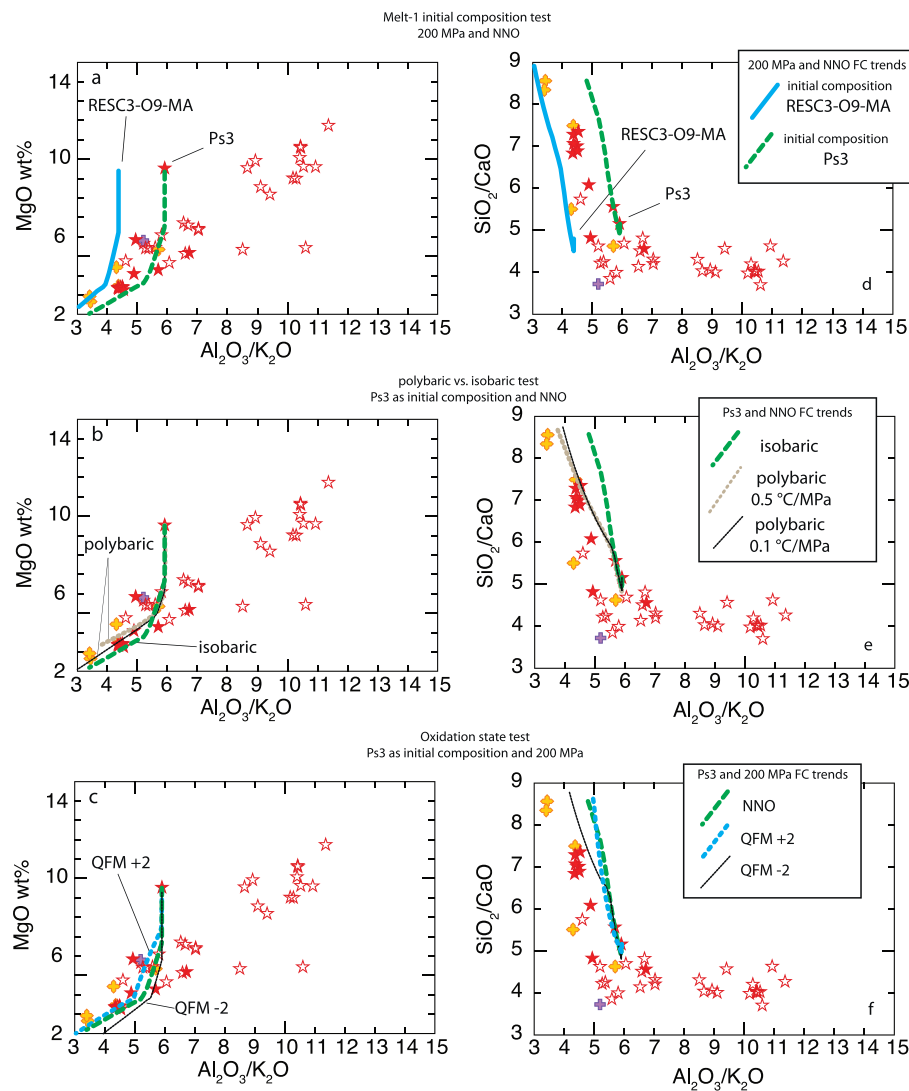
Fig. 7. Major element compositions of mafic bulk rocks from Procida and calculated crystallization trends using bulk rocks and MI showing low Al_2O_3/K_2O. a), b) and c): MgO vs. Al_2O_3/K_2O. d), e) and f): SiO_2/CaO vs. Al_2O_3/K_2O. Symbols are the same as in Fig. 6. Trends were calculated using rhyolite-MELTS (Gualda and Ghiorso, 2015) with two initial compositions: Ps3 (bulk rock; Di Girolamo et al., 1984) and RESC3-O9-MA (MI; Esposito et al., 2011). Panels a) and d) show results obtained using the two initial compositions, a constant pressure of 200 MPa and at oxidation state equal to NNO. Panels b) and e) show results obtained using Ps3 as the starting composition, the NNO buffer, and compare isobaric versus polybaric crystallization paths (see text for details). Panels c) and f) show results obtained using Ps3 as the initial composition, constant pressure of 200 MPa, and oxidation states of NNO, QFM + 2 and QFM-2. The trends were calculated assuming that the melt is saturated with respect to H_2O-CO_2. Note that trends show a good fit with the bulk rock data at low Al_2O_3/K_2O ratios, suggesting that the low Al_2O_3/K_2O rocks and MI are compatible with trends predicted based on crystal fractionation.

relative to calculations based on Apr22 and Apr18 and RESC5-O5-MA reported above. In addition, RESC3-O9-MA experiments predicted clinopyroxene crystallization throughout the fractionation trend and that clinopyroxene coexisted with sanidine. The only mismatch for this run is that olivine crystallization ended later in the differentiation sequence than is observed in the samples. However, as shown in the supplementary material (Appendix Table C.1-13), the mass fraction of olivine crystallizing as the path moves through the shoshonite field continuously decreases. Thus, predictions based on Ps3 and RESC3-O9-MA starting compositions are in better agreement with observations, compared to Apr22, Apr18, and RESC5-O5-MA for both the TAS trend

and mineral phase appearance (Fig. 11d). The same conclusion can be drawn for the feldspar compositions (Fig. 10d). The plagioclase compositions predicted by Ps3 and RESC3-O9-MA starting compositions are more representative of plagioclase compositions reported in the literature. In addition, the trends extend toward a higher sanidine component and show better agreement with sanidine compositions from the literature. The trend predicted for Fo mol% vs. Al_2O_3/K_2O, assuming Ps3 and RESC3-O9-MA starting compositions, is consistent with several of the MI compositions (Fig. 12).

6.2.1.2. Effect of pressure (depth) evolution during crystallization. In

Table 3

Calculated Fo_{max} predicted by rhyolite-MELTS compared with the Fo_{max} reported by D'Antonio and Di Girolamo (1994).

Bulk rock[a]	18-Apr	22-Apr	1-Apr	16-Apr	20-Apr
Phenocryst Vol% observed[a]	18	11	19	12	11
Olivine vol%[a]	2.2 to 12.8	2.2 to 12.8	2.2 to 12.8	2.2 to 12.8	2.2 to 12.8
Cpx vol%[a]	2.5 to 7.6	2.5 to 7.6	2.5 to 7.6	2.5 to 7.6	2.5 to 7.6
Fo(max) analyzed[a]	87.3	86.6	87.4	na	86.9
Fo(max) calculated[a]	89.8–91.5	88.1–90.0	87.1–89.2	na	86.4–88.6
Phenocryst Vol% from MELTS this study	18	12	na	na	na
Olivine vol% from MELTS this study	3	4	na	na	na
Cpx vol% from MELTS this study	15	8	na	na	na
Fo(max) from MELTS this study	88.7	87.35	86.4	85.8	85.76

[a]D'antonio and Di Girolamo (1994)
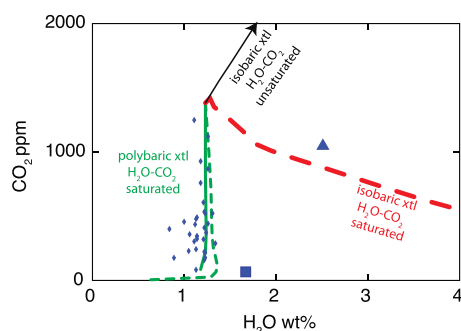
Fig. 8. H_2O-CO_2 systematics of bubble-free MI, with calculated crystallization trends predicted by rhyolite-MELTS (Gualda and Ghiorso, 2015). Note that the bubble-free MI shown exclude any MI deemed anomalous based on major-element compositions (see text for details). Symbols are the same as those in Fig. 3, and uncertainties on each data point are the same as in Fig. 4. Fractional crystallization trends are labelled as H_2O-CO_2 saturated isobaric versus polybaric, as well as H_2O-CO_2 undersaturated. Note that the H_2O-CO_2 systematics of MI hosted in olivine are consistent with polybaric crystallization under H_2O-CO_2 saturated conditions.

order to better understand if crystallization occurred while the magma was ponded in the subsurface (at a constant pressure) or occurred in the plumbing system as the magma ascended through the crust, we ran rhyolite-MELTS experiments assuming both isobaric and polybaric trends. We first selected sample Apr18 and assumed isobaric crystallization under volatile-saturated conditions at 200 MPa. In addition, we ran the same model under polybaric conditions with crystallization occurring as the pressure dropped from 200 to 14 MPa. The oxidation state was fixed by the NNO buffer in both examples. We note that the polybaric model improves the fit for alkali feldspar compositions (Fig. 10b). However, the TAS trend does not improve, and sanidine crystallization is predicted to occur later than is suggested by MI hosted in sanidine (Fig. 11b). In addition, the predicted SiO_2 concentration extends toward rhyolitic liquid. It is worth noting that for polybaric conditions, rhyolite-MELTS does not predict the formation of Ca–Ti-rich clinopyroxene.

We also considered Ps3 as the starting composition and compared the isobaric trend at 200 MPa with two polybaric trends. The polybaric model conditions were defined based on H_2O vs. CO_2 systematics (Fig. 8). The first polybaric trend assumed a 0.5 °C/MPa path from 200 MPa to 5 MPa, at which point the CO_2 content of the melt was 2 ppm. After the pressure reached 5 MPa, continued fractional crystallization was assumed to be isobaric. The second polybaric model assumed a 0.1 °C/MPa path from 200 MPa to 11 MPa, or until the CO_2 concentration in the melt was 9 ppm. Continued crystallization was assumed to be isobaric at 11 MPa. As can be seen in the SiO_2/CaO vs. Al_2O_3/K_2O trends, the polybaric models provide a better fit to the bulk rock and MI data (Fig. 7b and e). The difference between isobaric and polybaric conditions is not significant for the TAS trends. However, differences are observed during the final differentiation steps, and sanidine appearance occurs at the limit of the field defined by MI hosted in sanidine. The polybaric model shows a better fit to the sanidine compositions from the literature (Fig. 10e). Importantly, Ca–Ti-rich clinopyroxene is not predicted in two of the polybaric crystallization models (Fig. 9e).

6.2.1.3. Effect of oxidation state on predicted trends. The final test using rhyolite-MELTS examined potential effects of oxidation state on the differentiation trends by varying oxygen fugacity over the range from QFM − 2 and QFM + 2. We assumed isobaric crystallization and Apr22 as the starting composition. We recognize that oxidation state is expected to vary during extended periods of crystal fractionation (e.g., Moussallam et al., 2014), but we have not conducted experiments that allow the oxygen fugacity to vary during a

crystallization sequence.

Our results for Apr22 suggest that oxidation state does not significantly affect the various geochemical trends predicted by rhyolite-MELTS that were tested here. Trends for MgO and SiO_2/CaO vs. Al_2O_3/K_2O show similar patterns that do not match the bulk rock trends (Fig. 6c and f). The various oxidation states tested did not reproduce TAS trends during crystallization of clinopyroxene for the most evolved compositions (Fig. 11c and f), and feldspar compositions predicted by the models do not improve the match with the real data (Fig. 10c).

We also selected sample Ps3 (low Al_2O_3/K_2O ratio) as the starting composition with a range of oxidation states from QFM − 2 and QFM + 2. The different oxidation states have little effect on the liquid trend during the initial differentiation step (Fig. 7c and f). The match between predicted feldspar compositions and feldspar compositions from the literature does not improve (Fig. 10f). Varying the oxidation state did affect the trajectory of the liquid on the TAS diagram and the trends for different oxidation states delimit a field consistent with the MI data (Fig. 11f), an observation that is consistent with an evolving oxidation state during fractional crystallization.

6.2.1.4. Summary of rhyolite-MELTS modeling results. Selecting initial compositions based on bulk rocks and MI with high MgO concentrations and Al_2O_3/K_2O ratios does not yield trends consistent with the analytical data. In contrast, it is reasonable to infer that samples Ps3 (bulk rock) and RESC3-O9-MA (MI) represent mafic liquids that could produce geochemical trends toward trachytic and phonolitic melts during fractional crystallization. The consistency between bulk rock data, data from bubble-free MI, and rhyolite-MELTS predictions supports this hypothesis. In addition, the phases predicted to form during crystallization, and their compositions, are consistent with the literature data. Furthermore, the TAS trends based on "normal" MI and the correlation between MI composition and host mineral match with rhyolite-MELTS predictions. In particular, the predicted order of appearance of mineral phases is in good agreement with the phase fields defined by the MI compositions and the compositions of the MI hosts. The best agreement between the model results and the analytical data is obtained when the crystallization path is polybaric, especially for sanidine compositions and the predicted absence of Ca–Ti-rich clinopyroxene. The oxidation state does not appear to significantly influence the results.

To compare bubble-free MI data with rhyolite-MELTS trends and bulk rock data, we compared ratios of olivine-incompatible elements (e.g., SiO_2/CaO and Al_2O_3/K_2O) rather than using absolute concentrations of elements in MI (Fig. 13a and b). Comparing olivine-incompatible element ratios minimizes the effect of PEC (Lima et al., 2003) and these ratios are independent of methods used to correct the MI compositions (e.g., Danyushevsky et al., 2002a). As shown by the SiO_2/CaO vs. Al_2O_3/K_2O trends in Fig. 13, the major element ratios suggest that bubble-free MI cannot be explained solely by a single fractional crystallization trend starting from a single primitive melt. As for bulk rocks, a group of MI (hereafter referred to as Mixed-MI) forms a trend consistent with a mixing model (Fig. 14), and another group of bubble-free MI (hereafter referred to as Melt-1 MI) is consistent with simple fractional crystallization from Melt-1. These groups of bubble-free MI overlap with the same two groups of bulk rocks that can be identified based on geochemistry (Fig. 13a). It is important to note that the overlap in bulk rock composition and compositions of several MI indicates that the examined bulk rocks can be assumed to be representative liquids of magmas associated with volcanism at CF and IP. Consequentially, SiO_2/CaO or MgO vs. Al_2O_3/K_2O trends of bulk rocks cannot be the result of plagioclase crystal assimilation. Some of the trace element ratios of bubble-free MI show the same behavior as ratios of major elements, showing two distinct trends that cannot be produced by simple crystallization from a single starting composition represented by either Melt-1 or Mixed-MI and bulk rocks showing high-Al_2O_3/K_2O. For instance, Rb, Pb, Ba, U, Th, Nb, Ce, La, Pr, and Ta show the same
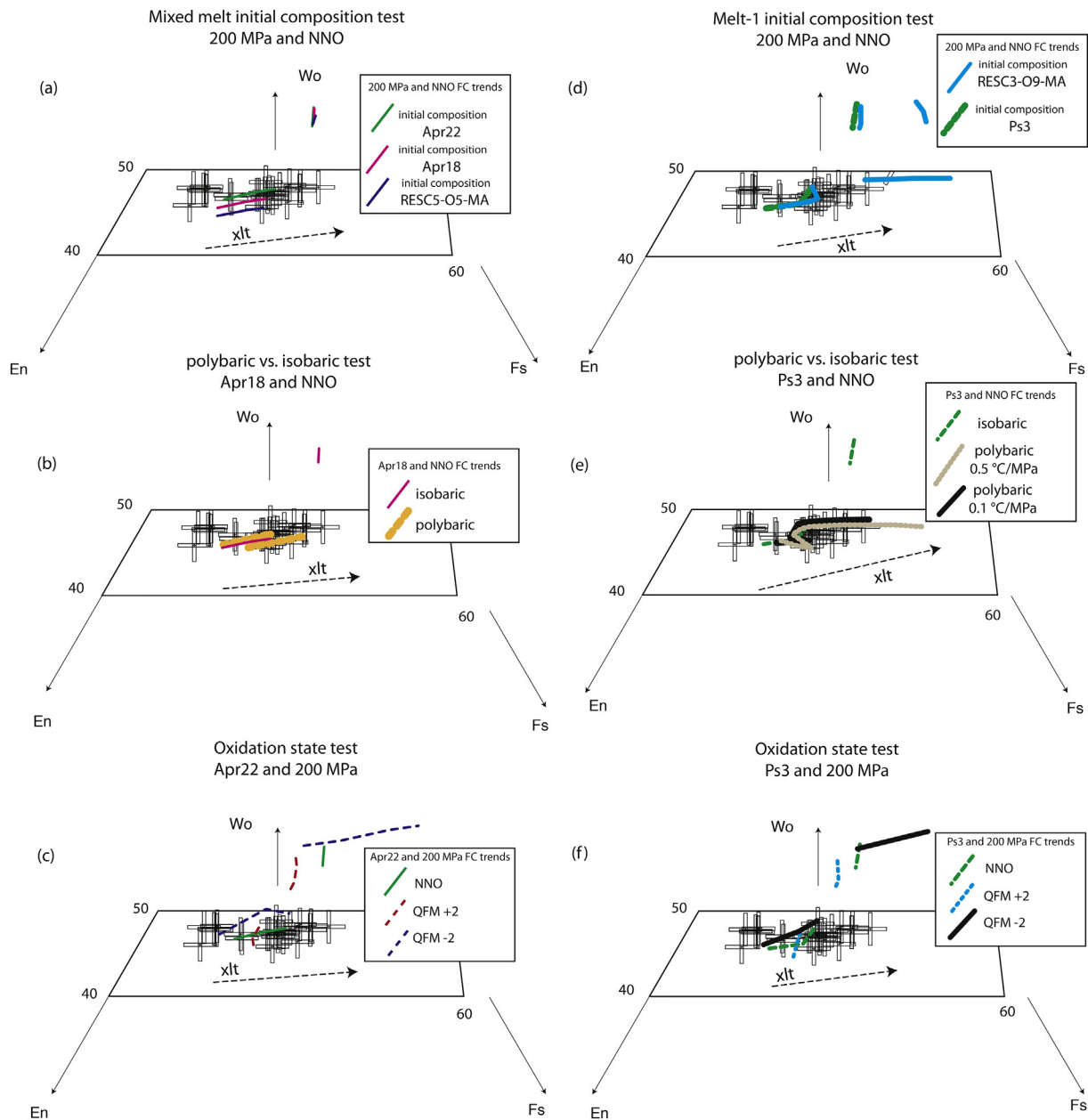
Fig. 9. Compositions of clinopyroxenes hosting MI from this study and clinopyroxene compositions predicted by rhyolite-MELTS (Gualda and Ghiorso, 2015). Panels a), b) and c) compare measured clinopyroxene compositions with those predicted by the models using high-Al_2O_3/K_2O bulk rocks and MI (Apr22, Apr18 and RESC5–05-MA; as in Fig. 6). Crosses are clinopyroxene analyses, and line styles are the same as in Fig. 6. Panels d), e) and f) compare measured clinopyroxene compositions with those predicted by the models using low-Al_2O_3/K_2O bulk rocks and MI (Ps3 and RESC3–09-MA; as in Fig. 7). Line styles are the same as in Fig. 7. Note that trends calculated using Ps3 as starting composition and polybaric fractional crystallization (panel e) show the best fit.

trend as K_2O in the SiO_2/CaO vs. Al_2O_3/K_2O diagram. The Mixed-MI form a different trend relative to Melt-1 MI (Fig. 14a). The same behavior is observed when trace element ratios are plotted against each other (e.g., Ba/Sr vs. Yb/Rb and Eu/Rb Fig. 14 b and c). We used a simple binary mixing model based on Albarède (1996) assuming MI compositions RESC5-O5-MA (for Mixed-MI) and RESC3-O9-MA (for Melt-1) as end members.

Spider diagrams also highlight the difference between Mixed-MI and Melt-1 MI (Fig. 15). For instance, the Primitive Mantle-normalized spider diagram (Sun, 1980) shows that the normalized LILE are generally lower for Mixed-MI, but that the same Mixed-MI show generally higher normalized HFSE (Fig. 15 c). Comparing the less evolved Melt-1 MI (RESC3-O9-MA) with the mixed MI that shows the strongest evidence of mixing (RESC5-O5-MA) highlights the difference in trace

element contents, such as for Rb, P, Eu, and Yb (Fig. 15c). These two MI are hosted in olivine with similar forsterite content and, therefore, crystal fractionation cannot be invoked to explain the difference in the trace element patterns. Similar observations are suggested from the REE spider diagrams (Sun and McDonough, 1989), whereby Mixed-MI show lower normalized LREE but generally higher normalized HREE, relative to Melt-1 MI (Fig. 15b). It is important to note that for intermediate REE, the two groups of MI overlap, with more erratic behavior shown by Mixed-MI. These observations indicate that the difference between these two groups cannot be explained by simple fractional crystallization but, rather, are explained by mixing of two different primitive melts. This is in agreement with D'Antonio et al. (2007), who suggested that primitive magmas of differing composition can be generated by contamination of the mantle source by various proportions of slab-
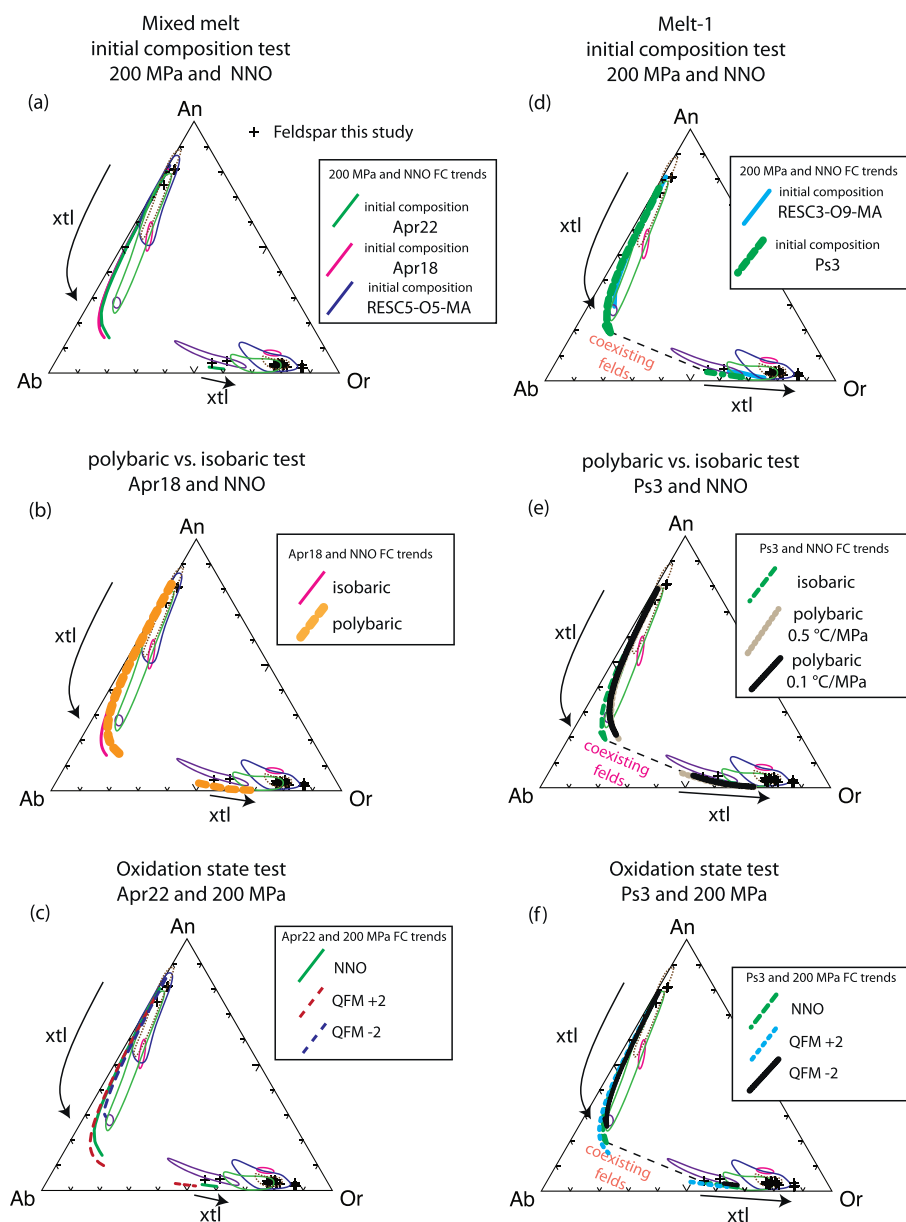
Fig. 10. Compositions of feldspars hosting MI analyzed in this study (cross symbols) and from the literature (encircled fields), compared to feldspar compositions predicted by rhyolite-MELTS (trend lines; Ghiorso and Gualda, 2015). Panels a), b) and c) compare measured feldspar compositions and those predicted by the models using high-Al_2O_3/K_2O bulk rocks and MI (Apr22, Apr18 and RESC5–05-MA; as in Fig. 6). Trend line styles are the same as in Fig. 6. Panels d), e) and f) compare measured feldspar compositions and those predicted by the models using low-Al_2O_3/K_2O bulk rocks and MI (Ps3 and RESC3–09-MA; as in Fig. 7). Line styles are the same as in Fig. 7. Note that the best fit is calculated using Ps3 as starting composition (see panels d), e) and f)).

derived fluids or by sediment-derived melts.

The systematics of Cl and S are also consistent with the mixing model proposed in this study. Here again, the Mixed-MI form well-defined trends and diverge from the general trend determined by Melt-1 MI (Fig. 16). This behavior can be observed in the Cl/Yb vs. Al_2O_3/K_2O plots, where the Mixed-MI show lower Cl/Yb and higher Al_2O_3/K_2O compared to Melt 1 MI (Fig. 16a). This suggests that, not only is Mixed-MI different from Melt-1 in terms of major and trace element trends, but also differs in terms of volatile contents.

To further test the hypothesis that mafic magmas beneath IP crystallize under volatile-saturated conditions and over a range of pressures, we first compared the volatile ratios (e.g., H_2O/CO_2) of bubble-free MI with the composition of the olivine hosts (Fig. 17a). It is important to note that the composition of the host was measured ~40 μm away from the MI/host interface (Esposito et al., 2011). No correlation is observed between H_2O/CO_2 ratio and the mol% Fo of the host.

The H_2O/CO_2 versus mol% Fo systematics could be explained by assuming different pressure-temperature evolution paths (Fig. 17a). A possible explanation of the different pressure-temperature paths is that feeding conduits of different geometries (e.g., thickness) could

transport magmas of different temperatures to the same depth (Spera, 1980). Thus, cogenetic magmas of slightly different temperatures may occur at the same depth below a volcano. This scenario is consistent with the "mush column" model proposed by Marsh (1996). As summarized by Putirka (2017; see his Fig. 1a and c) and by Cashman et al. (2017), the plumbing system beneath a volcano represents a mosaic of scattered bodies which may or may not be connected to each other. The most likely result is that co-genetic magma pools in a plumbing system may follow different pressure-temperature paths, consistent with the variability of volatiles found in MI hosted in olivine that show the same forsterite contents (Fig. 17a). This scenario is also consistent with the presence of anomalous MI in olivine as discussed by Danyushevsky et al. (2004).

Volatile ratios were plotted versus Al_2O_3/K_2O to test for consistency between volatile content of MI and major element compositions of MI. The distribution of bubble-free MI data in the H_2O/CO_2 versus Al_2O_3/K_2O diagram is plotted along the same polybaric crystallization trends. As was observed for major, trace and other volatile element ratios, H_2O/CO_2 ratios of Melt-1 MI are consistent with polybaric crystallization trends of Melt-1 and Mixed-MI, which define a mixing trend
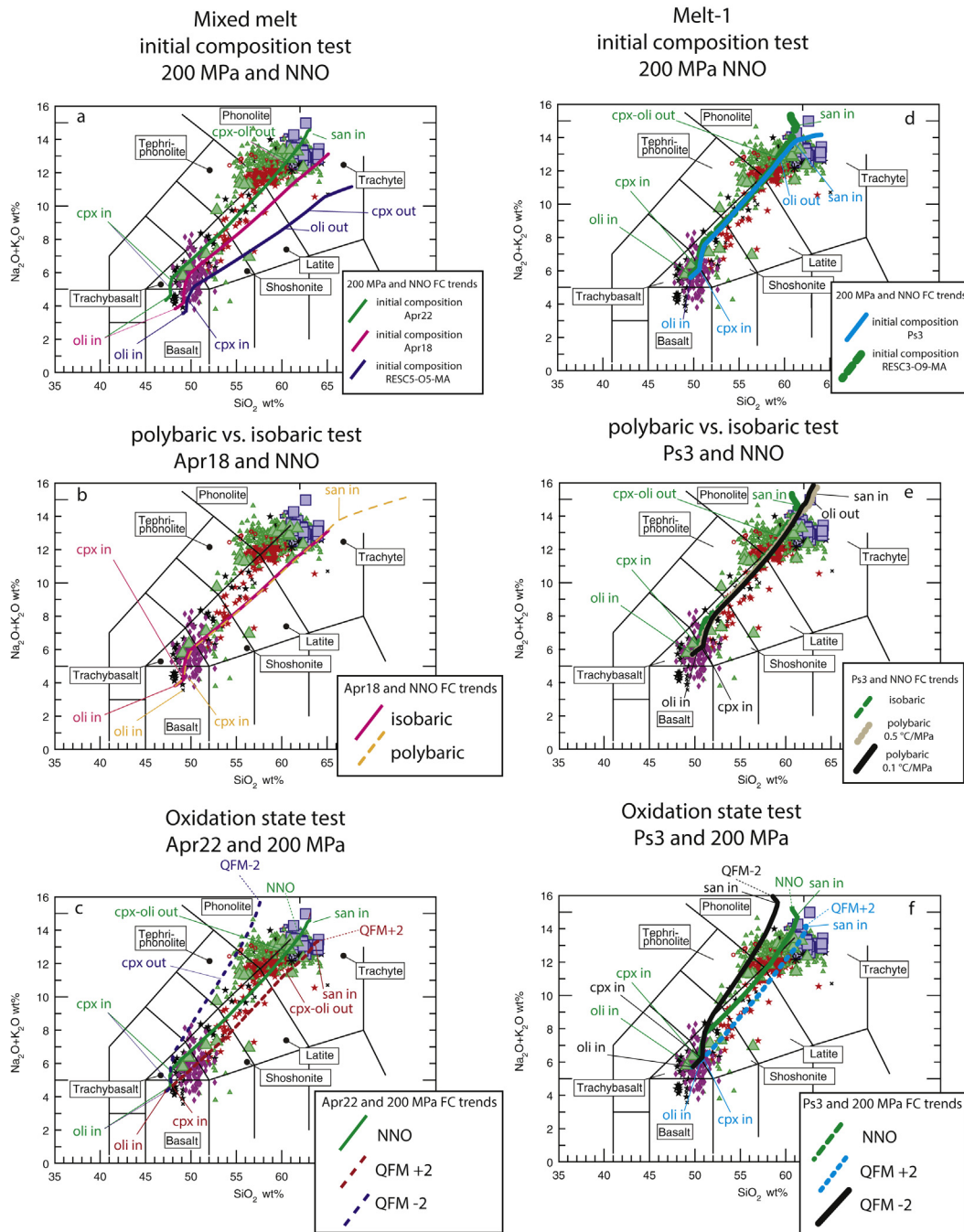
Fig. 11. TAS diagram comparing MI from CF and IP and liquid compositions predicted by Rhyolite-MELTS. Panels a), b) and c) compare MI compositions and liquid compositions predicted by the models using high-Al$_2$O$_3$/K$_2$O bulk rocks and MI (Apr22, Apr18 and RESC5–05-MA; as in Fig. 6). Trend line styles are the same as in Fig. 6. Panels d), e) and f) compare MI compositions and liquid composition predicted by the models using low-Al$_2$O$_3$/K$_2$O bulk rocks and MI (Ps3 and RESC3–09-MA; as in Fig. 7). Line styles are the same as in Fig. 7. In all panels, the appearance and disappearance of olivine, clinopyroxene, and sanidine predicted by rhyolite-MELTS are highlighted. Note the good fit between the phase field defined by the MI and their hosts and rhyolite-MELTS predictions, relative to the appearance and disappearance of olivine, clinopyroxene, and sanidine, especially for panels d), e) and f). Data references for MI are as in the main text.

(Fig. 17b).

We further investigated the chronology of the magmatic processes to assess whether crystal fractionation starting from Melt-1 occurred before or after mixing by examining textural and petrographic relationships of olivine and MI. First, we note that reverse zoning of olivine phenocrysts that were erupted in the IP is reported by many researchers (e.g., D'Antonio and Di Girolamo, 1994). Secondly, we re-evaluated data reported by Esposito et al. (2011) to search for correlations between type of zonation of the host olivine crystals of the bubble-free MI reported in their Table 3 and the type of MI defined

here. Also, we investigated the correlation between the position of the bubble-free MI within the host and the type of MI (Mixed-MI and Melt-1 MI) as defined here. This effort showed that 73% of the Mixed-MI are hosted in zoned olivine crystals and half of the Melt-1 MI are hosted in unzoned olivine phenocrysts. No Mixed-MI are hosted in the cores of olivine phenocrysts while the majority of Melt-1 MI are, indeed, hosted in olivine cores (Table 4). This textural and petrographic information suggests that fractional crystallization of Melt-1 began in the various magma pools below the volcano before the mixing event associated with the later Solchiaro eruption.
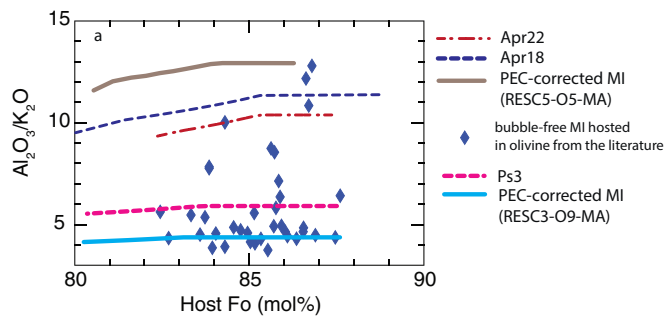
Fig. 12. Fo mol% of host olivine versus the respective Al_2O_3/K_2O ratios of olivine-hosted MI, compared with rhyolite-MELTS calculations assuming 200 MPa isobaric conditions. Symbols are as in Fig. 3, while trend line styles are as in Figs. 6 and 7. Note that for all calculations Al_2O_3/K_2O of liquids does not change significantly during crystallization, whereas the bubble-free MI show a large variation.

In conclusion, taken together, the volatile, major and trace element compositions of bubble-free MI, host-mineral compositions, bulk rocks, and trends predicted by rhyolite-MELTS models all suggest that crystallization of melt beneath Solchiaro first occurred by simple fractional crystallization under volatile-saturated conditions at depths between ~1 and 5 km (Fig. 18a). This interpretation is consistent with other MI studies that suggest that differentiation of magmas at shallow depths beneath CF and IP, as well as in the nearby Ischia Islands, is characterized by H_2O-CO_2 volatile saturation (Arienzo et al., 2016; Arienzo et al., 2010; Cannatelli et al., 2007; Cecchetti et al., 2001; Cipriani et al., 2008; Esposito et al., 2011; Fourmentraux et al., 2012; Mangiacapra et al., 2008; Mormone et al., 2011; Roach, 2005). Crystallization continued under polybaric conditions during magma ascent to shallower crustal levels. Well-constrained MI indicate that magmas in shallower reservoirs were slightly more evolved than those in deeper reservoirs, as predicted by Cashman et al. (2017). After this first stage dominated by magma ascent and crystallization, recharging by a second high-Al_2O_3/K_2O basaltic melt occurred at depths between ~1 to ~6 km (Fig. 18b). During this pre-eruptive stage, Melt-1 that had undergone varying degrees of crystallization mixed with various proportions of high-Al_2O_3/K_2O basaltic melt. Although mixing has been suggested previously based on the isotopic composition of bulk rocks from different localities and different degrees of differentiation (e.g., D'Antonio et al., 2007; D'Antonio and Di Girolamo 1994; Forni et al., 2018), our interpretation of mixing is based on MI and is representative of a single eruption (single location), with mixing between two near-primitive magmas showing similar degrees of differentiation. Most importantly, well-constrained bubble-free MI that record evidence of crystallization and mixing provide a chronological sequence of the magmatic processes occurring beneath Solchiaro. The recharging magma did not undergo extensive crystallization. In addition, well-constrained MI show no evidence for CO_2 fluxing as reported in other MI studies (e.g., Moretti et al., 2013). In fact, normal and bubble-free basaltic and trachybasaltic MI show that the H_2O contents remained essentially constant (within analytical error). In other words, well-constrained mafic MI show no evidence that H_2O/CO_2 decreases systematically with crystallization indicators (Fig. 17). Our results cannot disprove the CO_2 fluxing interpretation, but neither do the MI data support such an interpretation.

6.2.2. H₂O and CO₂ degassing during crystallization of trachytic magmas

After considering bubble-free MI from basaltic and trachybasaltic magmas, we investigated the bubble-free MI of more evolved magmas that likely originated from the differentiation of the same trachybasaltic melt. Ten bubble-free MI were analyzed in this study, nine of them are representative of the NYT magma and the other is from the Solfatara eruption. Seven bubble-free MI are hosted in sanidine and the other three are hosted in clinopyroxene. The low number of bubble-free MI
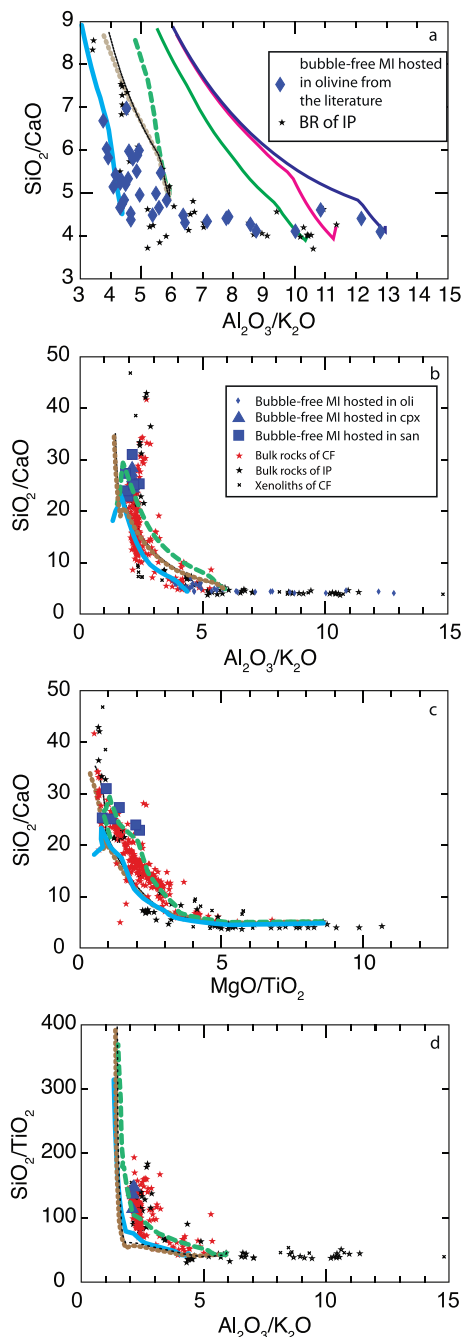

Fig. 13. Ratios of oxide concentrations (wt%), comparing bubble-free MI, bulk rock compositions and rhyolite-MELTS modeling results. The MI data exclude MI deemed anomalous based on major-element concentrations (see text for details). Symbols are the same as in Figs. 2 and 3, and trend line styles are the same as in Figs. 6 and 7. a) SiO_2/CaO vs. Al_2O_3/K_2O of basaltic and trachybasaltic bubble-free MI hosted in olivine. b) SiO_2/CaO vs. Al_2O_3/K_2O including trachytic bubble-free MI (symbols indicate host mineral). c) SiO_2/CaO vs. MgO/TiO_2 of bubble-free MI hosted in sanidine. d) SiO_2/TiO_2 vs. Al_2O_3/K_2O of bubble-free MI hosted in clinopyroxene.

analyzed is because bubble-free MI large enough for SIMS analysis are rare in the studied phenocrysts. The bubble-free MI from the NYT and Solfatara samples were likely trapped during isobaric crystallization at a relatively high pressure, ca. 200 MPa, followed by polybaric crystallization during ascent (Fig. 17c). This interpretation is consistent with the trend predicted by rhyolite-MELTS, starting from Melt-1 composition as reported above. Isobaric crystallization of a trachybasaltic
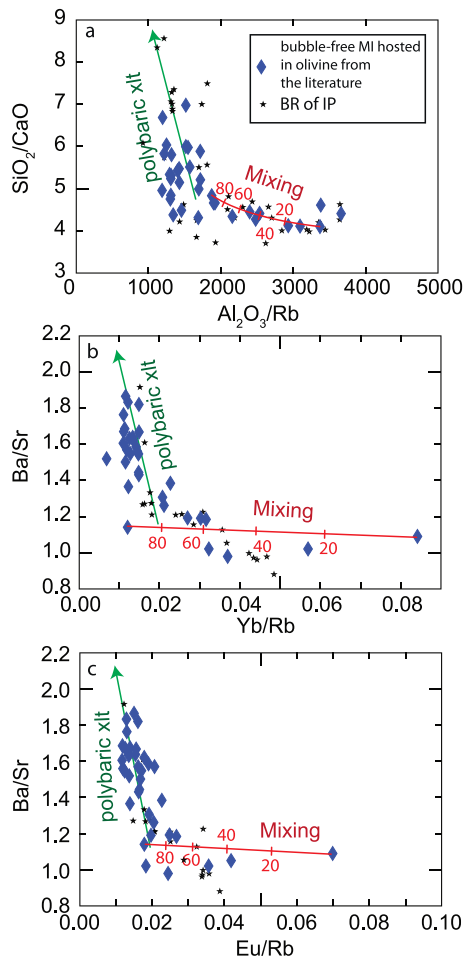
Fig. 14. Trace element compositions of bubble-free MI hosted in olivine. Symbols are the same as in Figs. 2 and 3. a) SiO$_2$/CaO vs. Al$_2$O$_3$/ Rb, b) Ba/Sr vs. Yb/Rb, and c) Ba/Sr vs. Eu/Rb. Note that for trace elements, fewer bulk rock data are available compared to major element data. The green arrow on each panel indicates the expected trend for polybaric crystallization. The red line on each panel represents a calculated mixing trend based on the same MI end members for all three panels. Mixing calculations were based on a simple binary mixing (Albarède, 1996). (For interpretation of the references to colour in this figure legend, the reader is referred to the web version of this article.)

Fig. 15. Spider diagrams of the MI and bulk rocks. Symbols in a) and b) are the same as in Figs. 2 and 3. a) Incompatible trace element spider diagram with normalization to primitive mantle as in (Sun, 1980), and b) Rare Earth elements spider diagram with normalization to chondrite as in Sun and McDonough (1989). c) Incompatible trace element spider diagram of two MI: RESC3-O9-MA and RESC5-05-MA. These two MI are hosted in olivine showing similar Fo-rich compositions, but these MI show very different Al$_2$O$_3$/K$_2$O ratios. Note that RESC3-O9-MA was selected as the low-Al$_2$O$_3$/K$_2$O starting composition for rhyolite melts simulations, whereas RESC5-05-MA was selected as the high-Al$_2$O$_3$/K$_2$O starting composition for these simulations, shown in Figs. 6 to 13.

magma at ~200 MPa under volatile-saturated conditions assumed here is consistent with results of other studies (e.g., Arienzo et al., 2010). A melt zone at ~200 MPa is also suggested by geophysical data (e.g., Zollo et al. (2008), not only for CF and IP but for all of the Neapolitan volcanic area (see Moretti et al., 2013 and references therein). While our interpretation is based on only a few well-constrained MI, we demonstrated that melts with high H$_2$O contents can be generated during fractional crystallization, starting from trachybasaltic melts. The elevated H$_2$O contents have obvious and important implications for generating high-magnitude (explosive) eruptions.

The composition of the trachytic bubble-free MI can be obtained after ~66% to 85% of isobaric crystallization under volatile-saturated conditions (Fig. 13b) (see also Appendix Table C.1-13). The mineral assemblage predicted by rhyolite-MELTS is consistent with the mineral assemblage of selected rock samples that are mainly composed of clinopyroxene and feldspar ± biotite and Ti-magnetite (see Appendix Table C.1-13). We discriminated between trachytic bubble-free MI by host using ratios of elements incompatible or slightly compatible with the host (Fig. 13c and d). For instance, bubble-free MI hosted in sanidine show good agreement with rhyolite-MELTS predictions and bulk rock trends for SiO$_2$/CaO vs. MgO/TiO$_2$ (Fig. 13c). Consistently,

bubble-free MI hosted in clinopyroxene show agreement with rhyolite-MELTS predictions and bulk rock trends for SiO$_2$/ TiO$_2$ vs. Al$_2$O$_3$/K$_2$O (Fig. 13d). It is important to note that trachytic bubble-free MI show good agreement even when ratios such as SiO$_2$/CaO (CaO highly compatible with clinopyroxene) and Al$_2$O$_3$/K$_2$O (K$_2$O and Al$_2$O$_3$ compatible with sanidine) are considered (Fig. 13b). These trends suggest that PEC or other modifications after trapping and before eruption were not extensive and did not significantly affect the composition of the trapped melt. The inferred low degree of PEC is also consistent with agreement between compositions of MI and the bulk rocks, and with the occurrence of bubble-free MI (Steele-MacInnis et al., 2011). CO$_2$ and H$_2$O contents are available for two bubble-free, trachytic MI from the NYT eruption. One bubble-free MI is hosted in clinopyroxene and the other in sanidine. The isobaric crystallization model is consistent with the volatile contents of bubble-free MI hosted in clinopyroxene, but not with the bubble-free MI hosted in sanidine (Fig. 16c). In order to evolve a melt with the volatile content recorded by the bubble-free MI hosted in sanidine, the system must crystallize at a lower pressure (shallower depth). Thus, our interpretation is that the last stage of crystallization for the NYT eruption occurs at shallower levels, compared to the earlier stages of crystallization. Under volatile-saturated conditions, the H$_2$O content of the melt can only increase if the magma evolves from trachybasalt to trachyte isobarically. With this scenario, the CO$_2$ content of
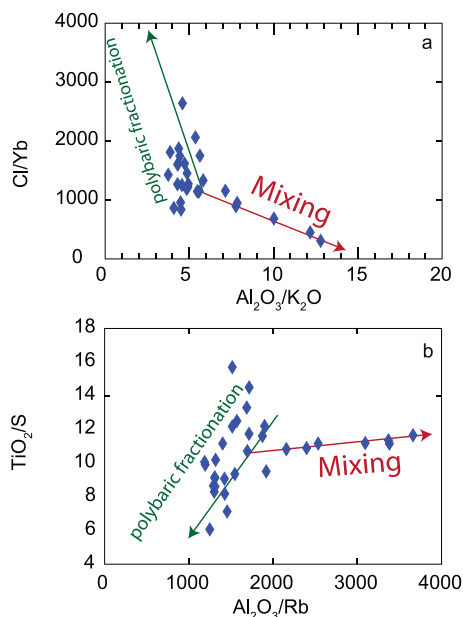
Fig. 16. Ratios of volatile, trace and major element compositions for bubble-free MI. Symbols the same as in Fig. 3. a) Cl/Yb vs. Al_2O_3/K_2O; b) TiO_2/S vs. Al_2O_3/Rb. Note that including Cl and S in these element ratio diagrams still differentiates the trends formed by the two different groups of MI as seen in Fig. 14. The arrows indicate trends predicted for polybaric fractional crystallization versus mixing.

the melt decreases and the melt becomes enriched in H_2O and the fluid exsolving from the melt becomes progressively enriched in H_2O (red dashed line in Fig. 8). The higher the pressure of isobaric crystallization, the higher the H_2O content of the evolved melts, as suggested by H_2O–CO_2–silicate melt solubility models. The higher the H_2O content of more evolved melts the greater the likelihood of a highly explosive eruption (e.g., NYT eruption), especially if crystallization occurs at relatively shallow depths where the difference between the partial molar volume of H_2O dissolved in the melt and the molar volume of H_2O-rich magmatic fluid is large (Bodnar et al., 2007). In conclusion, some of the trachybasaltic magmas must undergo extensive isobaric crystallization (from 66% to 85%) to produce the relatively H_2O-rich NYT-like magmas. These magmas can migrate to a shallower level, triggering further exsolution of fluids and crystallization of sanidine. In agreement with our data and modeling, the NYT is the most explosive eruption (VEI 6) to occur in this area in the last 23.6 ka. This interpretation is consistent with Mastrolorenzo and Pappalardo (2006), who showed that explosivity of eruptions at CF is mostly controlled by initial conditions in the magma chamber, including the volatile content, temperature and pressure. If the magnitude of the eruption is mainly driven by the pre-eruptive H_2O content of melts (Edmonds and Wallace, 2017; Webster et al., 2001), then extensive crystallization of a trachybasaltic magma occurring at relatively high pressure (relatively great depth) sets the stage for a later possible highly explosive eruption, because it will generate a more evolved, H_2O-rich melt.

7. Concluding remarks

Major element compositions of MI trapped in the most abundant crystal phases (olivine, clinopyroxene, sanidine and plagioclase) precipitating from CF and IP magmas younger than 23.6 ka, both from this study and from the literature, show compositional trends that to a large extent overlap with bulk rock compositions. Some MI show anomalous compositions, especially for Al_2O_3, P_2O_5, FeO, MgO, CaO and TiO_2. These anomalous MI can be explained through various processes, including grain scale dissolution–reaction–mixing (Danyushevsky et al.,
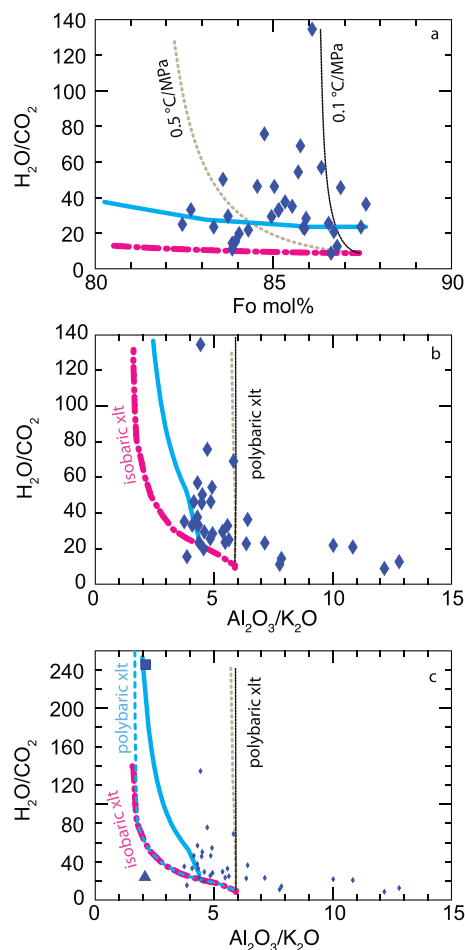

Fig. 17. Volatile compositions of bubble-free MI compared to a) host compositions, and b) and c) major element compositions of the MI. Symbols the same as in Fig. 3, whereas trend line styles are the same as in Figs. 6 and 7. a) mol% Fo vs. H_2O/CO_2; b) Al_2O_3/K_2O vs. H_2O/CO_2 for mafic bubble-free MI; c) Al_2O_3/K_2O vs. H_2O/CO_2 trachytic and mafic bubble-free MI.

2004), Fe loss and/or gain, and boundary layer processes. Anomalous MI exhibit volatile concentrations that likely deviate significantly from actual melt compositions. For these reasons, we suggest that all MI analyzed for volatile concentrations must also be analyzed for major elements to test for the representativeness of the trapped melt. In this study, all anomalous MI data were filtered from the dataset before interpreting volatile concentrations recorded by MI.

Another potential concern associated with determining the pre-eruptive volatile content of the original trapped melt based on MI analysis is the presence of a vapor bubble. Only a portion of the total volatile budget in the original trapped melt will be accounted for if the volatile content of the bubble is not considered (Esposito et al., 2016 and references therein), and interpretation of volatile contents based only on analysis of the glass phase of bubble-bearing MI may lead to erroneous conclusions. Thus, volatile concentrations of "normal" and bubble-free MI are shown to be more reliable monitors of volatile evolution during differentiation from trachybasaltic to trachyte magmas younger than 23.6 ka associated with the CF and IP eruptions. Major and trace element systematics, volatile contents, and petrological modeling based on "normal" and bubble-free MI suggest that trachybasaltic magmas ascended through the crust from depths of at least ~7.5 km (~200 MPa). This depth is consistent with geophysical data reported by Zollo et al. (2008), who suggest a 1–2 km thick layer of partially molten rocks at a depth of 8 km. At ≥7.5 km depth, trachybasalts can ascend through the crust to shallower levels while

Table 4
MI and olivine host descriptions based on Melt-1 and Mixed grouping.

MI-ID	Host zonation					MI position within the host				
	None	Normal	Reversed	Oscillatory	Patchy	Core position	Rim position	Intermediate	Embayement	
RESC4-O3-MA				x				x	x	Mixed MI
RESC4-O4-MA				x			x		x	
RESC4-O6-MA		x						x		
RESC4-O7-MA-av	x							x	x	
RESC5-O1-MA-av	x						x			
RESC5-O21-MA-av				x			x		x	
RESC5-O21-ME				x			x		x	
RESC5-O25-MB				x			x		x	
RESC5-O26-MA				x				x	x	
RESC5-O5-MA			x					x	x	
RESC5-O6-MA	x						x		x	
RESC2-O52.MIA	x					x				Melt-1 MI
RESC3-O10-MA	x							x	x	
RESC3-O10-MB	x							x	x	
RESC3-O16-MA				x				x		
RESC3-O18-MA	x							x	x	
RESC3-O23-MA					x			x	x	
RESC3-O26-MA				x		x			x	
RESC3-O27-MA	x					x			x	
RESC3-O27-MB	x					x			x	
RESC3-O29-MA		x				x			x	
RESC3-O3-MA		x				x			x	
RESC3-O6-MA		x						x		
RESC3-O7-MA				x		x			x	
RESC3-O9-MA	x					x				
RESC4-O10-MA-av				x				x	x	
RESC4-O11-MA-av		x				x			x	
RESC4-O14-MA				x		x				
RESC4-O14-MC				x			x			
RESC4-O15-MA				x			x			
RESC4-O5-MA	x					x				
RESC4-O9-MA				x				x	x	
RESC5-O10-MA	x							x		
RESC5-O10-MD	x							x		
RESC5-O15-MA	x					x				
RESC5-O18-MA	x					x				
RESC5-O22-MA	x							x		
RESC5-O27-MB	na	na	na	na	na	x			x	

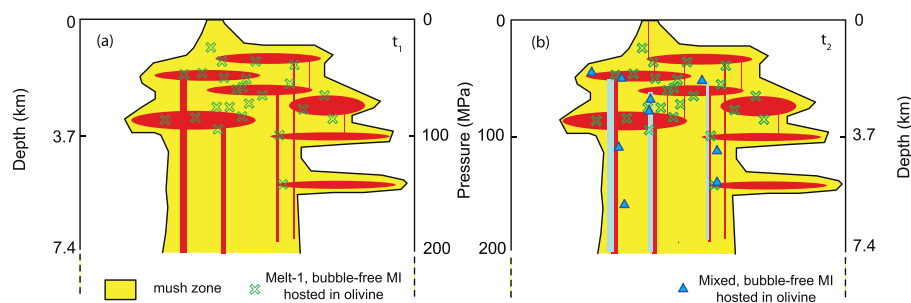| Summary	zoned	unzoned	total	zoned%	unzoned%	core	intermediate	rim	total	rim%	core%
Mixed-MI	8	3	11	73	27	0	5	6	11	55	0
Melt-1 MI	13	13	26	50	50	14	2	11	27	41	52

Fig. 18. Simplified temporal evolution model for the Solchiaro eruption based on bubble-free MI hosted in olivine. The results are based on the column-mush model of Marsh (1996), in which the plumbing system is represented by numerous sill-like pools of magma variably connected by dikes. The different thicknesses of these sills and dikes can result in different P-T histories for the same type of melt. This is consistent with MI data that show no correlation between Fo mol% of the host and the extrapolated depths of formation. Calculated pressures of formation of MI and interpreted depths were reported by Esposito et al. (2011) based on the solubility model of Papale et al. (2006). (t$_1$) the magma evolves mainly by fractional crystallization of magmas in separate pools. (t$_2$) recharge of new magma that mixes with the pre-existing magmas leading to the Solchiaro eruption.

undergoing minimal crystallization under volatile saturation and pond to feed eruptions associated with relatively less-differentiated magmas, as in the case of the Solchiaro eruption (23.6 ka ago). At 7.5 km depth, the same poorly differentiated magmas undergo extensive isobaric crystallization to form trachytic-phonolitic magmas feeding eruptions such as the NYT (15 ka ago; Deino et al., 2004). During extensive isobaric crystallization, the magma could also assimilate 1%–2% crustal material (D'Antonio et al., 2007). Isobaric crystallization at ~7 km depth of the parental melt of the Fondo Riccio eruption at CF was also suggested by Cannatelli (2012) based on MI data and MELTS simulations. Extensive crystallization under volatile-saturated conditions increases the H$_2$O content of the magma and, in turn, increases the likelihood of generating a high magnitude (explosive) eruption, as occurred for the NYT eruption (40 km^3 DRE). In another case, the

trachybasaltic magmas may evolve to trachytic-phonolitic magmas at shallower levels and H_2O enrichment of the magma during isobaric crystallization would be limited.

Bubble-free MI representative of magmas associated with the Solchiaro eruption suggest that mixing between trachybasaltic magmas and basaltic magmas occurred beneath the IP. One group of bubble-free MI is associated with simple polybaric crystallization from a trachy-basaltic primitive melt, while another group of MI define a trend consistent with mixing between the trachybasaltic primitive magma and another basaltic primitive magma. The primitive basaltic magma shows a more moderate enrichment of elements compatible with a slab-derived fluid. The mixing occurred at depths of at least ~6 km after simple crystallization of the trachybasaltic magma and likely did not affect the shallowest levels of the plumbing system.

Finally, even though interpretations based on volatile concentrations from MI may be sometimes problematic, they provide the only direct means to investigate magmatic processes such as degassing during magma ascent and crystallization. In this study, we show that MI provide more reliable information concerning the pre-eruptive volatile contents of magmas if the following steps are taken:

1- MI showing anomalous major element compositions relative to the bulk rock trends are omitted from the interpretation.
2- A detailed petrographic description of MI (e.g., size, shape, distance from the host edge, presence of the bubble, presence of magnetite dust etc.) should be performed to rule out processes affecting the reliability of MI such as boundary layer effects, and diffusive loss or gain of volatiles after trapping.
3- Bubbles of bubble-bearing MI should be analyzed to check for the presence of volatiles. Recent studies show that up to 90% of the total original CO_2 content of an MI could be stored in the vapor bubble (Aster et al., 2016; Hartley et al., 2014; Moore et al., 2015). For certain conditions, significant amounts of H_2O and S could also be lost into the bubble of MI (Esposito et al., 2016).
4- Temporal relationships between MI studied and host phase should be assessed to test various interpretations defined by volatile trends. When available, groups of MI trapped at the same time (Melt Inclusion Assemblages) should be examined to test the reliability of the data recorded by MI. Cathodoluminescence mapping of quartz phenocrysts (Peppard et al., 2001) or phosphorous maps in olivine (Esposito et al., 2015) can be used to assess relative time of MI formation. Time constraints on MI formation can be used to support or rule out interpretations on volatile trends recorded by MI.

Acknowledgments

References

Acocella, V., Funiciello, R., 1999. The interaction between regional and local tectonics during resurgent doming: the case of the island of Ischia, Italy. J. Volcanol. Geotherm. Res. 88 (1), 109–123.

Acocella, V., Salvini, F., Funiciello, R., Faccenna, C., 1999. The role of transfer structures on volcanic activity at Campi Flegrei (southern Italy). J. Volcanol. Geotherm. Res. 91 (2), 123–139.

Albarède, F., 1996. Introduction to Geochemical Modeling. Cambridge University Press.

Albini, A., Cristofolini, R., Di Girolamo, P., Nardi, G., Rolandi, G., Stanzione, D., 1977. Rare earth element and thorium distribution in volcanic rocks of the potassic kindred from Procida Island and the Phlegrean Fields, southern Italy. Atti Accad. Naz. Lincei, Classe di Scienze Fisiche Matematiche e Naturali, Rendiconti 63 (5), 416–429.

Alessio, M., Bella, F., Improta, S., Belluomini, G., Cortesi, C., Turi, B., 1971. University of Rome carbon-14 dates IX. Radiocarbon 13 (2), 395–411.

Alessio, M., Allegri, L., Azzi, C., Calderoni, G., Cortesi, C., Improta, S., Petrone, V., 1989. ^{14}C tephrochronology with different fractions of Paleosol humic matter at Procida Island, Italy. Radiocarbon 31, 664–671.

Arienzo, I., Moretti, R., Civetta, L., Orsi, G., Papale, P., 2010. The feeding system of Agnano–Monte Spina eruption (Campi Flegrei, Italy): dragging the past into present activity and future scenarios. Chem. Geol. 270 (1–4), 135–147.

Arienzo, I., Mazzeo, F., Moretti, R., Cavallo, A., D'Antonio, M., 2016. Open-system magma evolution and fluid transfer at Campi Flegrei caldera (southern Italy) during the past 5ka as revealed by geochemical and isotopic data: the example of the Nisida eruption. Chem. Geol. 427, 109–124.

Aster, E.M., Wallace, P.J., Moore, L.R., Watkins, J., Gazel, E., Bodnar, R.J., 2016. Reconstructing CO_2 concentrations in basaltic melt inclusions using Raman analysis of vapor bubbles. J. Volcanol. Geotherm. Res. 323, 148–162.

Baker, D., 2008. The fidelity of melt inclusions as records of melt composition. Contrib. Mineral. Petrol. 156 (3), 377–395.

Barbieri, M., Di Girolamo, P., Locardi, E., Lombardi, G., Stanzione, D., 1979. Petrology of the calc-alkaline volcanics of the Parete 2 well (Campania, Italy). Periodico di Mineralogia 48, 53–74.

Beccaluva, L., Di Girolamo, P., Serri, G., 1991. Petrogenesis and tectonic setting of the roman Volcanic Province, Italy. Lithos 26, 191–221.

Blundy, J., Cashman, K., 2008. Petrologic reconstruction of magmatic system variables and processes. Rev. Mineral. Geochem. 69 (1), 179–239.

Bodnar, R.J., Student, J.J., 2006. Melt inclusions in plutonic rocks: petrography and microthermometry. In: Webster, J.D. (Ed.), Melt Inclusions in Plutonic Rocks. Mineralogical Association of Canada, Montreal, Quebec, Canada, pp. 1–25.

Bodnar, R.J., Cannatelli, C., De Vivo, B., Lima, A., Belkin, H.E., Milia, A., 2007. Quantitative model for magma degassing and ground deformation (bradyseism) at Campi Flegrei, Italy; implications for future eruptions. Geology 35 (9), 791–794.

Brocchini, D., Principe, C., Castradori, D., Laurenzi, M.A., Gorla, L., 2001. Quaternary evolution of the southern sector of the Campanian plain and early Somma-Vesuvius activity: insights from the Trecase 1 well. Mineral. Petrol. 73 (1–3), 67–91.

Bucholz, C.E., Gaetani, G.A., Behn, M.D., Shimizu, N., 2013. Post-entrapment modification of volatiles and oxygen fugacity in olivine-hosted melt inclusions. Earth Planet. Sci. Lett. 374 (0), 145–155.

Cannatelli, C., 2012. Understanding magma evolution at Campi Flegrei (Campania, Italy) volcanic complex using melt inclusions and phase equilibria. Mineral. Petrol. 104 (1–2), 29–42.

Cannatelli, C., Lima, A., Bodnar, R.J., De Vivo, B., Webster, J.D., Fedele, L., 2007. Geochemistry of melt inclusions from the Fondo Riccio and Minopoli 1 eruptions at Campi Flegrei (Italy). Chem. Geol. 237, 418–432.

Cannatelli, C., Doherty, A., Esposito, R., Lima, A., De Vivo, B., 2016. Understanding a volcano through a droplet: a melt inclusion approach. J. Geochem. Explor. 171, 4–19.

Capaldi, G., Gasparini, P., Moauro, A., Salvia, E., Travaglione, O., 1972. Rare earth abundances in the alkaline volcanic rocks from Campania, South Italy. Earth Planet. Sci. Lett. 17, 247–257.

Cashman, K.V., Sparks, R.S.J., Blundy, J.D., 2017. Vertically extensive and unstable magmatic systems: a unified view of igneous processes. Science 355 (6331), eaag3055.

Cecchetti, A., Fulignati, P., Marianelli, P., Proto, N., Sbrana, A., 2001. The feeding system of Campi Flegrei. Insights from melt and fluid inclusions on Ignimbrite Campana, Solchiaro and Minopoli eruptions. In: GNV-INGV Meeting. Rome, Italy, pp. 190–191.

Cecchetti, A., Marianelli, P., Sbrana, A., 2003. L'eruzione di Astroni (caldera dei Campi Flegrei): dati preliminari dallo studio di inclusioni silicatiche. Atti Soc. Tosc. Sci. Nat., Mem. 108, 59–63.

Chiodini, G., Vandemeulebrouck, J., Caliro, S., D'Auria, L., De Martino, P., Mangiacapra, A., Petrillo, Z., 2015. Evidence of thermal-driven processes triggering the 2005–2014 unrest at Campi Flegrei caldera. Earth Planet. Sci. Lett. 414, 58–67.

Cipriani, F., Marianelli, P., Sbrana, A., 2008. Study of a pyroclastic sequence of Solfatara volcano (Phlegrean Fields). Insights on volcanological and feeding system processes. Atti Soc. Tosc. Sci. Nat., Mem. 113, 39–48.

Civetta, L., Carluccio, E., Innocenti, F., Sbrana, A., Taddeucci, G., 1991. Magma chamber evolution under the Phlegraean fields during the last 10 ka; trace element and isotope data. Eur. J. Mineral. 3 (2), 415–428.

Civetta, L., Orsi, G., Pappalardo, L., Fisher, R.V., Heiken, G., Ort, M., 1997. Geochemical zoning, mingling, eruptive dynamics and depositional processes - the Campanian Ignimbrite, Campi Flegrei caldera, Italy. J. Volcanol. Geotherm. Res. 75 (3–4), 183–219.

Da Toledo, P., Giacomo, B., 1539. Ragionamento del terremoto, del Nvovo monte, del aprimento di terra in Pozvolo nel anno 1538 : e dela significatione d'essi. Giouanni Sulztbah alemano. Napoli).

D'Antonio, M., 2011. Lithology of the basement underlying the Campi Flegrei caldera: Volcanological and petrological constraints. J. Volcanol. Geotherm. Res. 200 (1–2), 91–98.

D'Antonio, M., Di Girolamo, P., 1994. Petrological and geochemical study of mafic shoshonitic volcanics from Procida-Vivara and Ventotene Islands (Campanian

Region, South Italy). Acta Vulcanol 5, 69–80.

D'Antonio, M., Civetta, L., Di Girolamo, P., 1999a. Mantle source heterogeneity in the Campanian region (South Italy) as inferred from geochemical and isotopic features of mafic volcanic rocks with shoshonitic affinity. Mineral. Petrol. 67, 163–192.

D'Antonio, M., Civetta, L., Orsi, G., Pappalardo, L., Piochi, M., Carandente, A., De Vita, S., Di Vito, M.A., Isaia, R., 1999b. The present state of the magmatic system of the Campi Flegrei caldera based on a reconstruction of its behavior in the past 12 ka. J. Volcanol. Geotherm. Res. 91 (2–4), 247–268.

D'Antonio, M., Tonarini, S., Arienzo, I., Civetta, L., Di Renzo, V., 2007. Components and Processes in the Magma Genesis of the Phlegrean Volcanic District, Southern Italy. Vol. 418. Geological Society of America Special Papers, pp. 203–220.

Danyushevsky, L.V., Plechov, P., 2011. Petrolog3: integrated software for modeling crystallization processes. Geochem. Geophys. Geosyst. 12 (7), Q07021.

Danyushevsky, L.V., Della-Pasqua, F.N., Sokolov, S., 2000. Re-equilibration of melt inclusions trapped by magnesian olivine phenocrysts from subduction-related magmas: petrological implications. Contrib. Mineral. Petrol. 138 (1), 68–83.

Danyushevsky, L.V., McNeill, A.W., Sobolev, A.V., 2002a. Experimental and petrological studies of melt inclusions in phenocrysts from mantle-derived magmas: an overview of techniques, advantages and complications. Chem. Geol. 183 (1–4), 5–24.

Danyushevsky, L.V., Sokolov, S., Falloon, T.J., 2002b. Melt inclusions in olivine phenocrysts; using diffusive re-equilibration to determine the cooling history of a crystal, with implications for the origin of olivine-phyric volcanic rocks. J. Petrol. 43 (9), 1651–1671.

Danyushevsky, L.V., Leslie, R.A.J., Crawford, A.J., Durance, P., 2004. Melt inclusions in primitive olivine phenocrysts; the role of localized reaction processes in the origin of anomalous compositions. J. Petrol. 45 (12), 2531–2553.

De Astis, G., Pappalardo, L., Piochi, M., 2004. Procida volcanic history: new insights in the evolution of the Phlegraean Volcanic District (Campania, Italy). Bull. Volcanol. 66, 622–641.

De Natale, G., Troise, C., Mark, D., Mormone, A., Piochi, M., Di Vito, M.A., Isaia, R., Carlino, S., Barra, D., Somma, R., 2016. The Campi Flegrei Deep Drilling Project (CFDDP): new insight on caldera structure, evolution and hazard implications for the Naples area (southern Italy). Geochem. Geophys. Geosyst. 17 (12), 4836–4847.

de Vita, S., Orsi, G., Civetta, L., Carandente, A., D'Antonio, M., Deino, A., di Cesare, T., Di Vito, M.A., Fisher, R.V., Isaia, R., Marotta, E., Necco, A., Ort, M., Pappalardo, L., Piochi, M., Southon, J., 1999. The Agnano–Monte Spina eruption (4100 years BP) in the restless Campi Flegrei caldera (Italy). J. Volcanol. Geotherm. Res. 91, 269–301.

De Vivo, B., Rolandi, G., Gans, P.B., Calvert, A., Bohrson, W.A., Spera, F.J., Belkin, H.E., 2001. New constraints on the pyroclastic eruptive history of the Campanian volcanic plain (Italy). Mineral. Petrol. 73 (1–3), 47–65.

De Vivo, B., Petrosino, P., Lima, A., Rolandi, G., Belkin, H., 2010. Research progress in volcanology in the Neapolitan area, southern Italy: a review and some alternative views. Mineral. Petrol. 99 (1), 1–28.

Deegan, F., Troll, V., Freda, C., Misiti, V., Chadwick, J.P., McLeod, C., Davidson, J.P., 2010. Magma–carbonate interaction processes and associated CO2 release at Merapi Volcano, Indonesia: insights from experimental petrology. J. Petrol. 51 (5), 1027–1051.

Deino, A.L., Orsi, G., De Vita, S., Piochi, M., 2004. The age of the Neapolitan yellow tuff caldera-forming eruption (Campi Flegrei Caldera, Italy) assessed by ^{40}Ar/^{39}Ar dating method. J. Volcanol. Geotherm. Res. 133, 157–170.

Di Girolamo, P., Stanzione, D., 1973. Lineamenti geologici e petrologici dell'isola di Procida. In: Rendiconti della Societa Italiana di Mineralogia e Petrologia. Vol. 29. pp. 81–125.

Di Girolamo, P., Ghiara, M.R., Lirer Munno, R., Rolandi, G., Stanzione, D., 1984. Vulcanologia e petrologia dei Campi Flegreei. Volcanology and petrology of Phlegraean Fields. Bollettino della Società Geologica Italiana 103, 349–413.

Di Renzo, V., Arienzo, I., Civetta, L., D'Antonio, M., Tonarini, S., Di Vito, M.A., Orsi, G., 2011. The magmatic feeding system of the Campi Flegrei caldera: architecture and temporal evolution. Chem. Geol. 281 (3–4), 227–241.

Di Vito, M.A., Isaia, R., Orsi, G., Southon, J., De Vita, S., D'Antonio, M., Pappalardo, L., Piochi, M., 1999. Volcanism and deformation since 12,000 years at the Campi Flegrei Caldera (Italy). J. Volcanol. Geotherm. Res. 91 (2–4), 221–246.

Di Vito, M.A., Arienzo, I., Braia, G., Civetta, L., D'Antonio, M., Di Renzo, V., Orsi, G., 2011. The Averno 2 fissure eruption: a recent small-size explosive event at the Campi Flegrei Caldera (Italy). Bull. Volcanol. 73, 295–320.

Edmonds, M., Wallace, P.J., 2017. Volatiles and exsolved vapor in volcanic systems. Elements 13 (1), 29–34.

Esposito, R., Bodnar, R.J., Danyushevsky, L., De Vivo, B., Fedele, L., Hunter, J., Lima, A., Shimizu, N., 2011. Volatile evolution of magma associated with the Solchiaro eruption in the Phlegrean Volcanic District (Italy). J. Petrol. 52 (12), 2431–2460.

Esposito, R., Klebesz, R., Bartoli, O., Klyukin, Y.I., Moncada, D., Doherty, A.L., Bodnar, R.J., 2012. Application of the Linkam TS1400XY heating stage to melt inclusion studies. Cent. Eur. J. Geosci. 4 (2), 208–218.

Esposito, R., Hunter, J., Schiffbauer, J., Shimizu, N., Bodnar, R.J., 2014. An assessment of the reliability of melt inclusions as recorders of the pre-eruptive volatile content of magmas. Am. Mineral. 99 (5–6), 976–998.

Esposito, R., Badescu, K., Boyce, J.W., Manning, C.E., 2015. Assessing the Origin of Olivines based on relative age of melt inclusions. In: American Geophysical Union, Fall Meeting 2015, abstract volume: #V51D-3068.

Esposito, R., Lamadrid, H.M., Redi, D., Steele-MacInnis, M., Bodnar, R.J., Manning, C.E., De Vivo, B., Cannatelli, C., Lima, A., 2016. Detection of liquid H2O in vapor bubbles in reheated melt inclusions: implications for magmatic fluid composition and volatile budgets of magmas? Am. Mineral. 101 (7), 1691–1695.

Fanara, S., Botcharnikov, R.E., Palladino, D.M., Adams, F., Buddensieck, J., Mulch, A., Behrens, H., 2015. Volatiles in magmas related to the Campanian Ignimbrite eruption: experiments vs. natural findings. Am. Mineral. 100 (10), 2284–2297.

Faure, F., Schiano, P., 2005. Experimental investigation of equilibration conditions during forsterite growth and melt inclusion formation. Earth Planet. Sci. Lett. 236 (3–4), 882–898.

Fedele, F.G., Giaccio, B., Isaia, R., Orsi, G., Carroll, M., Scaillet, B., 2007. The Campanian Ignimbrite factor: towards a reappraisal of the Middle to Upper Palaeolithic 'transition'. In: Grattan, J., Torrence, R. (Eds.), Living Under the Shadow: Cultural Impacts of Volcanic Eruptions. One World Archeology. Left Coast Press, Walnut Creek (CA), pp. 19–41.

Fedele, L., Insinga, D., Calvert, A., Morra, V., Perrotta, A., Scarpati, C., 2011. ^{40}Ar/^{39}Ar dating of tuff vents in the Campi Flegrei caldera (southern Italy): toward a new chronostratigraphic reconstruction of the Holocene volcanic activity. Bull. Volcanol. 73 (9), 1323–1336.

Forni, F., Petricca, E., Bachmann, O., Mollo, S., De Astis, G., Piochi, M., 2018. The role of magma mixing/mingling and cumulate melting in the Neapolitan Yellow Tuff caldera-forming eruption (Campi Flegrei, Southern Italy). Contrib. Mineral. Petrol. 173 (6), 45.

Fourmentraux, C., Metrich, N., Bertagnini, A., Rosi, M., 2012. Crystal fractionation, magma step ascent, and syn-eruptive mingling; the Averno 2 eruption (Phlegraean Fields, Italy). Contrib. Mineral. Petrol. 163 (6), 1121–1137.

Fowler, S.J., Spera, F.J., Bohrson, W.A., Belkin, H.E., De Vivo, B., 2007. Phase equilibria constraints on the chemical and physical evolution of the Campanian Ignimbrite. J. Petrol. 48 (3), 459–493.

Gebauer, S.K., Schmitt, A.K., Pappalardo, L., Stockli, D.F., Lovera, O.M., 2014. Crystallization and eruption ages of Breccia Museo (Campi Flegrei Caldera, Italy) plutonic clasts and their relation to the Campanian Ignimbrite. Contrib. Mineral. Petrol. 167 (1), 953.

Ghiara, M.R., Lirer, L., Munno, R., 1979. Mineralogy and geochemistry of the "low-potassium series" of the Campania Volcanics (South Italy). Chem. Geol. 26, 29–49.

Ghiorso, M.S., Gualda, G.A., 2015. An H2O–CO2 mixed fluid saturation model compatible with rhyolite-MELTS. Contrib. Mineral. Petrol. 169 (6), 1–30.

Gilg, H., Lima, A., Somma, R., Belkin, H., De Vivo, B., Ayuso, R., 2001. Isotope geochemistry and fluid inclusion study of skarns from Vesuvius. Mineral. Petrol. 73 (1–3), 145–176.

Gillot, P.Y., Chiesa, S., Pasquare, G., Vezzoli, L., 1982. < 33,000-yr K-Ar dating of the volcano-tectonic horst of the Isle of Ischia, Gulf of Naples. Nature 299 (5880), 242–245.

Hartley, M.E., Maclennan, J., Edmonds, M., Thordarson, T., 2014. Reconstructing the deep CO2 degassing behaviour of large basaltic fissure eruptions. Earth Planet. Sci. Lett. 393 (0), 120–131.

Hauri, E., Wang, J., Dixon, J.E., King, P.L., Mandeville, C., Newman, S., 2002. SIMS analysis of volatiles in silicate glasses: 1. Calibration, matrix effects and comparisons with FTIR. Chem. Geol. 183 (1), 99–114.

Hayward, C., 2012. High spatial resolution electron probe microanalysis of tephras and melt inclusions without beam-induced chemical modification. The Holocene 22 (1), 119–125.

Helo, C., Longpre, M.A., Shimizu, N., Clague, D.A., Stix, J., 2011. Explosive eruptions at mid-ocean ridges driven by CO2-rich magmas. Nat. Geosci. 4 (4), 260–263.

Humphreys, M.C.S., Blundy, J.D., Sparks, R.S.J., 2008a. Shallow-level decompression crystallisation and deep magma supply at Shiveluch Volcano. Contrib. Mineral. Petrol. 155 (1), 45–61.

Humphreys, M.C.S., Menand, T., Blundy, J.D., Klimm, K., 2008b. Magma ascent rates in explosive eruptions: constraints from H2O diffusion in melt inclusions. Earth Planet. Sci. Lett. 270 (1–2), 25–40.

Ippolito, F., D'Argenio, B., Pescatore, T., Scandone, P., 1975. Structural-stratigraphic units and tectonic framework of the southern Apennines. In: Squyres, C.H. (Ed.), Geology of Italy. Earth Sci. Soc. Libyan Arab Rep., Tripoli, Libya, pp. 1–11.

Isaia, R., Marianelli, P., Sbrana, A., 2009. Caldera unrest prior to intense volcanism in Campi Flegrei (Italy) at 4.0 ka BP: implications for caldera dynamics and future eruptive scenarios. Geophys. Res. Lett. 36 (21).

Kent, A.J.R., 2008. Melt inclusions in basaltic and related volcanic rocks. In: Putirka, K.D., Tepley IIIF.J. (Eds.), Minerals, Inclusions and Volcanic Processes. The Mineralogical Society of America, pp. 273–331.

Klébesz, R., Esposito, R., De Vivo, B., Bodnar, R.J., 2015. Constraints on the origin of sub-effusive nodules from the Sarno (Pomici di base) eruption of Mt. Somma-Vesuvius (Italy) based on compositions of silicate-melt inclusions and clinopyroxene. Am. Mineral. 100 (4), 760–773.

Kress, V.C., Ghiorso, M.S., 2004. Thermodynamic modeling of post-entrapment crystallization in igneous phases. J. Volcanol. Geotherm. Res. 137 (4), 247–260.

Lima, A., Danyushevsky, L.V., De Vivo, B., Fedele, L., 2003. A model for the evolution of the Mt. Somma-Vesuvius magmatic system based on fluid and melt inclusion investigations. Develop. Volcanol. 5, 227–249.

Lima, A., De Vivo, B., Spera, F.J., Bodnar, R.J., Milia, A., Nunziata, C., Belkin, H.E., Cannatelli, C., 2009. Thermodynamic model for uplift and deflation episodes (bradyseism) associated with magmatic-hydrothermal activity at the Campi Flegrei (Italy). Earth Sci. Rev. 97 (1–4), 44–58.

Lima, A., Esposito, R., De Vivo, B., 2017. Fluid and melt inclusions from subvolcanic to surface environment in the Campi Flegrei (Napoli, Italy) active volcanic system. J. Geol. Soc. India 90 (5), 515–523.

Lirer, L., Rolandi, G., Rubin, M., 1991. ^{14}C age of the "museum breccia" (Campi Flegrei) and its relevance for the origin of the Campanian Ignimbrite. J. Volcanol. Geotherm. Res. 48 (1–2), 223–227.

Lirer, L., Petrosino, P., Alberico, I., Armiero, V., 2011. Cartografia. In: Lirer, L. (Ed.), I Campi Flegrei, storia di un campo vulcanico. Quaderni dell'accademia pontiniana, Napoli, pp. 7–77.

Maclennan, J., 2017. Bubble formation and decrepitation control the CO2 content of olivine-hosted melt inclusions. Geochem. Geophys. Geosyst. 18 (2), 597–616.

Mangiacapra, A., Moretti, R., Rutherford, M., Civetta, L., Orsi, G., Papale, P., 2008. The deep magmatic system of the Campi Flegrei caldera (Italy). Geophys. Res. Lett. 35 (21) (L21304).

Marianelli, P., Sbrana, A., Proto, M., 2006. Magma chamber of the Campi Flegrei supervolcano at the time of eruption of the Campanian Ignimbrite. Geology 34 (11), 937–940.

Marsh, B.D., 1996. Solidification fronts and magmatic evolution. Mineral. Mag. 60 (1), 5–40.

Mastrolorenzo, G., Pappalardo, L., 2006. Magma degassing and crystallization processes during eruptions of high-risk Neapolitan-volcanoes: evidence of common equilibrium rising processes in alkaline magmas. Earth Planet. Sci. Lett. 250, 164–181.

Mazzeo, F., D'Antonio, M., Arienzo, I., Aulinas, M., Di Renzo, V., Gimeno, D., 2014. Subduction-related enrichment of the Neapolitan volcanoes (southern Italy) mantle source: new constraints on the characteristics of the slab-derived components. Chem. Geol. 386, 165–183.

Melluso, L., De'Gennaro, R., Fedele, L., Franciosi, L., Morra, V., 2012. Evidence of crystallization in residual, Cl–F-rich, agpaitic, trachyphonolitic magmas and primitive Mg-rich basalt–trachyphonolite interaction in the lava domes of the Phlegrean Fields (Italy). Geol. Mag. 149 (3), 532.

Metrich, N., Wallace, P.J., 2008. Volatile abundances in basaltic magmas and their degassing paths tracked by melt inclusions. Rev. Mineral. Geochem. 69 (1), 363–402.

Milia, A., 2010. The stratigraphic signature of volcanism off Campi Flegrei (Bay of Naples, Italy). In: Groppelli, G., Viereck-Goette, L. (Eds.), Stratigraphy and geology of volcanic areas. The Geological Society of America, Buolder, Colorado, pp. 155–170.

Mironov, N., Portnyagin, M.V., 2011. H_2O and CO_2 in parental magmas of Kliuchevskoi volcano inferred from study of melt and fluid inclusions in olivine. Russ. Geol. Geophys. 52 (11), 1353–1367.

Mironov, N., Portnyagin, M., Botcharnikov, R., Gurenko, A., Hoernle, K., Holtz, F., 2015. Quantification of the CO_2 budget and $H_2O–CO_2$ systematics in subduction-zone magmas through the experimental hydration of melt inclusions in olivine at high H_2O pressure. Earth Planet. Sci. Lett. 425, 1–11.

Moore, L.R., Gazel, E., Tuohy, R., Lloyd, A.S., Esposito, R., Steele-MacInnis, M., Hauri, E.H., Wallace, P.J., Plank, T., Bodnar, R.J., 2015. Bubbles matter: an assessment of the contribution of vapor bubbles to melt inclusion volatile budgets. Am. Mineral. 100 (4), 806–823.

Morabito, S., Petrosino, P., Milia, A., Sprovieri, M., Tamburrino, S., 2014. A multi-disciplinary approach for reconstructing the stratigraphic framework of the last 40ka in a bathyal area of the eastern Tyrrhenian Sea. Glob. Planet. Chang. 123, 121–138.

Moretti, R., Arienzo, I., Orsi, G., Civetta, L., D'Antonio, M., 2013. The deep plumbing system of ischia: a physico-chemical window on the fluid-saturated and CO_2-sustained Neapolitan volcanism (southern Italy). J. Petrol. 54 (5), 951–984.

Moretti, R., De Natale, G., Troise, C., 2017. A geochemical and geophysical reappraisal to the significance of the recent unrest at Campi Flegrei caldera (southern Italy). Geochem. Geophys. Geosyst. 18 (3), 1244–1269.

Morgan, G.B., London, D., 2005. Effect of current density on the electron microprobe analysis of alkali aluminosilicate glasses. Am. Mineral. 90 (7), 1131–1138.

Mormone, A., Piochi, M., Bellatreccia, F., De Astis, G., Moretti, R., Della Ventura, G., Cavallo, A., Mangiacapra, A., 2011. A CO_2-rich magma source beneath the Phlegraean Volcanic District (southern Italy): evidence from a melt inclusion study. Chem. Geol. 287 (1–2), 66–80.

Moussallam, Y., Oppenheimer, C., Scaillet, B., Gaillard, F., Kyle, P., Peters, N., Hartley, M., Berlo, K., Donovan, A., 2014. Tracking the changing oxidation state of Erebus magmas, from mantle to surface, driven by magma ascent and degassing. Earth Planet. Sci. Lett. 393, 200–209.

Nakamura, M., Shimakita, S., 1998. Dissolution origin and syn-entrapment compositional change of melt inclusion in plagioclase. Earth Planet. Sci. Lett. 161 (1), 119–133.

Norman, M.D., Garcia, M.O., Kamenetsky, V.S., Nielsen, R.L., 2002. Olivine-hosted melt inclusions in Hawaiian picrites: equilibration, melting, and plume source characteristics. Chem. Geol. 183 (1–4), 143–168.

Orsi, G., D'Antonio, M., de Vita, S., Gallo, G., 1992. The Neapolitan yellow tuff, a large-magnitude trachytic phreatoplinian eruption; eruptive dynamics, magma withdrawal and caldera collapse. J. Volcanol. Geotherm. Res. 53 (1–4), 275–287.

Orsi, G., Civetta, L., Dantonio, M., Digirolamo, P., Piochi, M., 1995. Step-filling and development of a 3-layer magma chamber - the Neapolitan-yellow-tuff case-history. J. Volcanol. Geotherm. Res. 67 (4), 291–312.

Orsi, G., de Vita, S., di Vito, M., 1996. The restless, resurgent Campi Flegrei nested caldera (Italy); constraints on its evolution and configuration. J. Volcanol. Geotherm. Res. 74 (3–4), 179–214.

Orsi, G., Civetta, L., Del Gaudio, C., De Vita, S., Di Vito, M.A., Isaia, R., Petrazzuoli, S.M., Ricciardi, G.P., Ricco, C., 1999. Short-term ground deformations and seismicity in the resurgent Campi Flegrei Caldera (Italy); an example of active block-resurgence in a densely populated area. J. Volcanol. Geotherm. Res. 91 (2–4), 415–451.

Papale, P., Moretti, R., Barbato, D., 2006. The compositional dependence of the saturation surface of $H_2O + CO_2$ fluids in silicate melts. Chem. Geol. 229 (1–3), 78–95.

Pappalardo, L., Civetta, L., D'Antonio, M., Deino, A., Di Vito, M.A., Orsi, G., Carandente, A., De Vita, S., Isaia, R., Piochi, M., 1999. Chemical and Sr-isotopical evolution of the Phlegraean magmatic system before the Campanian Ignimbrite and the Neapolitan yellow tuff eruptions. J. Volcanol. Geotherm. Res. 91 (2–4), 141–166.

Pappalardo, L., Piochi, M., D'Antonio, M., Civetta, L., Petrini, R., 2002. Evidence for multi-stage magmatic evolution during the past 60kyr at Campi Flegrei (Italy) Dduced from Sr, Nd and Pb isotope data. J. Petrol. 43 (8), 1415–1434.

Peccerillo, A., 1999. Multiple mantle metasomatism in central-southern Italy; geochemical effects, timing and geodynamic implications. Geology 27 (4), 315–318.

Peccerillo, A., 2017. The Campania Province, Cenozoic Volcanism in the Tyrrhenian Sea Region. In: Advances in Volcanology. Springer International Publishing AG, Cham, Switzerland, pp. 159–201.

Peppard, B.T., Steele, I.M., Davis, A.M., Wallace, P.J., Anderson, A.T., 2001. Zoned quartz phenocrysts from the rhyolitic bishop tuff. Am. Mineral. 86 (9), 1034–1052.

Perrotta, A., Scarpati, C., Luongo, G., Morra, V., 2006. The Campi Flegrei Caldera boundary in the City of Naples. In: De Vivo, B. (Ed.), Developments in Volcanology. Elsevier, pp. 85–96.

Pescatore, T., Rolandi, G., 1981. Osservazioni preliminari sulla stratigrafia dei depositi vulcanoclastici nel settore SW dei Campi Flegrei. Preliminary Observations of the Stratigraphy of Volcaniclastic Deposits of the South-West Sector of Phlagrean Fields. Vol. 100 (2). Bollettino della Società Geologica Italiana, pp. 233–254.

Piochi, M., Mastrolorenzo, G., Pappalardo, L., 2005. Magma ascent and eruptive processes from textural and compositional features of Monte Nuovo pyroclastic products, Campi Flegrei, Italy. Bull. Volcanol. 67 (7), 663–678.

Piochi, M., Polacci, M., De Astis, G., Zanetti, A., Mangiacapra, A., Vannucci, R., Giordano, D., 2008. Texture and composition of pumices and scoriae from the Campi Flegrei caldera (Italy): implications on the dynamics of explosive eruptions. Geochem. Geophys. Geosyst. 9 (3), Q03013.

Piochi, M., Kilburn, C.R.J., Vito, M.A., Mormone, A., Tramelli, A., Troise, C., Natale, G., 2013. The volcanic and geothermally active Campi Flegrei caldera: an integrated multidisciplinary image of its buried structure. Int. J. Earth Sci. 1–21.

Putirka, K.D., 2017. Down the crater: where magmas are stored and why they erupt. Elements 13 (1), 11–16.

Rhodes, J., 1981. Characteristics of primary Basaltic Magmas. In: Basaltic Volcanism Study Project: Basaltic Volcanism on the Terrestrial Planets. Pergamon Press, New York, pp. 409–432.

Roach, A.L., 2005. The Evolution of Silicic Magmatism in the Post-Caldera Volcanism of the Phlegrean Fields, Italy. Doctoral Thesis. Brown University, Providence.

Roedder, E., 1979. Origin and significance of magmatic inclusions. Bull. Mineral. 102 (5–6), 487–510 Mineraux et Minerais.

Rolandi, G., Bellucci, F., Heizler, M.T., Belkin, H.E., De Vivo, B., 2003. Tectonic controls on the genesis of ignimbrites from the Campanian volcanic zone, southern Italy. Mineral. Petrol. 79 (1), 3–31.

Rosi, M., Sbrana, A., 1987. Campi flegrei. Quaderni de "La Ricerca Scientifica". 9. pp. 175.

Rosi, M., Sbrana, A., Vezzoli, L., 1988a. Correlazioni tefrostratigraphiche di alcuni livelli di Ischia, Procida e Campi Flegrei. Vol. 41. Memorie della Società Geologica Italiana, pp. 1015–1027.

Rosi, M., Sbrana, A., Vezzoli, L., 1988b. Stratigraphy of Procida and Vivara islands. Bollettino Nazionale Geofisica e Vulcanologia 4, 500–525.

Rowe, M.C., Nielsen, R.L., Kent, A.J.R., 2006. Anomalously high Fe contents in re-homogenized olivine-hosted melt inclusions from oxidized magmas. Am. Mineral. 91 (1), 82–91.

Scandone, R., 1997. Campi Flegrei. http://vulcan.fis.uniroma3.it/campi_flegrei/Campi_flegrei.html pp. Geologic Map of Campi Flegrei Modified after Di Vito et al. (1985).

Scandone, R., Bellucci, F., Lirer, L., Rolandi, G., 1991. The structure of the Campanian plain and the activity of the Neapolitan volcanoes (Italy). J. Volcanol. Geotherm. Res. 48 (1–2), 1–31.

Scandone, R., Giacomelli, L. and Fattori Speranza, F., 2006. The volcanological history of the volcanoes of Naples: a review. In: B. De Vivo (editor), Volcanism in the Campanian Plain Elsevier Sciences, pp. 1–26.

Scarpati, C., Cole, P., Perrotta, A., 1993. The Neapolitan yellow tuff - a large volume multiphase eruption from Campi Flegrei, southern Italy. Bull. Volcanol. 55, 343–356.

Self, S., 1976. The recent volcanology of Terceira, Azores. J. Geol. Soc. 132 (6), 645–666.

Shishkina, T., Botcharnikov, R., Holtz, F., Almeev, R., Portnyagin, M.V., 2010. Solubility of H_2O- and CO_2-bearing fluids in tholeiitic basalts at pressures up to 500 MPa. Chem. Geol. 277 (1), 115–125.

Signorelli, S., Vaggelli, G., Francalanci, L., Rosi, M., 1999. Origin of magmas feeding the Plinian phase of the Campanian Ignimbrite eruption, Phlegrean Fields (Italy); constraints based on matrix-glass and glass-inclusion compositions. J. Volcanol. Geotherm. Res. 91 (2–4), 199–220.

Smith, V., Isaia, R., Pearce, N., 2011. Tephrostratigraphy and glass compositions of post-15 kyr Campi Flegrei eruptions: implications for eruption history and chronostratigraphic markers. Quat. Sci. Rev. 30 (25), 3638–3660.

Sobolev, A.V., Danyushevsky, L.V., 1994. Petrology and geochemistry of Boninites from the north termination of the Tonga trench: constraints on the generation conditions of primary high-Ca Boninite Magmas. J. Petrol. 35 (5), 1183–1211.

Sobolev, A.V., Dmitriev, L.V., Barsukov, V.L., Nevsorov, V.N., Slutsky, A.B., 1980. The formation conditions of the high magnesium olivines from the monomineralic fraction of Luna 24 Regolith. In: Proceedings of the Lunar and Planetary Science Conference. Vol. 11. pp. 105–116.

Spera, F., 1980. Thermal evolution of plutons: a parameterized approach. Science 207 (4428), 299–301.

Steele-MacInnis, M.J., Esposito, R., Bodnar, R.J., 2011. Thermodynamic model for the effect of post-entrapment crystallization on the H_2O-CO_2 systematics of volatile saturated silicate melt inclusions. J. Petrol. 52 (12), 2461–2482.

Steele-MacInnis, M., Esposito, R., Moore, L.R., Hartley, M.E., 2017. Heterogeneously entrapped, vapor-rich melt inclusions record pre-eruptive magmatic volatile contents. Contrib. Mineral. Petrol. 172 (4), 18.

Stock, M.J., Humphreys, M.C., Smith, V.C., Isaia, R., Pyle, D.M., 2016. Late-stage volatile saturation as a potential trigger for explosive volcanic eruptions. Nat. Geosci. 9 (3), 249–254.

Student, J.J., Bodnar, R.J., 2004. Silicate melt inclusions in porphyry copper deposits; identification and homogenization behavior. In: Kontak, D.J., Anderson, A.J., Marshall, D.D. (Eds.), The Canadian Mineralogist. Vol. 42. Mineralogical Association of Canada, Ottawa, pp. 1583–1599 Part 5.

Sun, S.S., 1980. Lead isotopic study of young volcanic-rocks from Mid-Ocean ridges, Ocean Islands and Island Arcs. Phil. Trans. R. Soc. A 297 (1431), 409–445.

Sun, S.S., McDonough, W.F., 1989. Chemical and isotopic systematics of oceanic basalts; implications for mantle composition and processes. Geol. Soc. Spec. Publ. 42, 313–345.

Thomas, J.B., Bodnar, R.J., 2002. A technique for mounting and polishing melt inclusions in small (> 1 mm) crystals. Am. Mineral. 87 (10), 1505–1508.

Thunell, R., Federman, A., Sparks, S., Williams, D., 1979. Age, origin, and volcanological significance of the Y-5 ash layer in the Mediterranean. Quat. Res. 12 (2), 241–253.

Tonarini, S., Leeman, W.P., Civetta, L., D'Antonio, M., Ferrara, G., Necco, A., 2004. B/Nb and delta ^{11}B systematics in the Phlegrean volcanic district, Italy. J. Volcanol. Geotherm. Res. 133, 123–139.

Tonarini, S., D'Antonio, M., Di Vito, M.A., Orsi, G., Carandente, A., 2009. Geochemical and B–Sr–Nd isotopic evidence for mingling and mixing processes in the magmatic system that fed the Astroni volcano (4.1–3.8 ka) within the Campi Flegrei caldera southern Italy. Lithos 107 (3–4), 135–151.

Turi, B., Taylor Jr., H.P., Ferrara, G., 1991. Comparisons of ^{18}O ^{16}O and ^{87}Sr/^{86}Sr in volcanic rocks from the Pontine Islands, M. Ernici, and Campania with other areas in Italy. In: Special Publication - Geochemical Society. 3. pp. 307–324.

Villemant, B., 1988. Trace element evolution in the Phlegrean Fields (Central Italy): fractional crystallization and selective enrichment. Contrib. Mineral. Petrol. 98, 169–183.

Vitale, S., Isaia, R., 2014. Fractures and faults in volcanic rocks (Campi Flegrei, southern Italy): insight into volcano-tectonic processes. Int. J. Earth Sci. 103 (3), 801–819.

Di Vito, M., Lirer, L., Mastrolorenzo, G., Rolandi, G., Scandone, R., 1985. Volcanological Map of Campi Flegrei. Ministero Protezione Civile e Università di Napoli.

Webster, J.D., Raia, F., De Vivo, B., Rolandi, G., 2001. The behavior of chlorine and sulfur during differentiation of the Mt. Somma-Vesuvius magmatic system. Mineral. Petrol. 73 (1–3), 177–200.

Webster, J.D., Raia, F., Tappen, C., De Vivo, B., 2003. Pre-eruptive geochemistry of the ignimbrite-forming magmas of the Campanian volcanic zone, southern Italy, determined from silicate melt inclusions. Mineral. Petrol. 79 (1), 99–125.

Welsch, B., Faure, F., Famin, V., Baronnet, A., Bachèlery, P., 2013. Dendritic crystallization: a single process for all the textures of olivine in basalts? J. Petrol. 54 (3), 539–574.

Wohletz, K., Orsi, G., Devita, S., 1995. Eruptive mechanisms of the Neapolitan-yellow-tuff interpreted from stratigraphic, chemical, and granulometric data. J. Volcanol. Geotherm. Res. 67 (4), 263–290.

Yaxley, G., Kamenetsky, V., Kamenetsky, M., Norman, M., Francis, D., 2004. Origins of compositional heterogeneity in olivine-hosted melt inclusions from the Baffin Island picrites. Contrib. Mineral. Petrol. 148 (4), 426–442.

Zollo, A., Maercklin, N., Vassallo, M., Dello Iacono, D., Virieux, J., Gasparini, P., 2008. Seismic reflections reveal a massive melt layer feeding Campi Flegrei Caldera. Geophys. Res. Lett. 35, L12306.